Design and Performance Evaluation of an Outer Stator Magnetically Geared Permanent Magnet Machine

by

Pushman Michael Tlali

Thesis presented in partial fulfilment of the requirements for the degree of Master of Science in Electrical Engineering in the Faculty of Engineering at Stellenbosch University

Department of Electrical and Electronic Engineering,
University of Stellenbosch,
Private Bag X1, Matieland 7602, South Africa.

Supervisor: Prof. R-J. Wang

March 2015

Declaration

By submitting this thesis electronically, I declare that the entirety of the work contained therein is my own, original work, that I am the sole author thereof (save to the extent explicitly otherwise stated), that reproduction and publication thereof by Stellenbosch University will not infringe any third party rights and that I have not previously in its entirety or in part submitted it for obtaining any qualification.

Signature: .....
P. M. Tlali

Date: 20/02/2015 .....

Abstract

Design and Performance Evaluation of an Outer Stator Magnetically Geared Permanent Magnet Machine

P. M. Tlali

Department of Electrical and Electronic Engineering,
University of Stellenbosch,
Private Bag X1, Matieland 7602, South Africa.

Thesis: MScEng (E & E)

March 2015

In this thesis, a magnetically geared permanent magnet (MGPM) machine is proposed for use in wind power generation. The outer-stator MGPM machine considered in this project incorporates a flux modulated coaxial magnetic gear (CMG) and a synchronous permanent magnet (PM) machine in a single volume to achieve a highly compact and torque dense machine configuration. The contact-less torque transmission property and over-load protection capability inherent to the CMG may solve the reliability concerns with current mechanically geared wind turbine drive-trains.

The operating principles and the design methodology of the MGPM machine are described in detail. An efficient finite element method (FEM) based design optimization approach has been implemented in the design of the machine. The optimized machine shows that a torque density close to 100 $\mathrm{kNm/m^3}$ can be achieved, which is significantly higher than that achieved by conventional electrical machines. A prototype machine is constructed and experimentally evaluated. The measured torque performance shows good agreement with the predicted performances, but a significant difference exists between the measured and calculated efficiencies. This is mainly due to the higher than expected mechanical loss in the MGPM machine. In addition, the design related aspects are also analyzed and discussed. Relevant recommendations are made for future work.

Uittreksel

Ontwerp en Werkverrigting Evaluasie van 'n Buite-Stator Magneties-Geratte Permanente Magneet Masjien

P. M. Tlali

Departement Electriese en Electroniese Ingenieurswese,
Universiteit van Stellenbosch,
Privaatsak X1, Matieland 7602, Suid Afrika.

Tesis: MScIng (E & E)

Maart 2015

In hierdie tesis word 'n magneties-geratte permanente magneet (MRPM) masjien voorgestel vir gebruik in windkrag opwekking. Die buite-stator MRPM masjien wat in hierdie projek oorweeg word, integreer 'n vloedgemoduleerde koaksiale magnetiese rat (KMR) en 'n sinchrone permanente magneet (PM) masjien in 'n enkele eenheid om sodoende 'n hoogs kompakte en draaimoment-digte masjien konfigurasie te lewer. Die kontaklose draaimoment oordrag eienskap en oorbelasting beveiligingsvermoë inherent aan die KMR mag die betroubaarheidsprobleem met huidige meganies-geratte wind turbine aandryfstels oplos.

Die werking en die ontwerpsmetodologie van die MRPM masjien word in detail beskryf. 'n Doeltreffende eindige element gebaseerde ontwerpsoptimering benadering is gebruik in die ontwerp van die masjien. Die geöptimeerde masjien toon dat 'n draaimomentdigtheid na aan 'n 100 kNm^3 bereik kan word, wat aansienlik hoër is as wat met konvensionele elektriese masjiene bereik kan word. A prototipe is gebou en eksperimenteel geëvalueer. Die gemete draaimoment vermoë stem goed ooreen met die voorspelde waardes, maar 'n noemenswaardige verskil tussen die gemete en berekende effektiwiteite kom voor. Hierdie verskil is grootendeels die gevolg van die hoër as verwagte meganiese verliese in die MRPM masjien. Die ontwerpsverwante aspekte word ook geanaliseer en bespreek. Relevante aanbevelings word gemaak vir toekomstige werk.

Acknowledgements

I would like to express my honest gratitude to the following:

- **GOD** for every day's life, endless love and blessings
- My supervisor, Prof. Rong-Jie Wang, for his intelligent supervision, academic guidance and support.
- Special thanks to ABB (Sweden) for providing financial support for this project.
- Stiaan Gerber, for his great help and wise advice.
- EMlab workshop staff for their help on the prototype assembling and test-bench set-up.
- EMlab colleagues for their friendship and good cooperation.
- Finally, many thanks to my family and friends for their persistent support through out my educational career.

List of Publications

Part of the work in this thesis has been presented at either international or national conferences. Below is a list of the published papers:

[1] Wang, R-J., Bronn, L., Gerber, S. and Tlali, P.M.: Design and evaluation of a disc-type magnetically geared pm wind generator. In: *Power Engineering, Energy and Electrical Drives (POWERENG), 2013 Fourth International Conference on*, pp. 1259-1264. May 2013, Istanbul, Turkey.

[2] Tlali P.M., Gerber, S. and Wang, R-J.: Gear ratio selection of an outer-stator magnetically geared machine. In: *Southern African Universities Power Engineering Conference (SAUPEC)*, pp. 242-248, January 2014, Durban, South Africa.

[3] Tlali, P.M., Wang, R-J. and Gerber, S.: Magnetic gear technologies: A review. In: *Electrical Machines (ICEM), 2014 XXI International Conference on*, pp. 539-545, Sept 2014, Berlin, Germany,

Dedications

To my sister, 'Mamokhele Joyce Tlali
Even though we are far apart, You are always on our minds,
And You will forever remain in my heart...

Contents

List of Figures

List of Tables

Nomenclature

Constants

$\mu_0 = \quad 4\pi \times 10^{-7}\,\mathrm{Wb/(A.m)}$

Greek Symbols

μ_r	Relative recoil permeance	[ ]
θ	Rotational angle	[rad]
θ_0	Initial angle	[rad]
θ_{mp}	Modulator pole-pitch angle	[rad]
θ_{mi}	Modulator inner width angle	[rad]
θ_{mo}	Modulator outer width angle	[rad]
θ_p	Magnet or stator pole-pitch angle	[rad]
θ_s	Magnet span or stator pole span angle	[rad]
θ_{sp}	Stator slot pitch angle	[rad]
θ_{ss}	Stator slot pole angle	[rad]
α_p	Magnet pole-arc angle	[rad]
ω	Rotational velocity	[rad/s]
ω_h	Angular velocity of gear's inner rotor	[rad/s]
ω_l	Angular velocity of gear's outer rotor	[rad/s]
ω_r	Rotor angular velocity	[rad/s]
ω_s	Modulator angular velocity	[rad/s]
λ	Flux linkage	[Wb]
λ_d	d-axis flux linkage	[Wb]

λ_q	q-axis flux linkage	[Wb]
λ_{PM}	Flux linkage due to PMs	[Wb]
ρ_T	Conductor resistivity at temperature T	[Ω/m]
η	Percentage efficiency	[%]
τ_s	Modulator torque	[Nm]
ξ	Machine's stack length to outer diameter ratio	[ ]

Acronyms

2D	Two Dimensional
3D	Three Dimensional
CMG	Coaxial Magnetic Gear
DDG	Directly Driven Generator
EMF	Electromotive force
FEA	Finite Element Analysis
FEM	Finite Element Method
HTS	High Temperature Superconductor
LCM	Least Common Multiple
MG	Magnetic Gear
MGM	Magnetically Geared Machine
MGPM	Magnetically Geared Permanent Magnet
PM	Permanent Magnet
PMSM	Permanent Magnet Synchronous Machine
RMS	root-mean square

Variables

A_{cond}	Conductor cross section area	[mm^2]
A_{slot}	Slot cross section area	[mm^2]
B_r	Permanent magnet remanence	[T]

B_R	Radial flux density	[T]
B_θ	Tangential flux density	[T]
e_m	Electromotive force	[V]
E_a	Per-phase rms value of EMF	[V]
E_d	d-axis induced voltage	[V]
E_q	q-axis induced voltage	[V]
f	Frequency	[Hz]
f_c	Cogging torque factor	[ ]
f_e	Electrical frequency	[Hz]
G_r	Gear ratio	[ ]
I_A	Armature current	[A]
I_d	d-axis current	[A]
I_q	q-axis current	[A]
I_{mag}	Current magnitude	[A]
J	Current density	[A/mm^2]
k	Optimization iteration step	[ ]
K_f	Cross section of available slot area	[mm^2]
K_{w1}	Fundamental winding factor	[ ]
l	Machine stack length	[m]
l_e	Single side end-winding length	[m]
l_{st}	Stator tooth length	[m]
L	Inductance	[H]
L_s	Synchronous inductance	[H]
L_e	Stator end-winding inductance	[H]
L_m	Stator main inductance	[H]
m	Number of phases	[ ]
M_n	Permanent magnetization distribution	[T]

M_{CU}	Mass of copper material in a machine	[kg]
M_{FE}	Mass of magnetically active iron material in a machine	[kg]
M_{PM}	Mass of permanent magnet material in a machine	[kg]
M_{Tot}	Total mass of active material in a machine	[kg]
n_{cond}	Number of turns in series per phase	[ ]
n_l	Number of winding layers	[ ]
n_s	Rotational speed	[rpm]
p	Pole-pair number	[ ]
p_h	Inner rotor PM pole-pair number	[ ]
p_l	Outer rotor or stator PM pole-pair number	[ ]
P	Real power	[W]
P_{in}	Input power	[W]
P_c	Core power losses	[W]
P_{cu}	Copper losses	[W]
P_f	Power factor	[ ]
P_{fr}	Friction losses	[W]
P_{loss}	Total power losses	[W]
P_{out}	Output power	[W]
P_w	Windage power losses	[W]
q	Number of stator slots per pole per phase	[ ]
q_s	Pole-pair number of modulator pole-pieces	[ ]
Q	Number of stator slots	[ ]
r	Radial distance	[m]
r_{md}	Modulator inner radius	[m]
r_y	Inner rotor inner yoke radius	[m]
r_{s_out}	Stator outer radius	[m]
r_{s_in}	Stator inner radius	[m]

R_a	Outer radius of inner rotor yoke	[m]
R_A	Armature resistance	[Ω]
R_b	Outer radius of inner rotor PMs	[m]
R_c	Inner radius of outer rotor yoke	[m]
R_C	Stator core resistance	[Ω]
R_d	Inner radius of outer rotor PMs	[m]
R_r	Radial magnetic permeance	[Wb/A]
R_θ	Circumferential magnetic permeance	[Wb/A]
S	Apparent power	[VA]
S_{ff}	Stator slot filling factor	[ ]
t	Time	[s]
t_{brg}	Modulator bridge thickness	[m]
t_{mh}	Inner rotor magnet thickness	[m]
t_{md}	Modulator thickness	[m]
t_{ms}	Stator PM thickness	[m]
t_y	Inner rotor yoke thickness	[m]
t_{sb}	Stator tooth base thickness	[m]
t_{st}	Stator tooth thickness	[m]
t_{sy}	Stator yoke thickness	[m]
T_{EM}	Electromagnetic torque	[Nm]
T_M	Magnetic torque	[Nm]
V_ϕ	Terminal voltage	[V]
V_d	d-axis terminal voltage	[V]
V_q	q-axis terminal voltage	[V]
X_s	Synchronous reactance	[Ω]

Chapter 1

Introduction

1.1 Wind power development

The steadily increasing world-wide energy demands and environmental concerns resulting from the greenhouse effect, have added urgency to the move towards renewable energy sources. In a global campaign for the reduction of the heavy consumption of fossil fuels, significant attention has been paid to wind energy as one form of the renewable energies available in abundance. It has been estimated that the installed global wind energy capacity increased more than 6 fold within a period of ten years to a total of 318 GW by the end of 2013 [1–4], which comes to about a 2.9% contribution to global energy production. Figure 1.1 further reveals that wind energy is one of the fastest growing renewable energy since its percentage share among all renewable energies has increased 4 times over the last decade.

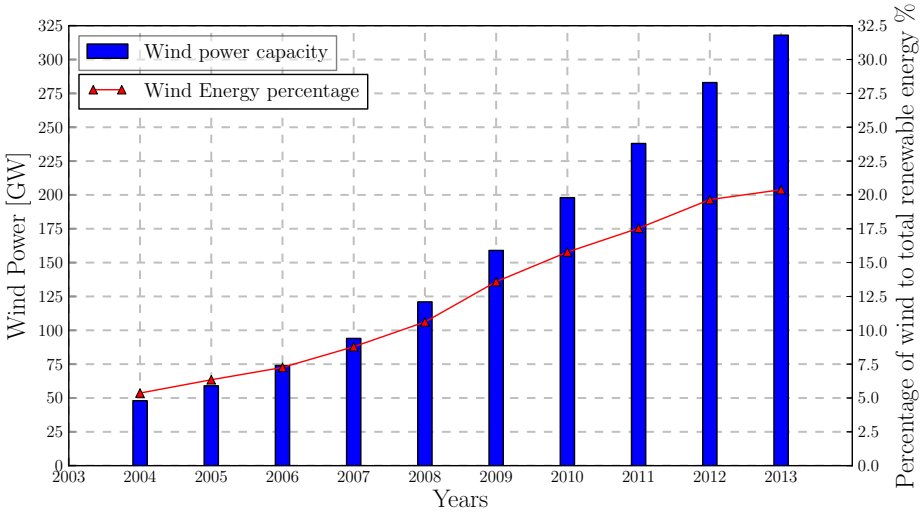

Figure 1.1: Growth of wind energy in the last ten years [1–4].

Essential to the growth of wind energy production are the electrical machines (genera-

tors in this case) which perform a pivotal role of electro-mechanical energy conversion in a wind turbine. Wind generators need to have a high efficiency in order to utilize most of the kinetic energy extracted by the turbine blades. In addition, they must be more reliable to guarantee a minimum risk of operational faults and maintenance costs. Therefore, their advancement mainly in efficiency and reliability aspects is of utmost importance both for the satisfaction of energy requirements at competitive costs and the alleviation of greenhouse gas emissions.

1.2 Wind turbine generator systems

The significant attention paid to wind energy harvesting in the past decades has led to the search for more efficient and reliable electrical generators. In wind power generation industries, the combination of a mechanical gearbox and a medium or high speed machine is often employed to match both the low speed and high torque inputs from turbine blades with the values tolerated by the generator, forming the mechanically geared system. This certainly exhibits improved performance with reduced generator size and mass. However, because of their intrinsic contact mechanism, mechanical gears are prone to severe frictional losses, teeth wearing and are likely to be permanently damaged if overloaded. Such drawbacks are the major source of the need for frequent maintenance in the turbine drive-drain since their failure leads to not only the long down-times, but also expensive repairs or replacements of wind turbines [5]. Besides their acoustic noise which is generally experienced as disturbing by the community around the wind farms, mechanical gearbox failures are regarded as the main cause of short wind turbine operational time relative to their intended 20 to 30 years design lifetime [5, 6].

Directly driven generators (DDGs) are generally preferred over mechanically geared generator concepts due to their lower part count, simplicity and higher reliability prospects. As a result, operational failures and maintenance issues are kept to the minimum in this configuration. Nevertheless, at higher power levels with lower input speeds, which is usually the case with larger wind turbine systems, DDGs quickly approach bulky sizes and heavy weights. Previous comparative studies of these two concepts reports that the DDG is several times heavier than the geared generator with higher cost and almost equal energy yield [7,8]. This shows that, technologically, direct-drive wind turbines present some advantages. However, the economic incentive for a shift from geared systems to direct-drive systems seems insufficient. The high cost associated with direct-drive technology has been a key deterring factor.

On the other hand, magnetically geared permanent magnet (MGPM) machines have been proposed as an attractive alternative to both DDGs and mechanically geared machines. MGPM machines incorporate both a permanent magnet synchronous machine

(PMSM) and a magnetic gear (MG) into one volume. Instead of physical teeth meshing as in mechanical gears, MGs transfer torque or power through the force interaction of virtual magnetic fields' teeth. As a result of their contact-less operation, MGs boasts several important advantages namely:

- Inherent overload protection.
- Quiet operation.
- Little maintenance and
- Potential for high torque density and efficiency.

Therefore, it is envisaged that with a combination of a PM machine and MG, a better performance machine with reduced size and weight can be realized. This project is focused on the design and evaluation of an outer stator magnetically geared machine for wind power generation applications. In this chapter, the background and context leading to the current interest and research into this technology is given. Furthermore, a brief review is given to highlight the important achievements and recent developments in historical context.

1.3 Literature review

It is important to note that MGs or MGPM machines are not new, but their popularity, and hence industrial interest, have been hampered by the poor performance of both permanent magnets and old MGs' structure which were basically analogous to that of mechanical gears. Accordingly, the commercialization and affordability of high energy PMs such as neodymium-iron-boron ($Nd_2Fe_{14}B$) and sophisticated MGs' topologies which include flux modulated and harmonic MGs, have been the driving force behind the current revival of this idea.

1.3.1 Magnetic gears

Literature reveals that the magnetic gearing principle is more than a century old technology [9], with credit given to C. G. Armstrong for the invention of the first MG shown in Fig. 1.2. [10]. The earliest MGs had a prime mover with salient electromagnetic teeth while the driven mover had only the steel teeth [10–12]. For this reason, impractical air-gap lengths were required for improved torque density. In addition, the slip rings connecting the electromagnets to their current source added more losses to these devices which degraded their efficiency. Because of their complicated and bulky structures in combination with low efficiency as mentioned, magnetic gears garnered little recognition,

and no evident utilization of this idea could be seen during the first few decades after its invention.

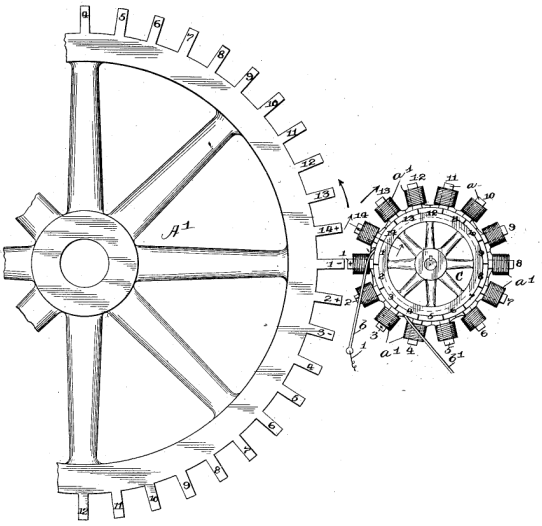

Figure 1.2: First magnetic gear [10].

By the middle of the nineteenth century, stronger PMs began to emerge in the commercial market, hence the designers of MGs switched from the use of electromagnetic teeth to permanent magnetic teeth. In comparison to the previous electro-magnetic gears, the use of PMs had some obvious merits such as higher efficiency and reduced size and weight. While the torque transmission of earlier designs was based on attractive forces and allowed for pole-slipping on overloaded conditions, the gear which Faus patented worked according to a slightly different principle, shown in Fig. 1.3 [13]. The gear has intermeshed teeth as in mechanical gears, but with little air-gaps maintained between them, and the rotors are mounted with similar polarity of PMs, thereby transmitting torque through repulsive forces. Although the performance of his patent might have an improvement relative to older designs, the downside was that the teeth were exposed to a risk of breaking when the gear has overloaded.

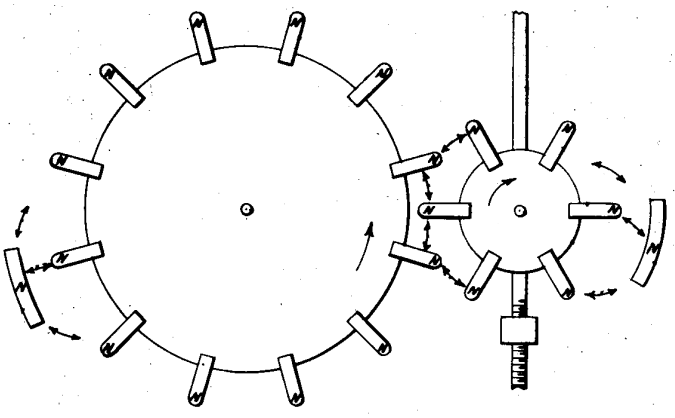

Figure 1.3: Faus's MG with intermeshed PM teeth [13].

The historic magnetic gear development was focused mostly on the MGs with fundamental operating principles derived from already existing types of mechanical gears, except that the torque was transmitted by magnetic interaction. Since PMs can be produced in various shapes, almost all mechanical gear topologies could also be converted into their MGs' version, for instance, spur gears [13–19], bevel gears [20], rack and pinion gears, and even the intricate topologies such as worm gears [21, 22] and belt and pulley [23] were realized. In Fig. 1.4, some of these MGs derived from mechanical topologies are shown with their counterparts. However, due to the fact that few PMs got engaged into torque transmission at each time instant, a limited magnitude of torque values were transferred between the rotors.

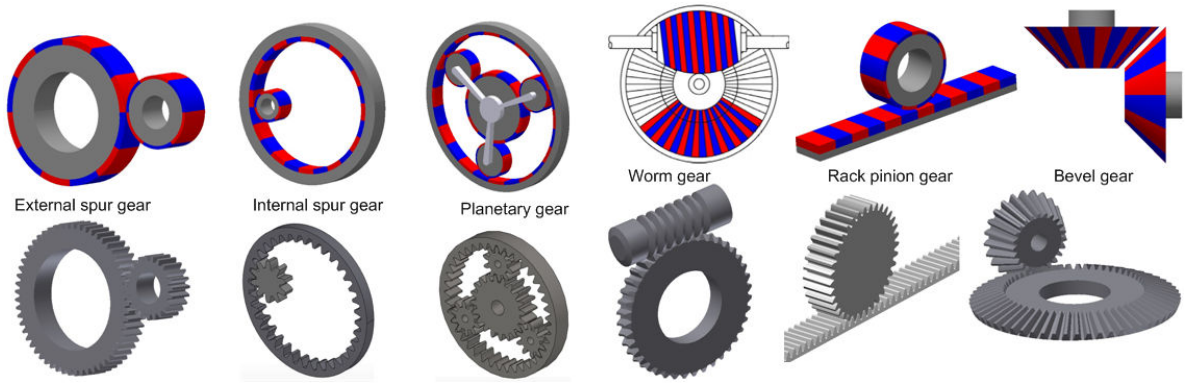

Figure 1.4: MGs with their corresponding mechanical gear topologies

Most of these MGs with converted configurations, except for planetary types, were characterized by significantly low torque densities in comparison to their mechanical counterparts [24]. Hence, they could hardly be regarded as future replacements for mechanical gears in industrial applications. On one hand, researchers of the time could deduce from the concept of magnetic couplers that with many PMs simulataneously involved in action, higher torque can be transferred [18, 19, 25, 26].

In the late 1960s, Martin introduced a notable concept of an MG (Fig.1.5) with two concentric PM rotors and a flux modulator situated between them [27]. The structural arrangement of this gear looked almost like those of the reluctance MGs described in [11,28], except that it had PMs mounted on the two rotors instead of the electromagnets on only one rotor as in [11, 28]. Therefore, this concept of flux modulated MG had a different operating principle, and because of many PM pole-pairs engaged in the movement at any time instant, it promised to have a higher torque density, although no measurements were reflected.

Martin's invention attracted interest from many researchers so much that further studies on this principle were carried out, e.g. those by Laing [29,30] and Ackermann [31,32].

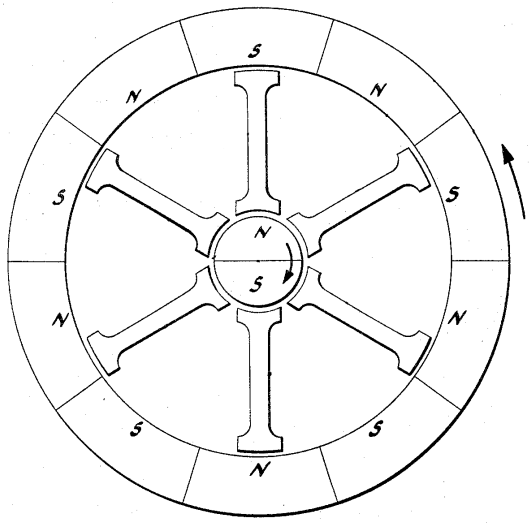

Figure 1.5: Martin's flux modulated magnetic gear [27].

Both of these studies focused mostly on the different shapes and arrangements of the modulator segments illustrated in Fig. 1.6. Moreover, Ackermann delineated the mathematical relations between the numbers of pole-pairs of the rotor PMs and the modulator pieces.

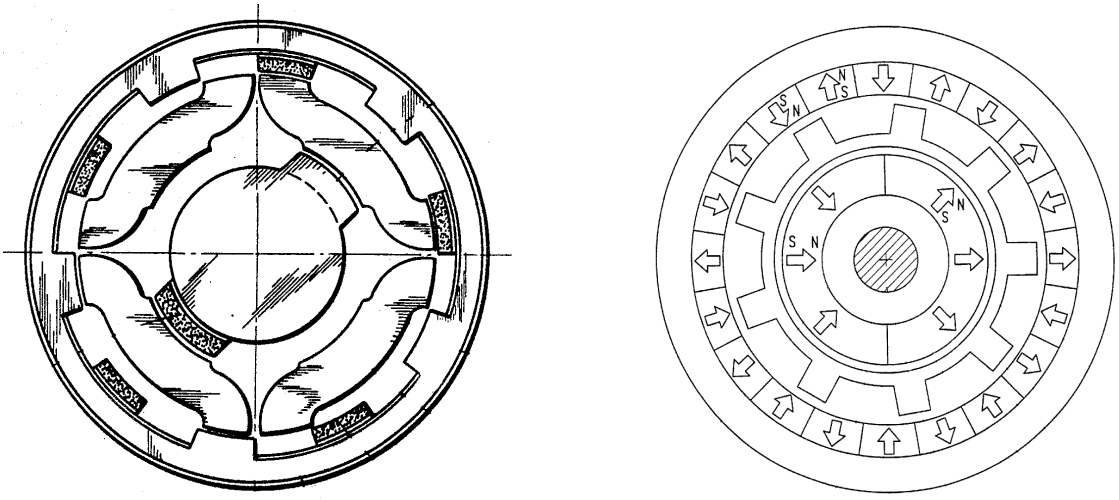

(a) (b)

Figure 1.6: Alternative flux modulated MGs by (a) Laing, (b) Ackermann.

Atallah and Howe published an important paper on the flux modulated coaxial MG in 2001 shown in Fig. 1.7 [33], in which the design of this gear was clearly outlined and its high torque capability was first revealed. The designed gear was fundamentally the same as Ackermann's design in [31], except that the modulator pole-pieces were not physically connected to each other. Its basic operation principle relied on the ferromagnetic pole-pieces interposed between the inner and outer PM rotors to modulate the magnetic field such that each rotor "sees" a working space harmonic corresponding to its own number of

poles. Moreover, the authors demonstrated through simulation studies that a combination of this MG and a PM machine can result in a system with outstanding performance. Therefore this gear type became fashionable.

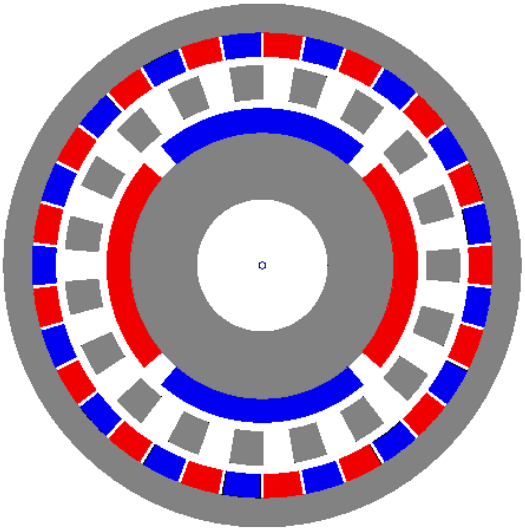

Figure 1.7: Coaxial flux modulated magnetic gear [33].

The operational principle of coaxial flux modulated MGs can also be designed into linear/tubular and disc-type topologies shown in Fig. 1.8. A disc-type MG, first proposed in [34], has axially magnetized PMs mounted on the opposite faces of two radially laminated rotor discs with modulating pieces between them. It was shown that a torque density over 70 kNm/m^3 is attainable from this type of gear [34], but also has significant eddy current losses which have an adverse impact on its efficiency [35].

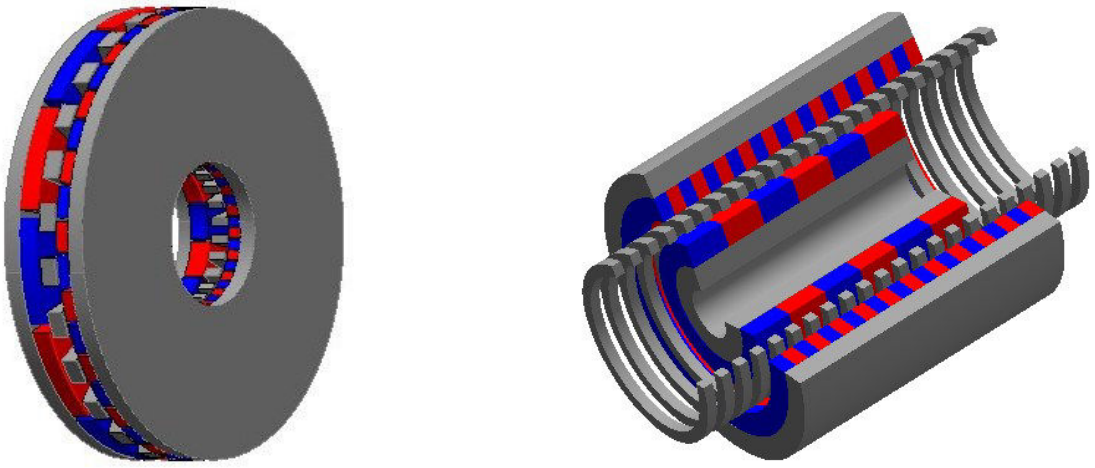

(a) disc-type (b) linear type

Figure 1.8: Other configurations of concentric MGs: (a) disc-type, (b) linear type.

A linear concentric MG was first presented in [36], and has a tubular structure with outer and inner shorter PM movers separated by the ferro-magnetic rings along the length of the gear. Simulation studies showed that a high force density can be achieved with this linear topology, which is however sensitive to the axial length of the spacers between the ferromagnetic rings [37,38].

Besides the coaxial flux modulated concept, the two other torque dense MGs that have recently attracted interest are the planetary (Fig. 1.9b) and harmonic (Fig. 1.9a) types of gears. The operation principle of a harmonic MG relies on a mechanism to produce a sinusoidal time varying air-gap length between the low-speed PM rotor and the rigid PM stator [39, 40]. The air-gap length is varied as the high-speed rotor deforms the flexible low-speed rotor which then rotates within a rigid outer stator. Then the variation of the air-gap length modulates the magnetic field produced by the low-speed rotor PMs so that the resultant asynchronous space harmonic field interacts with stator PMs to facilitate torque transmission.

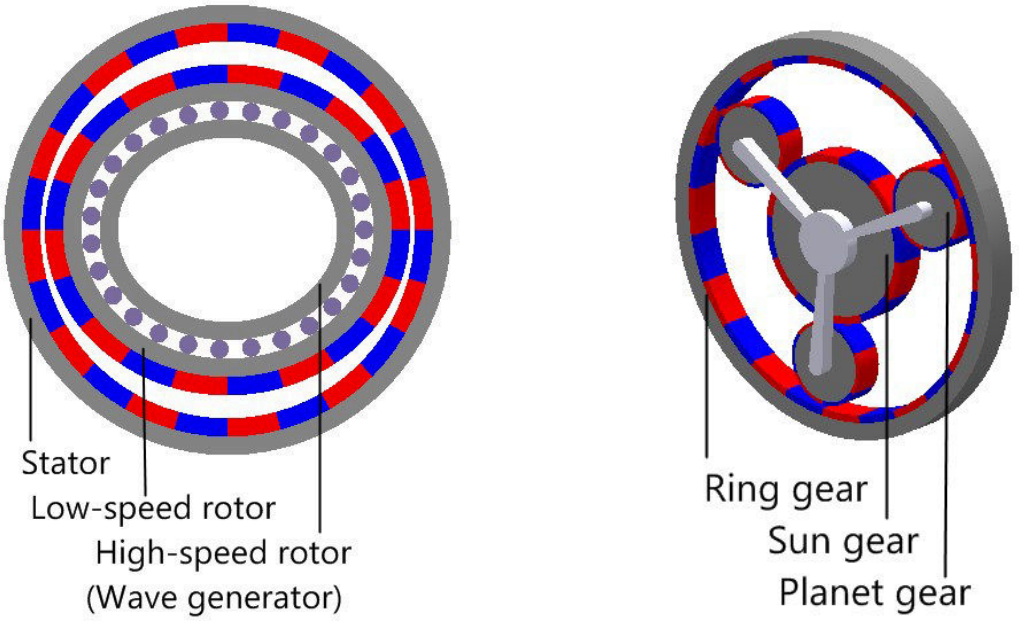

(a) harmonic gear (b) planetary gear

Figure 1.9: Planetary and harmonic MGs.

It was pointed out that this type of gear exhibits a smooth torque, and is suitable for high gear ratios and torque density [41]. However, the harmonic MG is complicated by the requirement of the flexible PM rotor. One technique to solve this problem is to implement an eccentrically rotating rigid low-speed PM rotor [42], although this will still need flexible coupling. A dual stage arrangement was also proposed as an alternative configuration that eliminates the need for flexible PM rotor or coupling [39, 41]. Despite all its distinctive merits and attempts to get them working, harmonic MGs remained practically unsuccessful.

In the same way as their mechanical counterparts, planetary MGs are characterized by three major components, *i.e*, the sun, planets and ring gear. The exploration of this type of MG began a few decades ago [43–45], although much analysis became apparent only in the recent years [46–49]. The planetary MG's advantages include the capability of three transmission modes, high gearing ratios and high torque density. It was reported that its torque density is proportional to the number of planet gears, but the upper limit to this number may exist as a consequence of cogging torque [47] and leakage flux losses.

The concentric-type MG has currently taken the centre stage in both research and industrial institutions due to the following reasons:

- Of all MGs with competent torque densities to the mechanical gears, it is the least complex to construct.
- It can be integrated with a PM machine without much struggle.
- The same concept can easily be rearranged into radial, axial or linear shapes, although radial configuration is the most common.

The flux modulated coaxial MG's performance is sensitive to many of its design parameters, including the modulator pieces and PM pole-pairs arrangement. To assess the effect of the flux modulator on the torque quality and magnitude, different mechanical linkage options illustrated in Fig. 1.10 were evaluated in [50], which showed that the internally connected modulator has the least impact on the torque capability of an MG. This is in good agreement with [51, 52], which further reveals the benefits of thin internal mechanical bridges such as loss reduction and suppression of undesirable harmonics. Jian *et al.* [53] proposed the use of high temperature superconductor (HTS) materials for modulator pole-pieces, as this can significantly reduce the modulator thickness and also the end effects. The effect of the stack length of the modulator was investigated in [52, 54], which show that maximum stall torque can be obtained when the modulator has the same stack length as that of both rotors.

In order to counteract large centrifugal forces experienced by the rotor PMs during high rotational speeds, interior [50] and spoke-type [55] PM configurations were considered for replacement of surface mounted PMs. The studies showed that although the PMs can be firmly secured on the rotor yoke with these methods, the torque capability is comparatively reduced as a consequence of leakage flux. Instead of radial magnetized PMs for radial flux gears, halbach PM configuration was also investigated in [56], which proved that the halbach attractive features can be beneficial for reduction of torque ripple and losses.

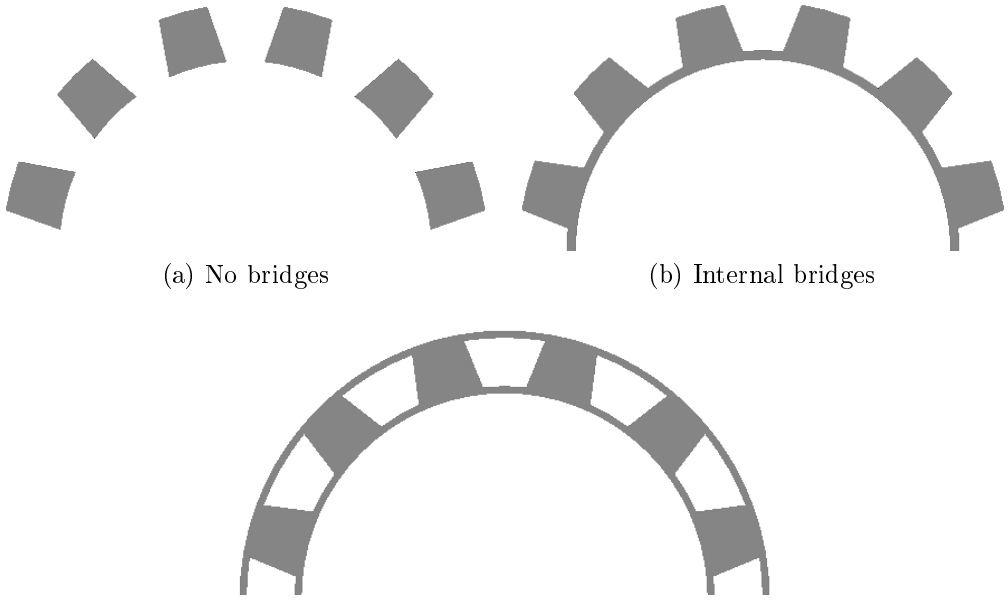

(a) No bridges (b) Internal bridges

(c) Double bridges

Figure 1.10: Different modulator arrangements for radial flux modulated MGs: (a) no bridge, (b) internal bridge, (c) double bridges.

1.3.2 Magnetically geared machines

Advances in magnetic gear technology led to the development of a new class of electrical machine: magnetically geared PM (MGPM) machines . These machines house a magnetic gear integrated with a PM machine in the same volume. In this way, the system torque density is increased beyond what can be achieved with a cascaded configuration.

Magnetically geared electric machines featuring the combined full MG and brushless PM motor/generator were first presented in the twentieth century [57–59], although the MGM operating on the principle of variable reluctance method was earlier described by Venturini [60] and the vernier principle introduced in [61]. The former designs shown in Fig. 1.11(a and b) are the two most prominent topologies of MGPM machines. The topology in Fig. 1.11a can be classified as an MGPM machine with an inner-stator, whereas the one in Fig. 1.11b can be classified as an MGPM machine with an outer-stator. The inner-stator topology can further be classified as either a coupled or decoupled configuration, illustrated by the left and right halves in Fig. 1.11a respectively. Another possible topology was presented in [62] where it is proposed that a winding be placed between the modulator segments. This type of topology, illustrated in Fig. 1.11c, can be referred to as a wound modulator magnetically geared machine.

The inner-stator topology is perhaps the most natural way of integration, especially in the decoupled case since the spaces occupied by the magnetic gear and electrical machine are completely separate. The decoupled configuration will have superior flux-weakening capabilities compared to the coupled configuration due to its higher inductance [63]. This

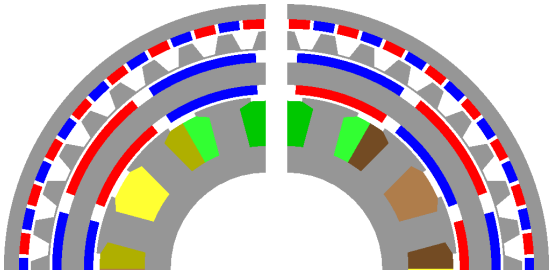

(a) Coupled/decoupled inner-stator configuration

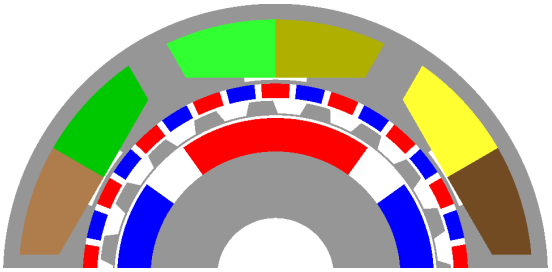

(b) Outer-stator configuration

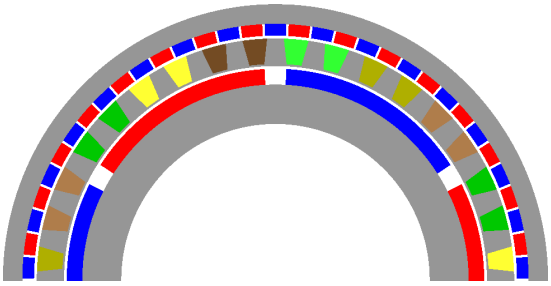

(c) Wound modulator configuration.

Figure 1.11: Topologies of magnetically geared machines.

can be an important consideration for applications such as traction drives. On the other hand, the coupled configuration generally has higher torque density because it does not require a thick high-speed rotor yoke. One major disadvantage of the inner-stator topology is the high level of mechanical complexity. The machine has four concentric components, three air-gaps and two rotors rotating at different angular velocities. Thus, the mechanical construction of this machine is challenging. Despite the difficulties, several prototypes of inner-stator MGPM machines have been realized [64–66].

The outer-stator topology has reduced mechanical complexity compared to the inner-stator topology because the outer magnets are attached directly to the inner surface of the stator. In this way, the number of air-gaps is reduced to two. It has been demonstrated that a torque density greater than 60 kNm/m^3 can be achieved [59,67]. It was found in one study that the outer-stator MGPM machine does not perform as well as the inner-stator topology in terms of torque density for a small machine [68].

In addition to the radial flux configurations, such as those displayed in Fig. 1.11, disc [69] and linear configurations can also be realized. One of the main design challenges with disc-type MGPM machine topology is to mechanically balance the resultant axial magnetic forces on the PM rotor interposed between the modulator and stator. Furthermore, it was reported that the machine has too much eddy current losses concentrated in the low-speed rotor, which heavily affects its efficiency [69].

In summary, magnetic gearing technology is not an entirely new concept but it has been disregarded in the industrial applications in the past. The recent growing interest in

this technology may be attributed to the availability of energy dense magnetic material and novel torque dense MG topologies. Amongst others, coaxial flux modulated MGs are of particular interest as they are not only of high torque density, but can also easily be integrated with a PM machine to realize a compact MGPM machine suitable for applications such as wind-turbines and electric vehicle motors. The attractive features of MGs can therefore boost the operational performance of the overall electro-mechanical systems. However, more practical validation of this idea is still necessary to prove its potential benefits over the normal mechanical gear to PM machine coupling.

1.4 Research aims and methodology

Wind power is one of the abundant, most attractive and competitive renewable energy resources the exploitation of which has been a focus of the global renewable energy development. However, the challenges associated with the traditional wind turbine drive-train system proves that there is room for improvement of this technology. The main aim of this research project is to evaluate a magnetically geared permanent magnet (MGPM) machine technology, as a potential alternative to the conventional mechanically geared wind generator system. The outcome of this research will outline the true potential of this technology for wind power application.

The basic research methodology employed in this work is to optimally design, construct and experimentally evaluate an outer-stator type MGPM machine. The machine design optimization is focused on the maximizing of its torque capability and weight reduction, and possibly lower cost, as these are some of the critical characteristics required for the wind generator. The following steps are carried out to accomplish the goal of this project.

- Conduct the literature review of MGs and MGPM machines to determine the current state of this technology development.
- Investigate the MG's and MGPM machine's operating principle and design methodology.
- Derive the equivalent circuit and parameters of the outer-stator type MGPM machine necessary for its analysis.
- Carry out FEM design analysis and optimization of the MGPM machine.
- Construct the MGPM machine prototype.
- Perform experimental tests on the manufactured MGPM machine prototype.
- Evaluate the performance of the MGPM machine from both theoretical and practical results.

1.5 The layout of the thesis

The basic layout of the thesis is as follows:

In Chapter 1 a literature review of the magnetic gears and magnetically geared permanent magnet machines are presented.

In Chapter 2 the basic operating principle and theory of MGs and MGPMs are presented. From the equivalent circuit of the outer stator MGPM machine, which is the focus of this study, the derivation of parameters and equation formulations necessary for the performance evaluation of this machine are carried out.

In Chapter 3 the computation of electrical design variables, FEM modeling and design optimization of the outer stator MGPM machine are addressed. Furthermore, the used optimization algorithm and procedure are also discussed. The optimized results are documented and this is followed by a discussions of certain optimized machine's magnetic and electrical behavior.

In Chapter 4 the mechanical construction and assembly of a MGPM machine prototype are described. The details of the manufacturing process of the machine and materials used for the production of its components are also provided.

In Chapter 5 the results of the experimental tests of the prototype machine are presented. The no-load and loaded test results are analyzed and compared to simulation results where applicable. The efficiency map of the machine from experimental results is constructed to highlight the best performance operating regions with respect to the machine loading conditions.

In Chapter 6, the conclusions pertaining the work presented in this thesis are drawn. In addition, some recommendations likely to make improvements in the future research on this type of machine are made.

Chapter 2

Principle of Magnetically Geared Machines

In this chapter the basic operational theory of the outer stator magnetically geared machine studied in this project is presented. Firstly, the gearing principle in coaxial magnetic gears is explained with reference to the equations predicting the behaviour of modulated air-gap magnetic field distribution. Afterwards, an overview of how such a machine can be realized from an magnetic gear and PM synchronous machine is provided. Then the equivalent circuit for the performance calculation of the MGPM machine is described.

2.1 Magnetic gears

The general structure of a flux modulated coaxial magnetic gear (CMG) with radially magnetized permanent magnets (PMs) is shown in Fig. 2.1. It has two concentric rotors with PMs mounted on opposite surfaces, separated by equal-spaced ferromagnetic pole-pieces. The main function of these ferromagnetic pieces is to modulate the magnetic fields originating from one rotor so that they have the same number of pole-pairs as the second rotor, hence the term "flux modulator". Normally, the rotor with the smallest number of pole-pairs is the high speed, rotor while the one with the large number of pole-pairs can play the role of a low speed rotor or just be the stationary component with the flux modulator.

From Fig. 2.1, it is obvious that both sets of PMs contribute concurrently to the magnetic field at any point in between the rotors. In addition, the magnitude and harmonic formation of the magnetic fields in the two air-gap regions are of great importance for stable torque transmission between the gear components. Therefore, to simplify their analytical description, the field produced from each rotor is first analyzed separately, with no modulator but only the yoke of a second rotor, as illustrated on Fig. 2.2. Then the effect of the flux modulator in the vicinity of rotor PMs is considered afterwards. In other

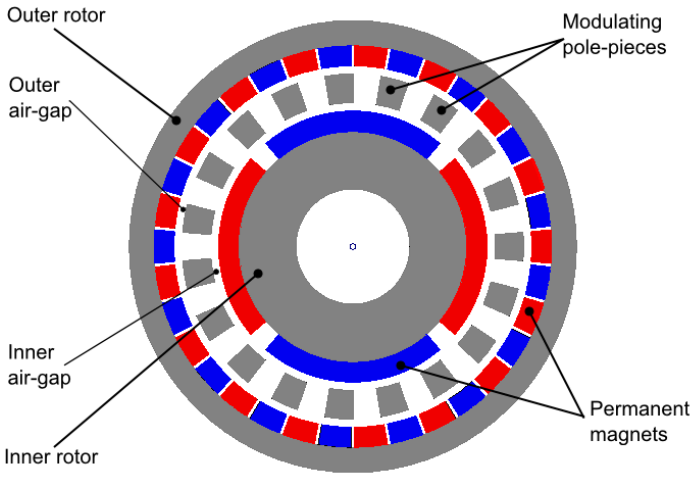

Figure 2.1: Radial flux modulated coaxial magnetic gear.

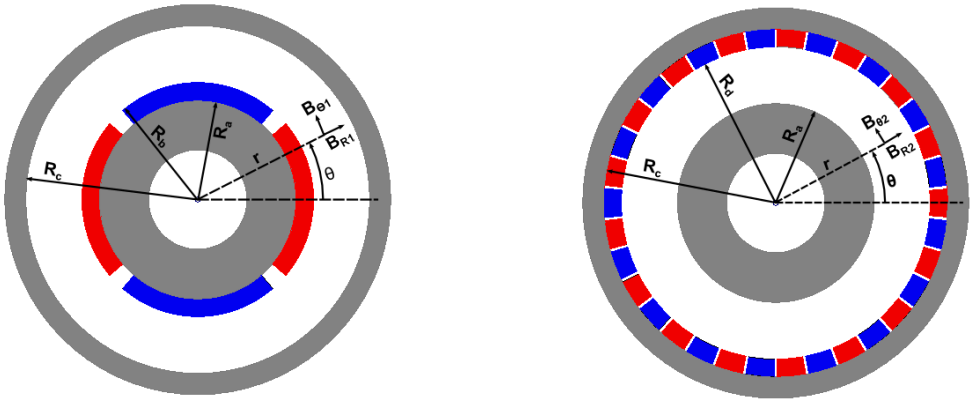

(a) (b)

Figure 2.2: Parameters of structural and magnetic fields parameters for rotors without flux modulator [56]: (a) with inner rotor PMs and (b) with outer rotor PMs.

words, this is more like initially analyzing an internal and external slotless stator machines with non-salient permanent magnet rotors, and later examining the effects made by slotted stator. The resultant field in each air-gap is the sum of the field contribution from both rotors in that specific air-gap.

The 2D model of rotor magnetic fields in the polar coordinates system developed in [70] was adopted and used with the following assumptions:

- Ferromagnetic components have infinite permeability.
- Permanent magnets are radially magnetized with linear second quadrant demagnetization characteristic.
- Permanent magnets have uniform magnetization throughout their cross-section, and with their relative recoil permeability equal to 1.04.
- The machine or gear has more than one pole-pair.

According to Zhu *et al*, the solution of Laplace's equations for the air-space scalar potential distribution gives the following expressions for the radial and tangential components of magnetic flux density [70]:

$$\begin{aligned} B_{R1}(r,\theta) = & \sum_{n=1,3,5,\ldots,}^{\infty} \frac{\mu_o M_n}{\mu_r} \frac{np}{(np)^2-1} \\ & \times \left\{ \frac{(np-1)+2\left(\frac{R_a}{R_b}\right)^{np+1}-(np+1)\left(\frac{R_a}{R_b}\right)^{2np}}{\frac{\mu_r+1}{\mu_r}\left[1-\left(\frac{R_a}{R_c}\right)^{2np}\right]-\frac{\mu_r-1}{\mu_r}\left[\left(\frac{R_b}{R_c}\right)^{2np}-\left(\frac{R_a}{R_b}\right)^{2np}\right]} \right\} \\ & \times \left[\left(\frac{r}{R_c}\right)^{np-1}\left(\frac{R_b}{R_c}\right)^{np+1}+\left(\frac{R_b}{r}\right)^{np+1}\right]\cos np\theta \\ = & \sum_{n=1,3,5,\ldots,}^{\infty} A(r)\cos np\theta \end{aligned} \tag{2.1.1}$$

$$\begin{aligned} B_{\theta 1}(r,\theta) = & \sum_{n=1,3,5,\ldots,}^{\infty} \frac{-\mu_o M_n}{\mu_r} \frac{np}{(np)^2-1} \\ & \times \left\{ \frac{(np-1)+2\left(\frac{R_a}{R_b}\right)^{np+1}-(np+1)\left(\frac{R_a}{R_b}\right)^{2np}}{\frac{\mu_r+1}{\mu_r}\left[1-\left(\frac{R_a}{R_c}\right)^{2np}\right]-\frac{\mu_r-1}{\mu_r}\left[\left(\frac{R_b}{R_c}\right)^{2np}-\left(\frac{R_a}{R_b}\right)^{2np}\right]} \right\} \\ & \times \left[\left(\frac{r}{R_c}\right)^{np-1}\left(\frac{R_b}{R_c}\right)^{np+1}-\left(\frac{R_b}{r}\right)^{np+1}\right]\sin np\theta \\ = & \sum_{n=1,3,5,\ldots,}^{\infty} B(r)\sin np\theta \end{aligned} \tag{2.1.2}$$

$$\begin{aligned} B_{R2}(r,\theta) = & \sum_{n=1,3,5,\ldots,}^{\infty} \frac{-\mu_o M_n}{\mu_r} \frac{np}{(np)^2-1} \\ & \times \left\{ \frac{(np-1)\left(\frac{R_d}{R_c}\right)^{2np}+2\left(\frac{R_d}{R_c}\right)^{np-1}-(np+1)}{\frac{\mu_r+1}{\mu_r}\left[1-\left(\frac{R_a}{R_c}\right)^{2np}\right]-\frac{\mu_r-1}{\mu_r}\left[\left(\frac{R_a}{R_d}\right)^{2np}-\left(\frac{R_d}{R_c}\right)^{2np}\right]} \right\} \\ & \times \left[\left(\frac{r}{R_d}\right)^{np-1}+\left(\frac{R_a}{R_d}\right)^{np-1}\left(\frac{R_a}{r}\right)^{np+1}\right]\cos np\theta \\ = & \sum_{n=1,3,5,\ldots,}^{\infty} C(r)\cos np\theta \end{aligned} \tag{2.1.3}$$

$$
\begin{aligned}
B_{\theta 2}(r,\theta) = & \sum_{n=1,3,5,\ldots,}^{\infty} \frac{\mu_o M_n}{\mu_r} \frac{np}{(np)^2-1} \\
& \times \left\{ \frac{(np-1)\left(\frac{R_d}{R_c}\right)^{2np} + 2\left(\frac{R_d}{R_c}\right)^{np-1} - (np+1)}{\frac{\mu_r+1}{\mu_r}\left[1-\left(\frac{R_a}{R_c}\right)^{2np}\right] - \frac{\mu_r-1}{\mu_r}\left[\left(\frac{R_a}{R_d}\right)^{2np} - \left(\frac{R_d}{R_c}\right)^{2np}\right]} \right\} \\
& \times \left[\left(\frac{r}{R_d}\right)^{np-1} - \left(\frac{R_a}{R_d}\right)^{np-1}\left(\frac{R_a}{r}\right)^{np+1}\right] \sin np\theta \\
= & \sum_{n=1,3,5,\ldots,}^{\infty} D(r) \sin np\theta
\end{aligned}
\tag{2.1.4}
$$

where p, μ_o and μ_r are the pole-pair number, permeability of free space and relative recoil permeability respectively, and all other geometric variables as defined in Fig. 2.2. The magnetization distribution M_n is defined as:

$$
M_n = \sum_{n=1,3,5,\ldots,}^{\infty} 2\left(\frac{B_r}{\mu_o}\right)\alpha_p \frac{\sin\frac{n\pi\alpha_p}{2}}{\frac{n\pi\alpha_p}{2}} \tag{2.1.5}
$$

where α_p is the magnet pole-arc angle and B_r is the remanent flux density of permanent magnets.

Basically, eqns. 2.1.1-2.1.4 show that the magnitude of the magnetic flux density distribution at any point $p(r,\theta)$ between the rotors is dependent on the gear's geometrical parameters. Hence, to understand the constitution and interaction of magnetic field harmonics, these equations are generally rewritten as the radial and tangential field components originating from either permanent magnet rotor, and also taking into the account the rotational speed of each rotor, as shown below:

$$
B_R(r,\theta) = \sum_{n=1,3,5,\ldots,}^{\infty} b_r(r)\cos\left(np\left(\theta-\omega_r t\right)+np\theta_0\right) \tag{2.1.6}
$$

$$
B_\theta(r,\theta) = \sum_{n=1,3,5,\ldots,}^{\infty} b_\theta(r)\sin\left(np\left(\theta-\omega_r t\right)+np\theta_0\right) \tag{2.1.7}
$$

where ω_r is rotational speed of permanent magnet rotor, subscripts r and θ indicate radial and tangential components respectively, and θ_0 is the initial rotor angle at a rest position. The radial and tangential Fourier coefficients b_r and b_θ are described by $A(r), C(r)$ and $B(r), D(r)$ from eqns. 2.1.1-2.1.4 for inner and outer rotors respectively.

When the modulator is brought into a close range of the PM rotor, that is to say, having a ring of ferromagnetic pole-pieces concentric with a PM rotor and with a small

Note: The subscripts 1 and 2 in the above equations denote inner and outer rotors respectively, and subscripts R and θ represent radial and tangential components .

air-gap in between, the PM magnetic fields are modified in both their magnitude and harmonic number due to the effect of the modulator. The permeance function of the soft ferromagnetic pole-piece ring is approximated by the Fourier series expansion as [56]:

$$R_r(r,\theta) = R_{r0}(r) + \sum_{i=1,3,5,\ldots,}^{\infty} R_{ri}(r)\cos\left(iq_s\left(\theta-\omega_s t\right)\right) \tag{2.1.8}$$

$$R_\theta(r,\theta) = R_{\theta 0}(r) + \sum_{i=1,3,5,\ldots,}^{\infty} R_{\theta i}(r)\cos\left(iq_s\left(\theta-\omega_s t\right)\right) \tag{2.1.9}$$

where ω_s, q_s, R_{ri} and $R_{\theta i}$ are respectively the modulator speed, number of modulator pole-pieces, radial and tangential Fourier series coefficients of permeance function.

Thus, the modulation effect of the magnetic fields by the flux modulator is expressed as the product of the ferromagnetic permeance and the magnetic flux density terms. For instance, considering the case of the inner rotor and the flux modulator, without the outer rotor, the modulated flux density distribution at the outer air-gap will be:

$$\begin{aligned} B_R(r,\theta) = {} & R_{r0}\sum_{n=1,3,5,\ldots,}^{\infty} b_r(r)\cos\left(np\left(\theta-\omega_r t\right)+np\theta_0\right) \\ & + \frac{1}{2}\sum_{n=1,3,5,\ldots,}^{\infty}\sum_{i=1,2,3,\ldots,}^{\infty} R_{ri}(r)b_r(r)\cos\left(\left(np+iq_s\right)\left(\theta-\frac{\left(np\omega_r+iq_s\omega_s\right)}{\left(np+iq_s\right)}t\right)+np\theta_0\right) \\ & + \frac{1}{2}\sum_{n=1,3,5,\ldots,}^{\infty}\sum_{i=1,2,3,\ldots,}^{\infty} R_{ri}(r)b_r(r)\cos\left(\left(np-iq_s\right)\left(\theta-\frac{\left(np\omega_r-iq_s\omega_s\right)}{\left(np-iq_s\right)}t\right)+np\theta_0\right) \end{aligned} \tag{2.1.10}$$

$$\begin{aligned} B_\theta(r,\theta) = {} & R_{\theta 0}\sum_{n=1,3,5,\ldots,}^{\infty} b_\theta(r)\sin\left(np\left(\theta-\omega_r t\right)+np\theta_0\right) \\ & + \frac{1}{2}\sum_{n=1,3,5,\ldots,}^{\infty}\sum_{i=1,2,3,\ldots,}^{\infty} R_{\theta i}(r)b_\theta(r)\sin\left(\left(np+iq_s\right)\left(\theta-\frac{\left(np\omega_r+iq_s\omega_s\right)}{\left(np+iq_s\right)}t\right)+np\theta_0\right) \\ & + \frac{1}{2}\sum_{n=1,3,5,\ldots,}^{\infty}\sum_{i=1,2,3,\ldots,}^{\infty} R_{\theta i}(r)b_\theta(r)\sin\left(\left(np-iq_s\right)\left(\theta-\frac{\left(np\omega_r-iq_s\omega_s\right)}{\left(np-iq_s\right)}t\right)+np\theta_0\right) \end{aligned} \tag{2.1.11}$$

A similar set of equations can be obtained for the magnetic flux density distribution in the inner air-gap due to PMs on the outer rotor, the difference being in the number of pole-pairs and the rotational speed. It is important to realize that eqns. 2.1.10 and 2.1.11 contain an infinite number of space harmonics, but the first order terms are sufficient to explain the operational principle of the gear. Essentially, these fundamental harmonic fluxes couple with the same order harmonic fluxes of the corresponding PM rotor, producing torque between the rotors, while the higher order harmonic flux terms may be the source of the cogging and ripple torques. Therefore, considering only the first order harmonics, it can be easily read from the same equations that the spatial modulated

flux density distribution on the other side of the flux modulator consists of three major components:

- The fundamental component that is rotating at the synchronous speed and has exactly the same number of pole-pairs as their original exciting permanent magnet rotor.
- The two other harmonic components with asynchronous speed and a different number of pole-pairs to the parent exciting permanent magnet rotor.

For the operation of a CMG, these asynchronous harmonic components are of great significance, since they can be coupled with a PM rotor with a similar number of pole-pairs to achieve torque transmission at different speeds. Moreover, it can be deduced from eqns. 2.1.10 and 2.1.11 that their pole-pair number and rotational velocity are respectively governed by the following relations:

$$p_{n,k} = |np + kq_s| \tag{2.1.12}$$

$$\omega_{n,k} = \frac{np}{np + kq_s}\omega_r + \frac{kq_s}{np + kq_s}\omega_s \tag{2.1.13}$$

$$n = 1, 3, 5, ...,$$
$$k = 0, \pm1, \pm2, \pm3, ..., \pm\infty$$

The logical comprehension of eqns. 2.1.12 and 2.1.13 implies that any combination with $k = 0$ means exclusion of the ferromagnetic ring, and that the space flux harmonics will always rotate synchronously with the PM rotor. As a result, only a one-to-one gear ratio or a magnetic coupling can be formed from such a configuration. Atallah *et al.* pointed out that the combination with $n = 1$ and $k = -1$ has the asynchronous harmonics with the largest amplitude [33]. Therefore, the modulated space harmonic pole-pairs, which the outer PM rotor must have for the smooth torque transmission, is given by:

$$p_l = q_s - p_h \tag{2.1.14}$$

where p_l and p_h are the pole-pair numbers on the outer and inner rotors, respectively.

As can be observed from Fig. 2.1, this type of gear has three components and one of them must be mechanically earthed while the other two are free to rotate. The conventional design approach is to have either the ferromagnetic pole-pieces ring (flux modulator) or the PM rotor with larger pole-pair number (usually the outer rotor) held stationary. The former option (i.e. $\omega_s = 0$) gives the gear ratio between the asynchronous modulated flux harmonics' and PM rotor's velocity as:

$$\frac{\omega_{n,k}}{\omega_r} = -\frac{p}{q_s - p} \Rightarrow G_r = \frac{\omega_h}{\omega_l} = -\frac{p_l}{p_h} \tag{2.1.15}$$

and the latter arrangement (when $\omega_l = 0$) has the following velocity relation:

$$\frac{\omega_{n,k}}{\omega_s} = \frac{q_s}{q_s - p} \Rightarrow G_r = \frac{\omega_h}{\omega_s} = \frac{p_l}{p_h} + 1 \tag{2.1.16}$$

again, the above equations may be valid for the case when $n = 1$ and $k = -1$, where G_r, ω_h and ω_l are the gear ratio, inner and outer rotors' angular speeds respectively. The negative sign in eqn. 2.1.15 indicates that the two PM rotors rotate in opposite directions, whereas fixing the outer rotor results in the inner rotor and the flux modulator rotating in the same direction with a slightly higher gearing ratio than that in the previous case.

2.2 Magnetically geared machine

In applications where a geared drive-train is demanded, CMGs are at an advantage due to their contactless operation and simplicity when concentrically integrated with a PM machine, instead of a cascaded arrangement that happens to be the only option for other types of gears. Integrating a CMG with a PM synchronous machine forms a more compact magnetically geared permanent magnet (MGPM) machine with high torque density, since the two units are housed in a single volume.

2.2.1 Topologies of magnetically geared machines

The system layout of the MGPM machine investigated in this project is shown in Fig. 2.3. It comprises of an inner high-speed PM rotor, a low-speed ferromagnetic rotor (flux modulator) and an outer-stator with tooth concentrated non-overlapping winding. Apart from

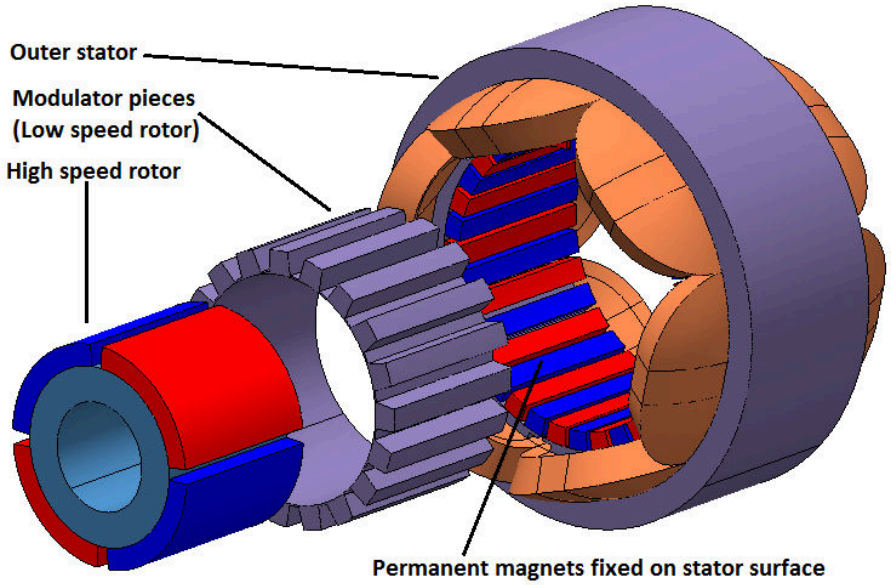

Figure 2.3: Structure of outer-stator magnetically geared machine.

carrying a balanced 3-phase winding, the stator core also supports PMs on its inner surface. These PMs, together with the modulator and high-speed rotor, form the MG part of this machine, while the stator and high speed rotor make up a PM machine.

Various types of MGPM machines exist, but the most prominent configurations include the inner stator and outer stator types shown in Fig. 2.4. From the point of view of the working principle, the inner stator type machine may be seen as a straightforward concept, since the MG and PM machine's flux paths and covered space can be easily seen. However, three air-gaps are involved, which makes its mechanical assembly more complicated. It is shown here only to help illustrate the MGPM machine principle. The

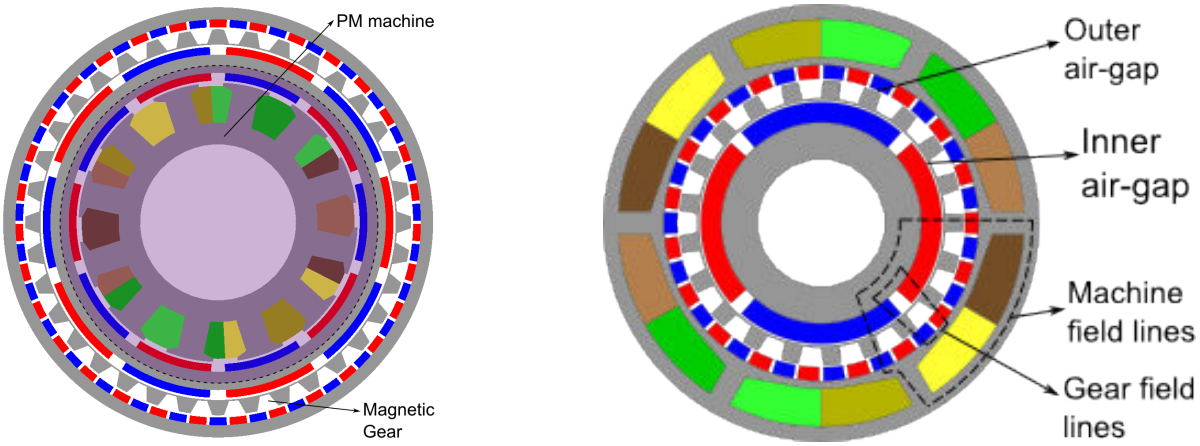

(a) inner stator MGPM machine (b) outer stator MGPM machine

Figure 2.4: Cross section view of MGPM machines.

outer stator type MGPM machine has the MG and PM machine sharing a large part of the magnetic path and the mechanical structure. In the remainder of this chapter the focus will be on this topology.

2.2.2 Working principle of an outer-stator MGPM machine

The working principle of the MGPM machine with an outer-stator can be easily understood by examining the magnetic flux density distribution in the two air-gaps. It has been stated earlier in this chapter, and demonstrated through the Fourier series expansion that the presence of ferromagnetic pole-pieces modulates the magnetic fields into a combination of harmonic components with different rotational speeds and pole-pairs. The radial flux density waveform in the inner air-gap solely produced by PMs fixed on the stator inner surface is shown in Fig. 2.5 together with its harmonic spectra. It can be realized that the dominant two pole-pair field harmonics are generated as a consequence of the presence of the modulator pieces. This modulated two pole-pair field rotates at asynchronous speed relative to its exciting PMs or modulator, and interacts with rotor PMs having the same number of pole-pairs to transfer torque between them.

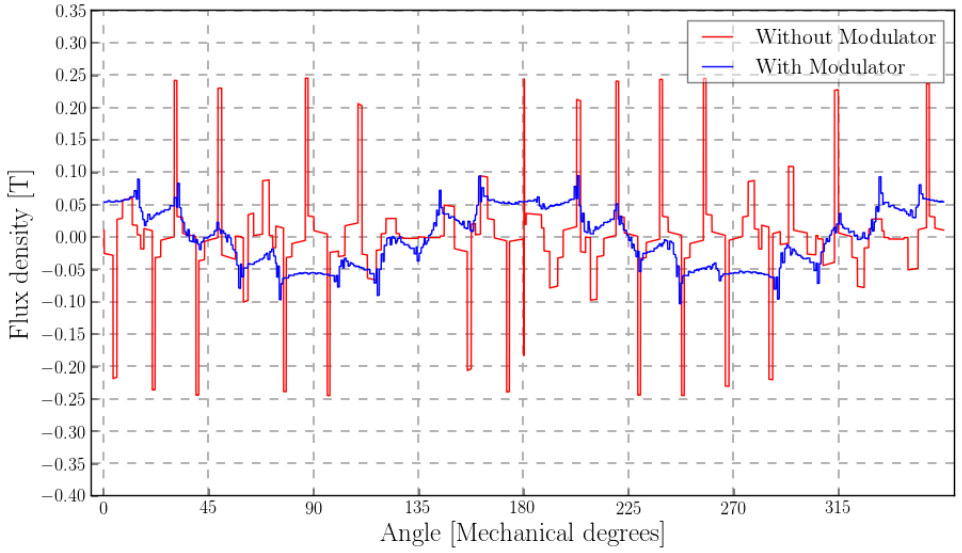

(a) Waveform

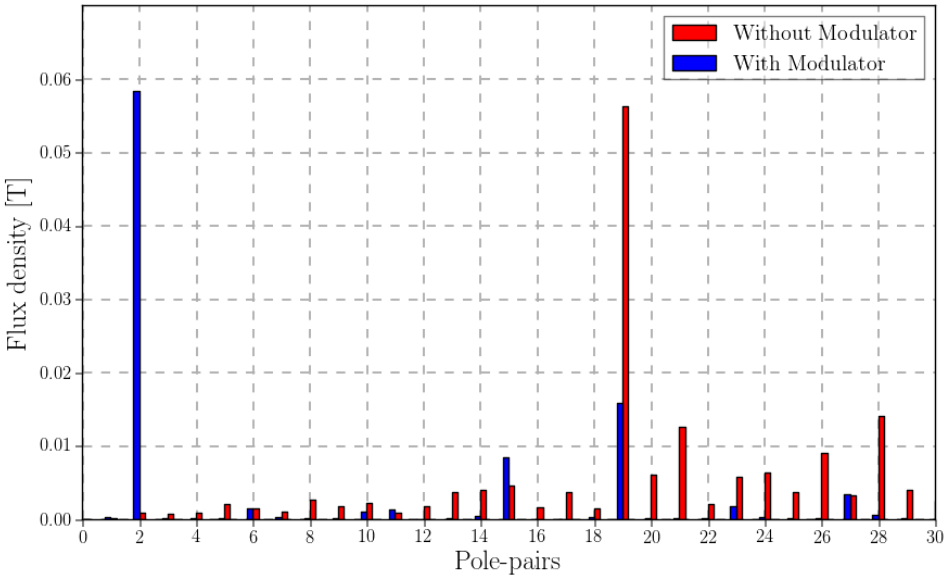

(b) Harmonic spectrum

Figure 2.5: Radial magnetic flux density waveform (obtained from FEM) and its harmonic spectrum in the inner air-gap due to PMs fixed on the stator bore surface, for 4-pole/6-slot MGPM machine.

In the same manner, the radial flux density waveform in the outer air-gap solely excited by PMs on the inner rotor and its corresponding harmonic spectra are shown in Fig. 2.6. In addition to the fundamental two pole-pair harmonic, a second largest 19^{th} pole-pair field can be identified, which emerges as a result of introducing the modulator between the rotors. The 19 pole-pairs field harmonics interact with the fixed PMs, which also have the same pole-pair number for torque transmission.

It is worth noting that while the asynchronous flux harmonics engage with the opposite set of PMs for the gearing purposes, the fundamental two pole-pair harmonic from rotor

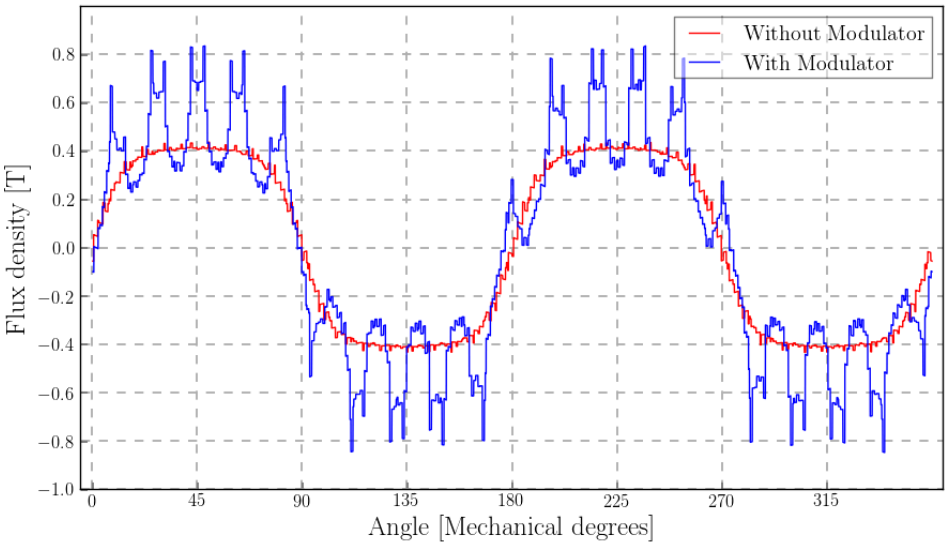

(a) Waveform

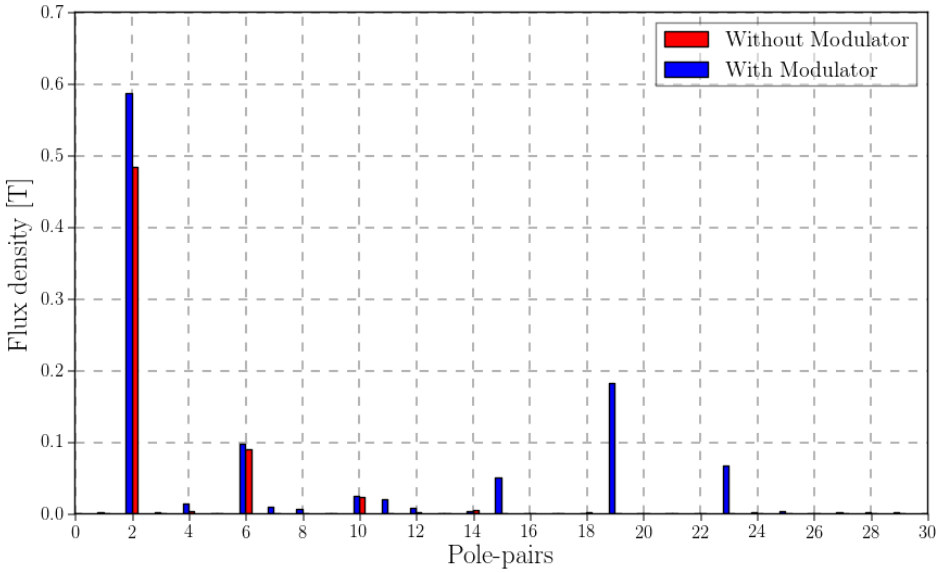

(b) Harmonic spectrum

Figure 2.6: Radial magnetic flux density waveform (obtained from FEM) and its harmonic spectrum in the outer air-gap due to PMs on the rotor, for 4-pole/6-slot MGPM machine.

PMs together with a two pole-pair modulated field from fixed PMs, sums up to a field that couples with stator coils to produce power. That means the stator pole-pairs must match with PM pole-pairs of the inner rotor in order to realize a balanced generator. In this way, it can be further claimed that the machine contains two torque components during its operation:

- The *magnetic torque* that results from the interlocking of the stator and rotor PMs through the *meshing* of their modulated and fundamental harmonic fields, and
- The *electromagnetic torque* which is developed as a consequence of interaction be-

tween combined rotor and stator PMs' fields of the same order and the field of the stator windings.

Therefore, the inner PM rotor can be regarded as an intermediate component between the MG and PM machine. For the steady state operation, the magnetic torque experienced by the inner rotor has to be balanced out with the electromagnetic torque, resulting in zero net torque on this component.

2.2.3 The MGPM machine equivalent circuit analysis

As already mentioned, the MGPM machine is essentially a combination of a CMG and a PM machine. From an electrical machine perspective, an MGPM machine behaves just like any PM synchronous machine. The electrical equivalent circuit is largely the same as that of a synchronous machine with the exception that there is an additional magnetic excitation component from the gear side. Fig. 2.7 shows the per-phase equivalent circuit of an MGPM machine (for generating mode), in which e_m is the electromotive force (EMF), V_ϕ is the terminal phase voltage, R_A is the winding resistance per phase, and L_m and L_e are main and leakage inductances respectively. The core loss resistance R_C is included to take into account the three components of core loss, whereas such losses in the inner high-speed rotor iron and frequency dependent PMs' losses are assumed negligible [71].

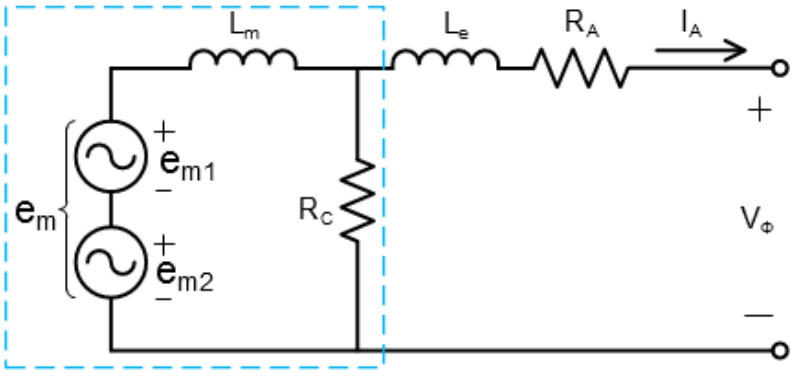

Figure 2.7: Per-phase equivalent circuit of an outer stator MGPM machine.

The no-load EMF induced in the stator windings can be calculated by the time differential of the outer air-gap flux linkage.

$$e_m = \frac{d\lambda}{dt} \tag{2.2.1}$$

Since both sets of PMs contribute to the magnetic field in the two air-gaps, it then follows that the total flux linkage in the outer air-gap is the sum of the flux linkage originating from rotor and stator fixed PMs.

$$\lambda = \lambda_{PM1} + \lambda_{PM2} \tag{2.2.2}$$

It should be noted that the set of PMs fixed on the stator surface has a different number of pole-pairs to the rotor and stator. Therefore, this means the flux responsible for the EMF induction is the result of the fundamental field harmonic from rotor PMs and the modulated harmonic from fixed PMs, both having the same pole-pair number as the stator. This effect of having dual excitation from two sets of PMs is highlighted by the two EMFs (e_{m1}) and (e_{m2}) in Fig. 2.7, which add up to the total stator EMF (e_m) in eqn. 2.2.1.

Moreover, in the circuit on Fig. 2.7, the synchronous inductance is also split into main and end-winding leakage inductances, L_m and L_e respectively. The motivation behind this is that in an FEM based design, the main inductance can always be obtained from 2D FEM analysis, whereas the end-winding inductance needs 3D FEM analysis. Due to the time cost of 3D FEM simulations, end-winding inductance is often calculated analytically.

Several analytical methods for performing end-winding inductance in non-overlap winding PM machines are evaluated in [72], which showed that the difference between 3D and 2D FEA calculated flux linkages can be used to accurately predict the end-winding inductance. Consequently, the 3D FEM approach was followed in the current study for the calculation of this parameter. Therefore, all the equivalent circuit parameters enclosed by the dashed lines in Fig. 2.7 can be approximated from the 2D FEM method alone.

On the other hand, it may be challenging to perform some of the calculations in the a-b-c stator reference frame since the flux linkages are vary with time. To simplify this, the instantaneous a-b-c stator values (i.e flux, currents and voltages) are projected onto dq-axis rotor frame. This is carried out through the use of power-invariant dq0 transformation matrix, defined as:

$$K_{dq0} = \sqrt{\frac{2}{3}} \begin{bmatrix} \cos\theta & \cos\left(\theta - \frac{2\pi}{3}\right) & \cos\left(\theta + \frac{2\pi}{3}\right) \\ -\sin\theta & -\sin\left(\theta - \frac{2\pi}{3}\right) & -\sin\left(\theta + \frac{2\pi}{3}\right) \\ \frac{1}{\sqrt{2}} & \frac{1}{\sqrt{2}} & \frac{1}{\sqrt{2}} \end{bmatrix} \tag{2.2.3}$$

The product of the dq0 transformation matrix and three phase stator values gives their corresponding dq-axis equivalent values. Fig. 2.8 illustrates the resulting steady state dq-axis equivalent circuits.

$$\left[S_{dq0}\right] = \left[K_{dq0}\right]\left[S_{abc}\right] \tag{2.2.4}$$

In these circuits, λ_d, λ_q and I_d, I_q are the dq-axis main flux linkages and currents respectively, and the end-winding flux linkages are still treated separately.

The speed dependent voltages are determined by:

$$\begin{aligned} E_d &= -\lambda_q \cdot \omega_r \\ E_q &= \lambda_d \cdot \omega_r \end{aligned} \tag{2.2.5}$$

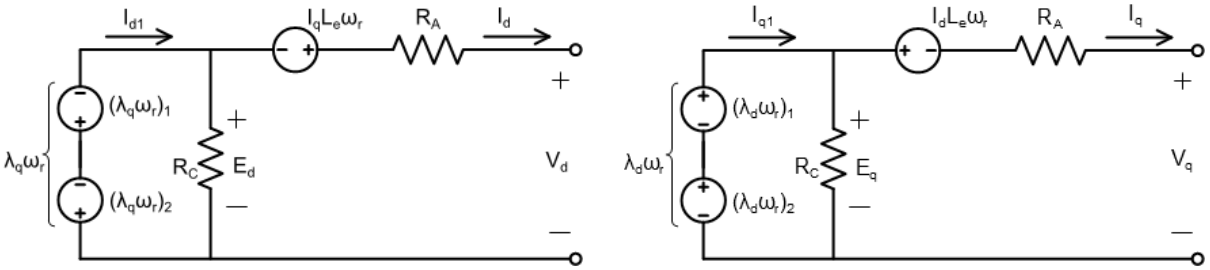

(a) d-axis (b) q-axis

Figure 2.8: d- and q-axis equivalent circuits.

When needed, the same procedure may be used to convert from dq-axis to stator reference frame, with the help of the inverse dq0 matrix.

$$\left[S_{abc}\right] = \left[K_{dq0}\right]^{-1} \left[S_{dq0}\right] \tag{2.2.6}$$

The hybrid method consisting of classical machine theory and FEM analysis is used for the computation of the machine equivalent circuit parameters and performance. The FE analysis programs used in this study require the rotor's steady state speed and the stator's three-phase currents as some of the inputs. In order to make sure that the machine is still within the limits of its designed cooling methods, the current is specified either in terms of current density (J) or calculated from the copper loss constraints.

The latter method requires prior knowledge of both copper loss (P_{cu}) limits and per phase equivalent resistance. Then the current amplitude is computed from eqn. 2.2.7.

$$I = \sqrt{\frac{2\,P_{cu}}{3\,R_s}} \tag{2.2.7}$$

For the former method, the standard current density value associated with a specific cooling technique is used, for instance, $5\,\mathrm{A/mm^2}$ for natural air cooling. The exact maximum current amplitude in each conductor is calculated from the following equation:

$$I_{mag} = \frac{J \cdot A_{slot} \cdot K_f}{n_{cond}} \tag{2.2.8}$$

$$K_f = \frac{A_{cond} \cdot n_{cond}}{A_{slot}}$$

where A_{slot}, A_{cond}, n_{cond} and K_f are available slot area, one conductor cross sectional area, number of series conductor turns per phase and slot filling factor, respectively.

The current magnitude (I) is provided as the q-axis value since the d-axis value is approximated to be zero on the assumption that the load connected to the generator is balanced and purely resistive, and for the general approximation that the d- and q-axis inductances are almost equal in surface mounted PM rotors, which means the d-axis

current has an insignificant effect on the torque. Then the dq-axis current is converted into three phase instantaneous magnitudes via the inverse dq0 transformation. It is important to align the rotor's direct axis with the stator's reference phase axis (normally phase a) during FE analysis as this simplifies the post-analysis computation, or otherwise the angle difference between them must be correctly determined.

After the machine's FE simulation process is completed, certain parameters, such as flux linkages, can readily be procured from FEA solution and transformed into their dq-axis reference frame for further post-processing steps.

The time averaged eddy-current and hysteresis core losses (P_c) are also obtained straight from the FEA solution. Then, the stator core resistance (R_C) can be calculated from a rearranged version of ohm's law equation as:

$$R_C = \frac{3{E_a}^2}{P_c} \tag{2.2.9}$$

where the per phase EMF rms value is given by:

$$E_a = \sqrt{\frac{{E_d}^2 + {E_q}^2}{2}} \tag{2.2.10}$$

The single phase temperature dependent armature resistance, with the skin effect ignored, is reckoned by:

$$R_A = \frac{2\rho_T \left(l + l_e\right)}{A_{cond}} n_{cond} \tag{2.2.11}$$

where ρ_T, l and l_e are the resistivity of the conductor at teperature T, stator stack length and single side end-winding length.

2.2.4 Performance calculation of the MGPM

From the equivalent circuits in Fig. 2.8, the dq-axis terminal voltage components and their amplitude V_s, are obtained:

$$\begin{aligned} V_d &= E_d + L_e I_q \omega_r - I_d R_A \\ V_q &= E_q - L_e I_d \omega_r - I_q R_A \\ V_s &= \sqrt{V_d^2 + V_q^2} \end{aligned} \tag{2.2.12}$$

In the same way, the dq-axis current components are deduced from the circuit as:

$$\begin{aligned} I_{d1} &= I_d + \frac{E_d}{R_C} \\ I_{q1} &= I_q - \frac{E_q}{R_C} \\ I_{s1} &= \sqrt{I_{d1}^2 + I_{q1}^2} \end{aligned} \tag{2.2.13}$$

From the FE solutions, the inductance is generally determined from the flux (λ) and current (I) values as:

$$\begin{aligned} L_q &= \frac{\lambda_q}{I_q} \\ L_d &\cong L_q \end{aligned} \tag{2.2.14}$$

Knowledge of equivalent circuit parameters enables computation of output torque and power. The high-speed steady-state average electromagnetic torque and generated apparent power of the machine are respectively calculated from the following equations:

$$T_{EM} = p_h \left(\lambda_d I_q - \lambda_q I_d\right) \tag{2.2.15}$$

$$\begin{aligned} S &= V_d I_d + V_q I_q \\ &= \frac{3}{2} V_s I_s \end{aligned} \tag{2.2.16}$$

With both the instantaneous output current and voltage known, the output active power is given by:

$$P_{out} = S \cdot P_f \tag{2.2.17}$$

where P_f is the power factor obtained from the difference in voltage and current angles.

The machine efficiency is defined as the percentage ratio of output active electrical power over input mechanical power:

$$\eta = \frac{P_{out}}{P_{in}} \times 100\% \tag{2.2.18}$$

Since the flux modulator is used as the mechanical input terminal of the generator, the input power may be calculated from this component's torque and rotational speed (n_s). The modulator's torque (τ_s) is obtained from the FEM solution, whereas its speed should be an input to FE simulation.

$$P_{in} = \frac{2\pi}{60} \tau_s n_s \tag{2.2.19}$$

The difference between the input and output powers is brought about by the internal machine losses illustrated by the power diagram in Fig. 2.9.

$$P_{out} = P_{in} - P_{loss} \tag{2.2.20}$$

These total losses are described by eqn. 2.2.21, although the common practice is to ignore mechanical losses during the preliminary design. That means that the efficiency calculation at electromagnetic optimization stage is dependent on the copper and core losses, while the frictional and windage losses are considered in the final design.

$$P_{loss} = P_{cu} + P_c + P_{friction} + P_{windage} \tag{2.2.21}$$

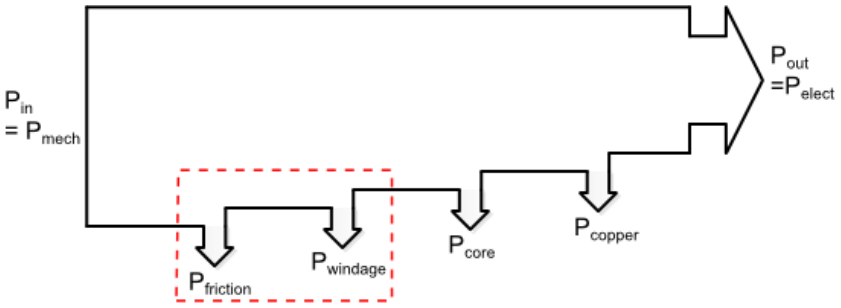

Figure 2.9: MGPM machine power flow diagram.

In this project, both copper and core losses are acquired from the FEA solution. Their analytic equations are also provided to show how they relate to other machine parameters, while the formulation of bearing and windage losses is excluded.

$$P_{cu} = 3I_A^2 R_A \tag{2.2.22}$$

and core losses

$$P_c = k_h f B_m^{\alpha} + k_e f^2 B_m^2 + k_{exc} f^{1.5} B_m^{1.5} \tag{2.2.23}$$

where B_m is the maximum flux density, f is the flux frequency, and k_h, k_e, k_{exc} and α are the material specific loss coefficients.

Chapter 3

Design and Optimisation

The determination of electrical design parameters and finite element modelling of the magnetically geared machine are described in this chapter. The selection of a suitable pole/slot combination for both the gear and stator in order to achieve a high winding factor and reduce cogging torque are first described. Subsequently, the modelling tools and design considerations are explained. Furthermore, the optimization procedure and employed algorithm are elaborated on in order to provide a good understanding of how the final machine dimensions are established. Lastly, the simulation results of the optimized machine are also presented.

3.1 Pole and slot numbers selection

The stator design is begun by selecting an appropriate winding configuration and determining a good pole-slot combination. With regard to the dimension constraints in this project, especially the stack length, the double-layer non-overlap winding is considered to be a suitable option. Compared to normal overlapping windings, non-overlap windings are generally acknowledged to have advantages such as a lower risk of phase-to-phase short circuit connection and shorter end-winding, which directly translate into a smaller copper volume and lower losses. In addition, this type of winding also simplifies the manufacturing process, hence saves time. It is obvious that double-layer non-overlap winding with each coil concentrated around one tooth are a fractional slot type of winding. Besides having a lower winding factor when compared to integral slot winding, they are also known for their rich harmonic contents, which gives rise to core losses.

Accordingly, the choice of the stator pole/slot combination has to be made with the aim of achieving the best possible fundamental winding factor at the same time as achieving minimum magnitudes of unbalanced magnetic forces within the stator. The number of

slots per pole per phase (q) defined by eqn. 3.1.1, which is a useful term for this purpose.

$$q = \frac{Q}{m \times 2p} \tag{3.1.1}$$

where Q, m and p represent the number of stator slots, phases and pole-pairs, respectively.

For this type of winding, Skaar *et al.* found that the pole/slot combination with decent q values lies in the region $1/4 < q < 1/2$, while the cases with $|m - 2p| > 1$ result into acceptable or symmetrical radial forces [73]. With this in mind, and also considering the small diameter of the proposed model, it was decided that 4/6 or 6/9 are feasible combinations since they can easily be accommodated within the small available stator volume. Moreover, the fact that the inner rotor is shared between the gear and the PM machine, means that the stator pole-pair number has a direct impact on the gear ratio. That is, the higher the stator pole-pair number the larger the number of PMs fixed on the stator surface so as to maintain a certain gear ratio. The practical limit for this number may be imposed by manufacturability and PM utilization. Figure 3.1 shows the variation of the maximum torque capacity with the parameter sweep through the pole-pair number of PMs fixed on the stator, while the stator or rotor pole-pairs are kept at 4 and 6. It

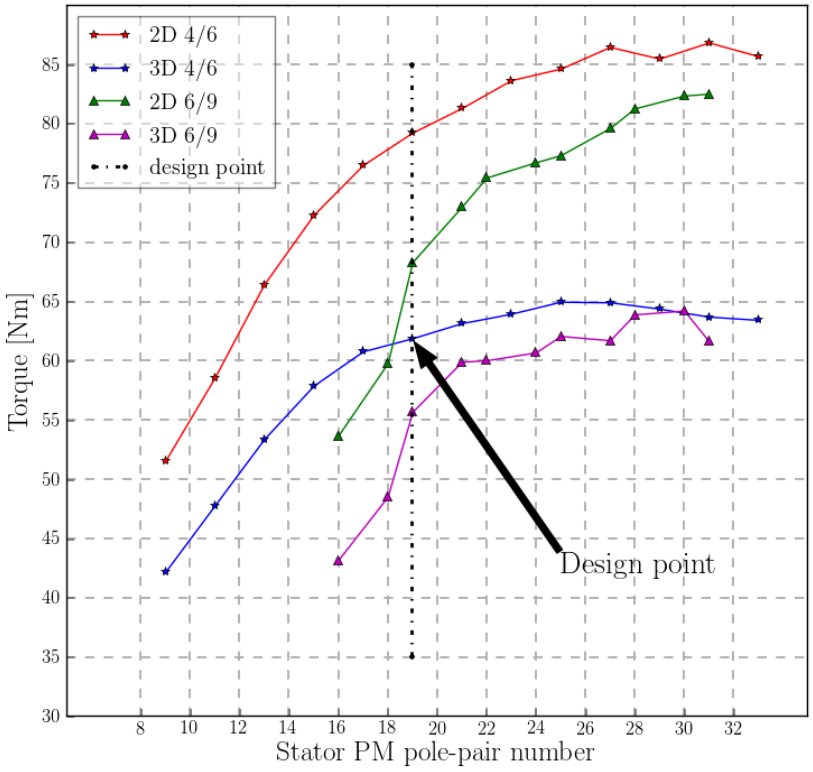

Figure 3.1: Maximum torque as a function of stator magnet's pole number.

should be noted that at almost the same pole-pair number, the 4/6 always gives better torque than the 6/9 combination. It can also be observed that the peak torque of the machine increases as the gear ratio increases. However, all the gradients of the graph

decline as the pole-pair number increases, which indicates that an optimum gear ratio exists above which the gain in torque by increasing gear ratio becomes insignificant. This may be attributed to the severe leakage flux loss associated with the high number of PM poles.

On the other hand, for both the gear and generator, the best pole-pair combination cannot be determined on the stall torque alone, but the ripple or cogging torque also play an important role in the selection criteria. The cogging torque factor f_c is employed to indicate the severity, but not the actual value of the cogging torque [74]

$$f_c = \frac{2p_h q_i}{\mathrm{LCM}(p_h, q_i)} \tag{3.1.2}$$

where p_h is the number of inner rotor pole-pairs, q_i represents either ferro-magnetic pole-pieces q_s, fixed PMs pole-pairs p_l or stator slots Q. LCM is the lowest common multiple.

A larger LCM value is preferred as it results in a higher order and lower magnitude of cogging harmonics, hence less ripple [75]. However, the relatively low number of stator pole/slot configuration selected in the foregoing design already limits the freedom to find very high LCM values.

A 4-pole, 6-slot stator was chosen as the final design, and Fig. 3.1 was used to select the optimal pole number of the PMs on the stator surface. The region where the graph begins to flatten is believed to have the required number since there is little torque gain after that, for this reason 19 pole-pairs was considered the best option.

The method presented in [76] was followed to determine the stator winding layout shown in Figure 3.2, from which the fundamental winding factor ($K_{\omega 1}$) was calculated through by means of following procedure [76]:

$$\begin{aligned} K_{\omega 1} &= \frac{1}{n_l Q/3} \left| \sum_{i=1}^{2Q/3} S(i) e^{j\frac{\pi 2p}{Q}|S(i)|} \right| \\ &= \frac{1}{2 \times 6/3} \left| -e^{j\frac{\pi \times 4}{6}} + 2e^{j\frac{\pi \times 4}{6}2} - 4e^{j\frac{\pi \times 4}{6}4} + 5e^{j\frac{\pi \times 4}{6}5} \right| \\ &= 0.866 \end{aligned} \tag{3.1.3}$$

$S(i) = [-1, 2, -4, 5]$ as derived from winding layout, and Q is number of stator slots, n_l is number of winding layers and equal to 2 for the double layer winding.

With the number of pole-pairs on the inner rotor (p_h) and outer rotor or fixed PMs on the stator (p_l) known, the number of modulation pole-pieces is calculated from eqn. 2.1.14 as:

$$q_s = p_h + p_l \Longrightarrow q_s = 21$$

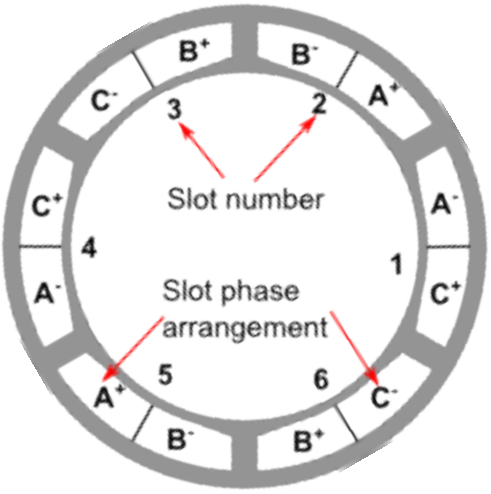

Figure 3.2: Stator winding layout.

and the gear ratio between the modulator and inner rotor speeds can also be obtained from eqn. 2.1.16 by:

$$G_r = \frac{\omega_h}{\omega_s} = \frac{p_l}{p_h} + 1$$
$$= \frac{19}{2} + 1 = 10.5$$

The cogging torque factor between the modulator pieces and the inner rotor is then:

$$f_c = \frac{2 \times 2 \times 21}{\text{LCM}(2, 21)} = 2$$

And the factor between the inner rotor and the stator slots is given by:

$$f_c = \frac{2 \times 2 \times 6}{\text{LCM}(2, 6)} = 4$$

Normally, a unity factor would be preferred since it predicts the minimum cogging/ripple torque. Thus with factors of 2 and 4, relatively high cogging torque can be expected in this machine. These factors, together with the fact that $G_r = 10.5$ are in good agreement with the findings of Nicholas *et al.* that gearing ratios with whole and half orders of numbers perform worst in terms of torque quality [75]. A more fractional order of ratio would result in lower cogging torque, but, as previously stated, the stator pole/slot combination already sacrificed the chances of achieving such a ratio.

In order for a machine with a gearing ratio of 10.5 and a 4-pole stator to have an output frequency close to 50 Hz at its operating point, the rated input shaft speed of 150 rpm was selected. Then, the inner rotor angular mechanical speed will be:

$$\omega_h = G_r \times 150 = 1575 \,\text{rpm}$$

and this gives the fundamental operating electrical frequency of:

$$f_e = \frac{p \times \omega_h}{60} = \frac{2 \times 1575}{60} = 52.5\,\text{Hz}$$

All the calculated parameters which define the machine and its rated conditions are shown in Table 3.1, and will be used as inputs to the FE model in the next section.

Table 3.1: Machine key parameters.

	Parameter Description	Symbol	Value
Generator	Number of slots	Q	6
	Number of poles	p	4
	Number of phases	m	3
	Winding layers	n_l	2
	Rated frequency	f_e	52.5 Hz
	Winding factor	$K_{\omega 1}$	0.866
Gear	Inner rotor pole-pairs	p_h	2
	Fixed PM pole-pairs	p_l	19
	Modulator pole-pieces	q_s	21
	Gearing ratio	G_r	10.5
	Rated speed	n_{rpm}	150 rpm

3.2 Finite element analysis

Finite Element Method (FEM) is used in this project to perform field calculations of MGPM machine since its performance cannot be accurately solved through the analytical approach only. FEM entails the solving of linear and non-linear partial differential or integral equations describing magnetic vector potential variation in small area/volume units called finite elements, which are themselves a discretization of a machine's cross sectional area or total volume. Compared to analytical techniques, the FE method allows the modeling of more intricate geometries and takes into account the non-linearity of materials without too many restricting assumptions.

The two FEM packages employed to create this design environment are SEMFEM and MagNet version - 7.3. SEMFEM is an in-house developed FEM program that is faster and includes other features unavailable in MagNet, although it is limited to only static 2D FE simulations. MagNet is a numerical analysis software from Infolytica Corporation that can process magnetic or electromagnet fields solutions, and is capable of dealing with both 2D and 3D FE static and transient simulations [77].

Several parameters have to be set in order to enhance the accuracy of the FEM solution to some satisfactory level. One of those parameters which is the most important and

sensitive is the size of the finite elements (mesh). The mesh size affects the degree of calculation accuracy as well as the speed of the simulation. Hence, it may be beneficial to find a balance between the computational time and accuracy of FEM calculation. This is achieved by defining different mesh sizes at different model regions, finer mesh in air-gaps and other regions with a large flux gradient, and rougher mesh in areas where the flux is almost constant.

Secondly, correct boundary conditions should be applied to ensure the solution validity. Since a typical MGPM machine exhibits no magnetic periodicity, the full machine has to be modelled with an air-box representing an artificial outer boundary surrounding the model. Dirichlet boundary condition was defined on the surfaces of the air-box. In addition, the flexibility offered in FEM packages to use iterative solving techniques such as Newton-Raphson method can be used to good advantage by adjusting the number of iterations, polynomial order and convergence tolerance to further improve solution accuracy.

Another important factor to take into consideration is the correct setting of each component material property. Ferromagnetic materials have non-linear characteristics, so a BH curve fit has to be coupled with each material used in the model. Besides several materials that are already defined in MagNet, a new material modified to have conductivity coefficient in the third dimension was used to include leakage flux losses in the 3D simulations. In addition, the permanent magnet type, material and magnetization characteristics were set.

The FEM flow diagram followed in this modelling is shown in Fig. 3.3. Python script is used as the interface to interact with FE programs by sending pre-processing commands and extracting the solution results, as well as the data processing environment in the post-processing stage. The input and output data are stored in an external tab delimited text (.txt) file for later analysis and to make it accessible to any other programs outside the current platform, as will be shown in the optimization section.

The machine specifications obtained from the previous section, together with the geometric parameters in Table 3.2 are inputs to the FE program. Furthermore, the geometric variables are clearly explained in Fig. 3.4. Once the simulation process is completed, the output is extracted for performance analysis done in the post-processing stage.

3.3 Design optimization

Electrical machines' numerical optimization may be seen as the recursive process whereby a machine is repeatedly simulated in finite element analysis, evaluated for an output performance and its parameters adapted to achieve an improved objective function while

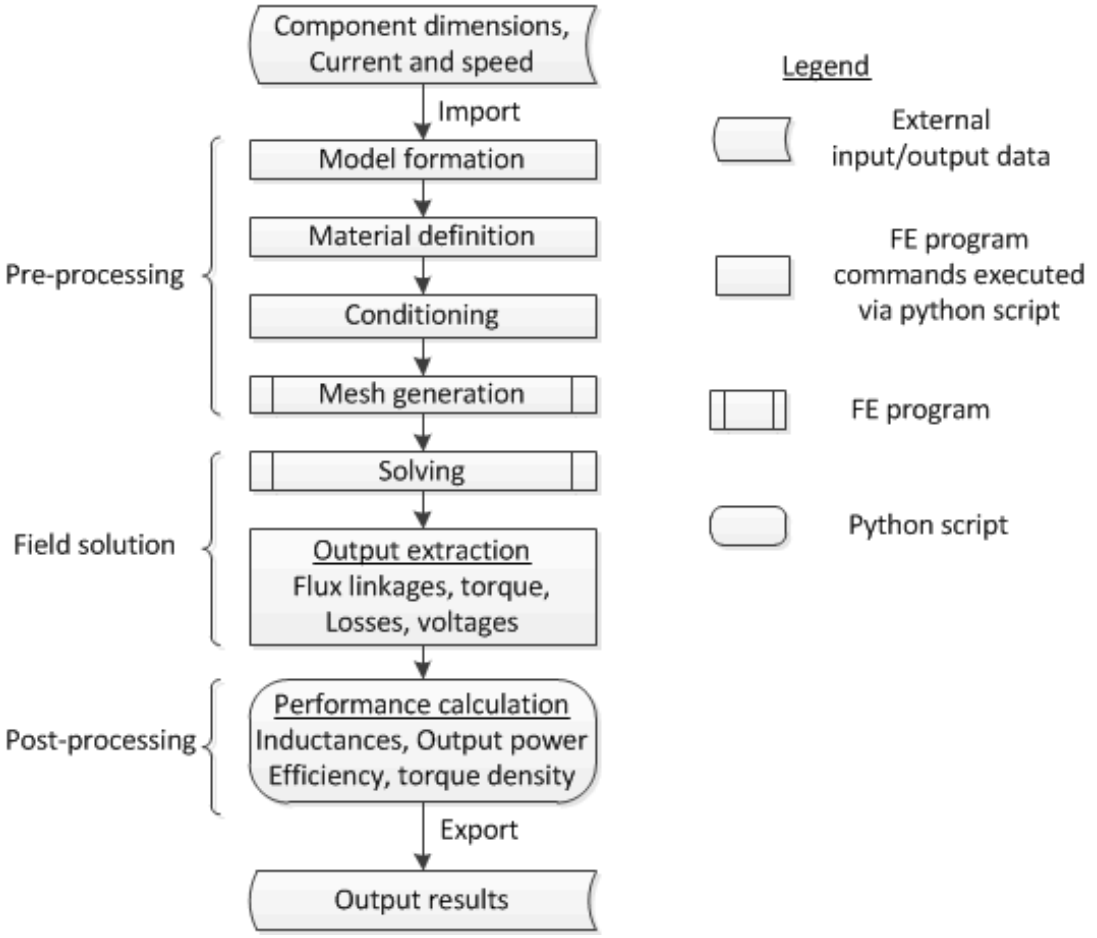

Figure 3.3: FEM flow diagram.

within some dimensional or characteristic constraints. There are several optimization techniques, which in most instances, are grouped as gradient-based and non-gradient based algorithms. The latter group is generally praised of its ability to reach a global optima, though it can be time and memory expensive for a very large sets of optimization variables. Gradient-based algorithms are time efficient, but are likely to be trapped in local optima due to their direct dependence on the function gradient at each step. To ensure that a global optimum is obtained under this techniques, final results provided by multiple optimization iterations performed from different starting points are expected to be within a fine margin. Thus, considering the number of variables and constraints involved in this project, a gradient-based algorithm was chosen since it provided results with an adequate degree of accuracy.

3.3.1 Optimization algorithm

The optimization of an electrical machine is naturally a constrained engineering problem. Within the category of gradient-based optimization algorithms, there are various direct methods to deal with such kinds of constrained multi-variable problems. These include, amongst many others, sequential linear/quadratic programming and a modified method of

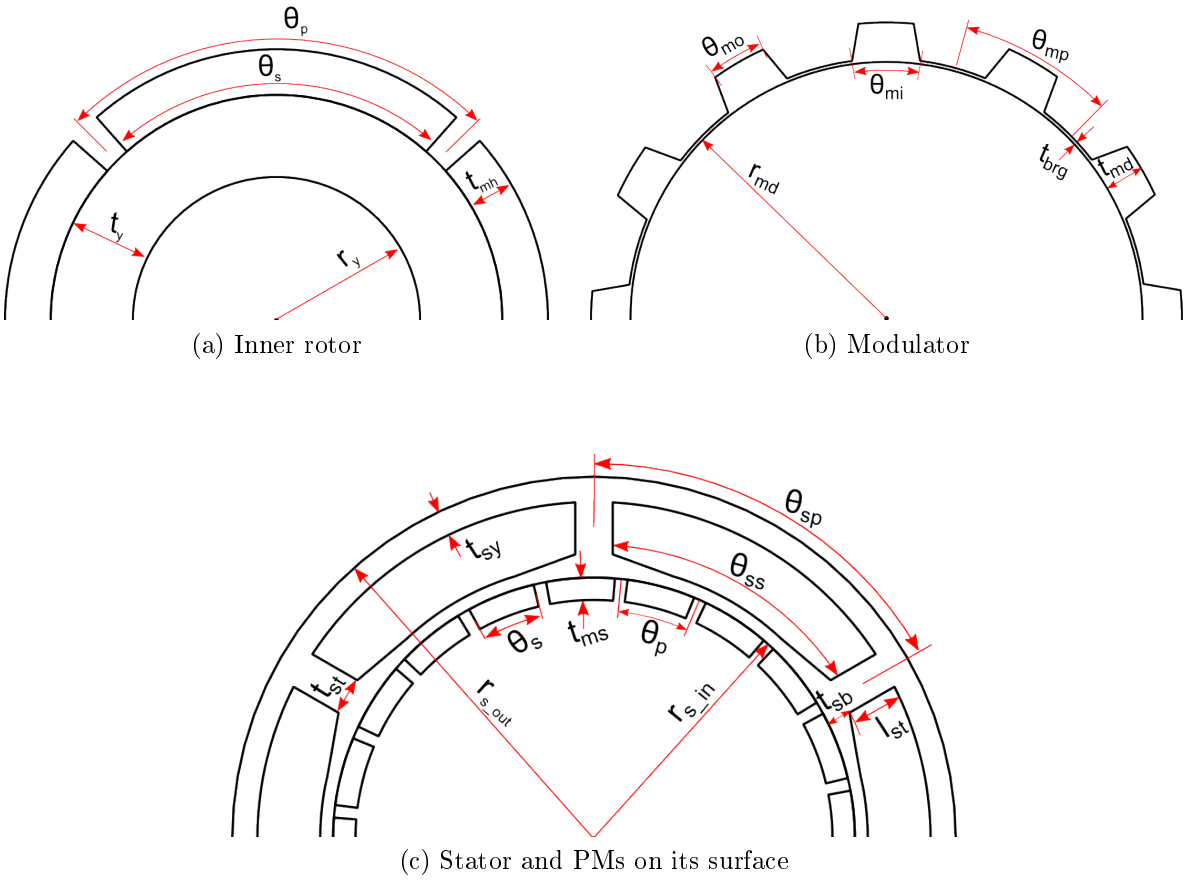

(a) Inner rotor

(b) Modulator

(c) Stator and PMs on its surface

Figure 3.4: Geometric variables input to FEM.

feasible directions (MMFD) [78]. Since the foregoing optimization involved both equality and inequality constraints, MMFD was a method of preference. Figure 3.5 illustrates the flow diagram of this method. It relies mainly on the line search to determine the direction which can quickly reduce the objective function while maintaining the feasible design [78, 79].

The following explanation of the employed optimization algorithm is adapted from [78, 79], hence it can be revisited for more details. At the beginning, the MMFD optimization process requires a set of initial design variables, and the objective function is evaluated from them. It is time efficient if such an initial design is feasible, otherwise more time is wasted in driving the optimizer back to the feasible region. At each process iteration (k), the objective function and inequality constraints are evaluated on the current design variables. Then the crucial constraints at that step are identified. The objective function and constraints' gradients are very helpful information for the determination of a search direction. If there are no active or violated constraints, the Fletcher-Reeves conjugate method (*eq.* 3.3.2) or the "direction of steepest descent" (*eq.* 3.3.1) defined by the negative gradient vector may be used to speed up the process. The latter is used at the initial stages of the process while the former is applied at any stage where the condition holds.

Table 3.2: Geometric input variables.

Component	Variable Description	Variable Symbol
High Speed Rotor	yoke inner radius	r_y
	yoke thickness	t_y
	magnet thickness	t_{mh}
	magnet pitch	θ_p
	magnet span	θ_s
Modulator	inner radius	r_{md}
	thickness	t_{md}
	bridge thickness	t_{brg}
	pole-pitch	θ_{mp}
	pole inner width	θ_{mi}
	pole outer width	θ_{mo}
Stator and PMs on its surface	outer radius	r_{s_out}
	inner radius	r_{s_in}
	tooth length	l_{st}
	tooth thickness	t_{st}
	tooth base thickness	t_{sb}
	yoke thickness	t_{sy}
	slot pitch	θ_{sp}
	slot pole	θ_{ss}
	magnet thickness	t_{ms}
	pole pitch	θ_p
	pole span	θ_s

But when the active constraints are met, the optimizer strives to find a search direction that improves the design while going in parallel to the constraint.

$$S^k = -\nabla F(X^{k-1}) \tag{3.3.1}$$

$$S^k = -\nabla F(X^{k-1}) + \beta S^{k-1}, \tag{3.3.2}$$

where

$$\beta = \frac{\left|\nabla F(X^{k-1})\right|^2}{\left|\nabla F(X^{k-2})\right|^2}$$

After the search direction is obtained, the constraints' gradients are used to estimate the reasonable value of the distance or step (α^*) to be moved in that direction. The design variables are then updated with the new values that lead in a direction towards the optimum while also being tangential to or moving away from the constraints. The optimization process continues iteratively until the objective function is completely minimized/maximized, the maximum number of iterations is exceeded or there are no feasible solutions.

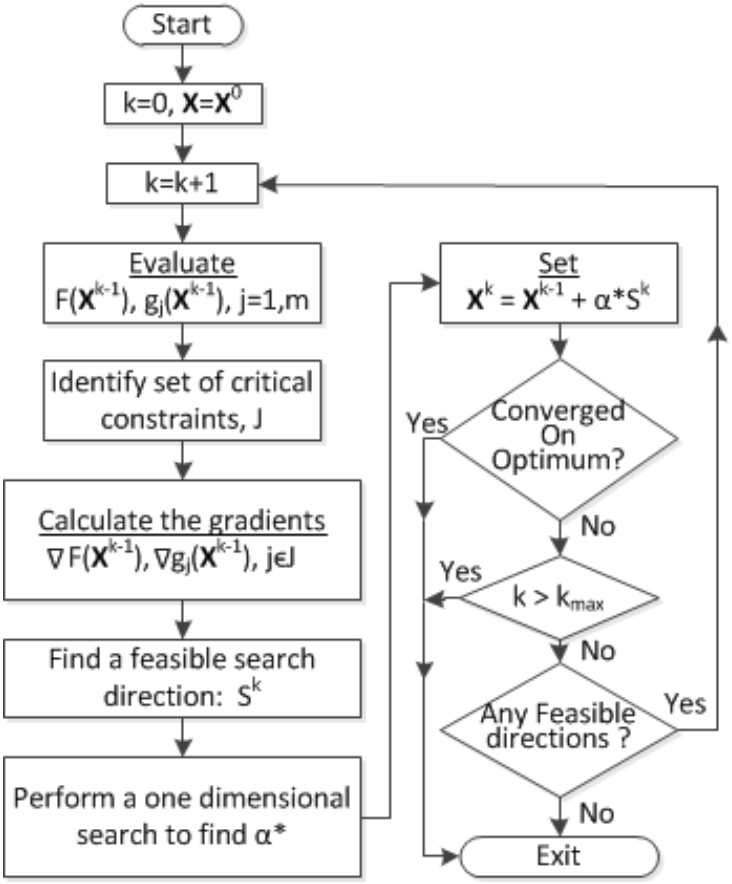

Figure 3.5: Optimization flow diagram [78].

3.3.2 Optimization procedure

The optimization of a magnetically geared machine is a non-linear constrained problem that depends on many variables explained in the previous subsection. In order to determine the optimum values of these parameters, an optimization problem has to be converted into a mathematical statement with an objective function that can be minimized or maximized within certain requirements. For the current design, the optimization statement is formulated as shown below:

$$\begin{aligned} \text{Maximize:} \quad & F(\mathbf{X}) = \text{Torque } (T_M)/\text{active mass} \\ \text{Subject to:} \quad & T_E \geq 0.8 \times T_M \\ & t_{mh}/t_{ms} \leq 1.5 \\ & J \leq 5\,\text{A/mm}^2 \end{aligned} \tag{3.3.3}$$

where T_E is the electromagnetic torque between the inner rotor and the stator, T_M is the magnetic torque between the inner rotor and the PMs fixed on the stator surface, t_{mh} and t_{ms} are corresponding thicknesses of the rotor and stator magnets and, $\mathbf{X}$ represents the vector of variables in Table 3.2.

For an MGPM machine, it may be of interest to optimize several characteristic parameters. It was found more reasonable to aim for the the active machine weight and torque

capability. This is because the active weight contributes to both the machine cost and portability, and it makes more sense to seek for maximum possible torque at any given machine dimensions. At first glance, it seems that a multi-objective set-up is necessary for these two targets, but by expressing the objective function as a fraction of the maximum torque to active mass, it is believed that two goals are achieved simultaneously, hence a single objective optimization is sufficient. By maximizing this combined objective function, the numerator (torque) is increased while the denominator (active mass) is decreased.

The copper losses are dominant over frequency dependent losses in this machine because the operating frequency is low and the involved ferro-magnetic material is less due to small machine volume. Consequently, the efficiency is mainly dependent on conductor ohmic losses. To ensure that a satisfactory efficiency is still maintained at any optimization step, a current density is constrained to limit the copper losses while the eddy-current and hysteresis loss are assumed to be negligible. A $5\,\mathrm{A/mm^2}$ was chosen since the machine is to be naturally air-cooled.

The PMs on the stator surface are vulnerable to permanent demagnetization due to the opposing magnetic fields from the inner rotor PMs and the currents in the stator coils. In addition, the stator temperature speeds up this adverse process since the coils and the PMs are on the opposite surfaces of the stator, which means the heat transfer between them is easily realized. As a safety factor, the thickness ratio of the two PM sets was constrained so that they don't demagnetize each other.

The average electromagnetic and magnetic torques can be maximized at the expense of each other, leading to an imbalanced design. To guarantee the optimal matching of the gear and the machine, the ratio of these two torques, defined as the stator load factor, has to always be confined within some boundaries. Since the objective function is directly dependent on the maximum input magnetic torque capacity, the electromagnetic torque is restricted to be at least 80% of the magnetic torque so that most of the input mechanical power is converted into electrical energy.

The argument of an objective function ($\mathbf{X}$) represents the vector of design variables shown in Table 3.3 together with their ranges; all length dimensions are in millimeters. As for the PMs, the upper limits on lengths and pole-arcs are set to reduce the inter-leakage flux between adjacent PMs. On the other hand, the minimum lengths for any other component including the PMs is set to ensure their mechanical integrity so that they will be easy to manufacture. The theoretically calculated parameters and specifications in Table 3.1 and the fixed geometric parameters in Table 3.4 are included for the complete definition of the machine and search range during optimization. It should also be noted that the temperature and material characteristics were kept constant throughout the optimization process.

Table 3.3: Geometric input variables and their constraints.

Parameter	Range
Magnet thickness	$2.5 \leq t_{mh}$ *or* $t_{ms} \leq 8$
Magnet span to pole-pitch ratio	$0.667 \leq \theta_s/\theta_p \leq 0.9$
Rotor yoke inner radius	$12 \leq r_y$
Rotor yoke thickness	$8 \leq t_y \leq 15$
Modulator thickness	$6 \leq t_{md} \leq 15$
Modulator bridge thickness	$0.3 \leq t_{brg} \leq 1$
Inner modulator pole width ratio	$0.3 \leq \theta_{mi}/\theta_{mp} \leq 0.8$
Outer modulator pole width ratio	$0.3 \leq \theta_{mo}/\theta_{mp} \leq 0.8$
Stator tooth length	$10 \leq l_{st}$
Stator tooth thickness	$6 \leq t_{st}$
Stator tooth base thickness	$1.5 \leq t_{sb}$
Stator yoke thickness	$4 \leq t_{sy}$
Stator slot pole to pitch ratio	$0.5 \leq \theta_{ss}/\theta_{sp} \leq 0.95$
Stator slot filling factor	$0.3 \leq S_{ff} \leq 0.55$

Table 3.4: Fixed geometric variables of the MGPM machine.

Outer diameter of the machine (mm)	140
Stack length of the machine (mm)	50
Air-gap length (mm)	0.7

VisualDOC version - 7 from VR&D Inc. was employed as the design tool which provides and executes the selected optimization algorithm on the given problem. It is coupled with the machine analysis program through the external files accessible to both of them. The optimization process was performed with a 2D FE static analysis of the machine at a maximum load point of the gear, and SEMFEM was chosen rather than MagNet for this purpose. The 3D FE static solver in MagNet was used to verify static performance of every optimum solution from VisualDOC, and a 2D FE transient simulation was done to analyze the transient performance. Figure 3.6 demonstrates how the three software tools were integrated and used to create a design environment. The optimized design variables are listed in Table 3.5.

3.3.3 Optimization results

The static torque-angle characteristics of the MG part of this machine are shown in Fig. 3.7. In order to conduct this simulation analysis, the stator currents' sources were de-activated, and the modulator (input terminal) rotated step-wise through 360 electrical degrees while the inner rotor was fixed in one position. It can be clearly seen that the obtained waveform is sinusoidal and reaches the maximum/minimum points at $\pm 90°$. The magnitude ratio between the two curves is precisely 10.5, which corresponds to the speed gear ratio between the inner rotor and the modulator. In addition, the two curves

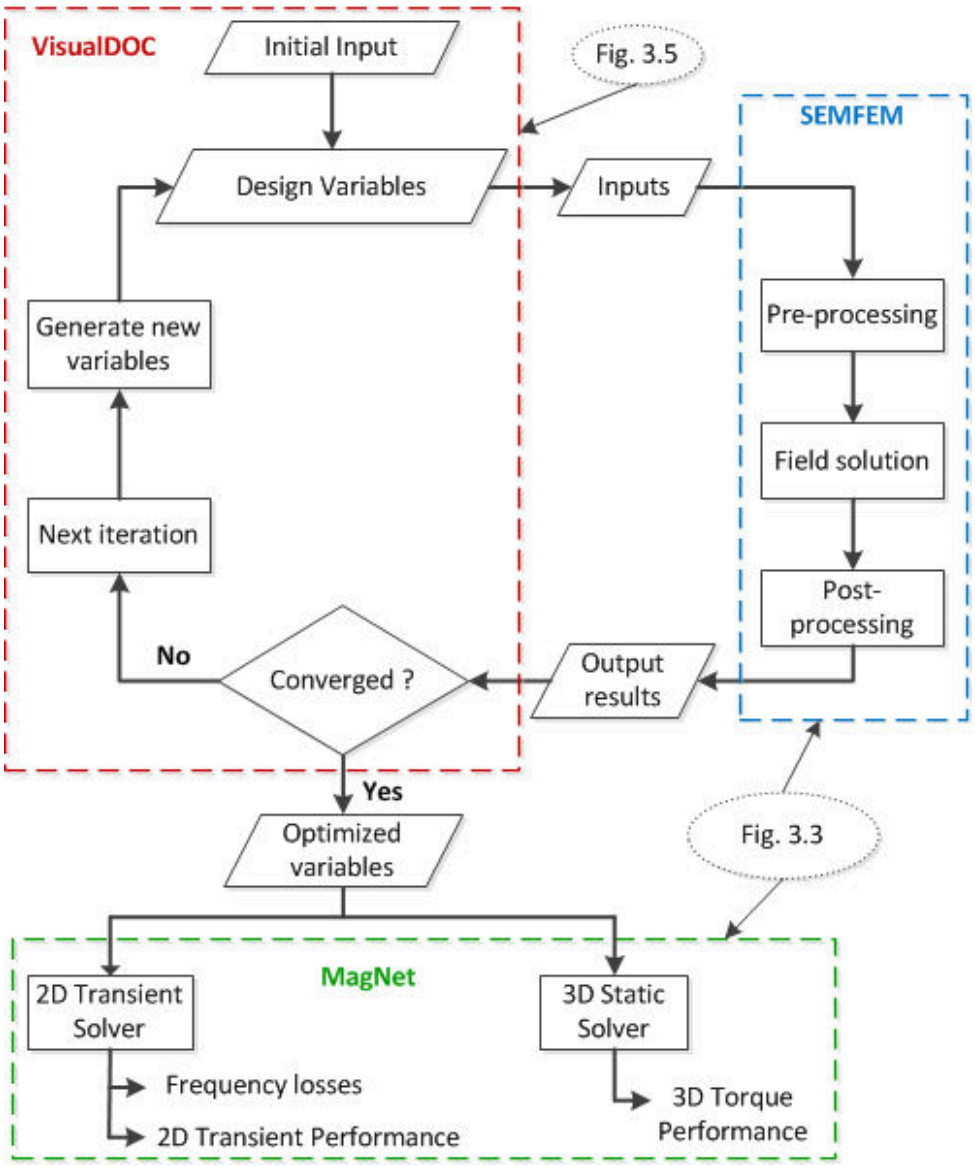

Figure 3.6: Optimization flow diagram.

intersect at 0° or ±180° where their magnitude is equal to zero, hence these are called the no-load or equilibrium points.

In practical operation, the torque in both components increases along the curves as the gear load is increased. But if the gear load is increased beyond the maximum static torque value in this graph, the gear will "slip over", causing the two components to disengage. This process is called overload protection, since the torque transmission is halted preventing any components from being physically damaged. After the modulator and the inner rotor decouple, the inner rotor runs at unstable speed or vibrates until the load is decreased to a value within the gear's capacity or the input rotor stops.

Figure 3.8 shows how the ratio of the machine's stack length to its outer diameter ($\xi = L/D$) affects the maximum torque capacity and torque density. Although all electrical machines have some end effects and should ideally be modelled by 3D FE programs, it is

Table 3.5: Optimized variables.

Parameter	Value	Units
Rotor magnet thickness (t_{mh})	6.50	mm
Fixed magnet thickness (t_{ms})	4.34	mm
Rotor magnet span to pole-pitch ratio (θ_s/θ_p)	0.92	–
Fixed magnet span to pole-pitch ratio (θ_s/θ_p)	0.84	–
Rotor yoke inner radius (r_y)	20.48	mm
Rotor yoke thickness (t_y)	11.71	mm
Modulator thickness (t_{md})	6.06	mm
Modulator bridge thickness (t_{brg})	0.5	mm
Inner modulator pole width ratio (θ_{mi}/θ_{mp})	0.50	–
Outer modulator pole width ratio (θ_{mo}/θ_{mp})	0.41	–
Stator tooth length (l_{st})	10.0	mm
Stator tooth thickness (t_{st})	7.27	mm
Stator tooth base thickness (t_{sb})	4.6	mm
Stator yoke thickness (t_{sy})	4.9	mm
Stator slot pole to pitch ratio (θ_{ss}/θ_{sp})	0.87	–
Stator slot filling factor (S_{ff})	0.55	–

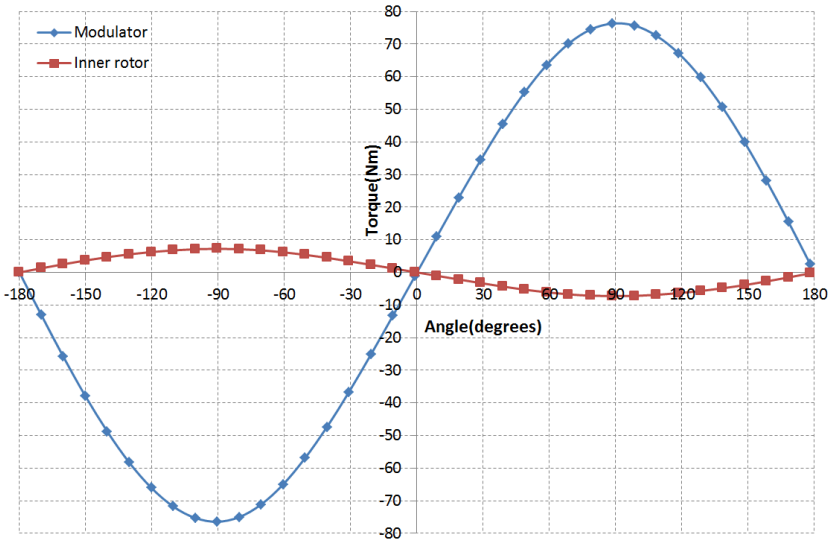

Figure 3.7: Torque angle curves (2D FEM).

a normal practice in research institutions and industries to employ 2-D analysis since 3-D FEM based programs are time expensive. However, the use of the 2D analysis methods (FEM or analytical) can lead to the over-estimation of the machine's performance as it is assumed that electrical length is equal to the physical stack length, and the end-effects are ignored. To determine the best ξ with regard to torque density, the machine was first optimized in 2D FE, then simulated in 3D FE with ξ varied from small fractions to 1, which means the machine has equal diameter and stack length at that point. To ensure the reliability of the results, ferro-magnetic material properties were modified to have a third dimensional field permeability.

It can be clearly seen from the graphs in Fig. 3.8 that the torque density increases rapidly with ξ to an optimum region before reaching to the state where there is little further increase. Considering the fact that long axial lengths may be subjected to component deflection due to strong PM alternating forces, and also incorporating the implications of the graphs in Fig 3.8, it may be preferable to have a stack length between 0.35 to 0.45. The current design is at 0.357.

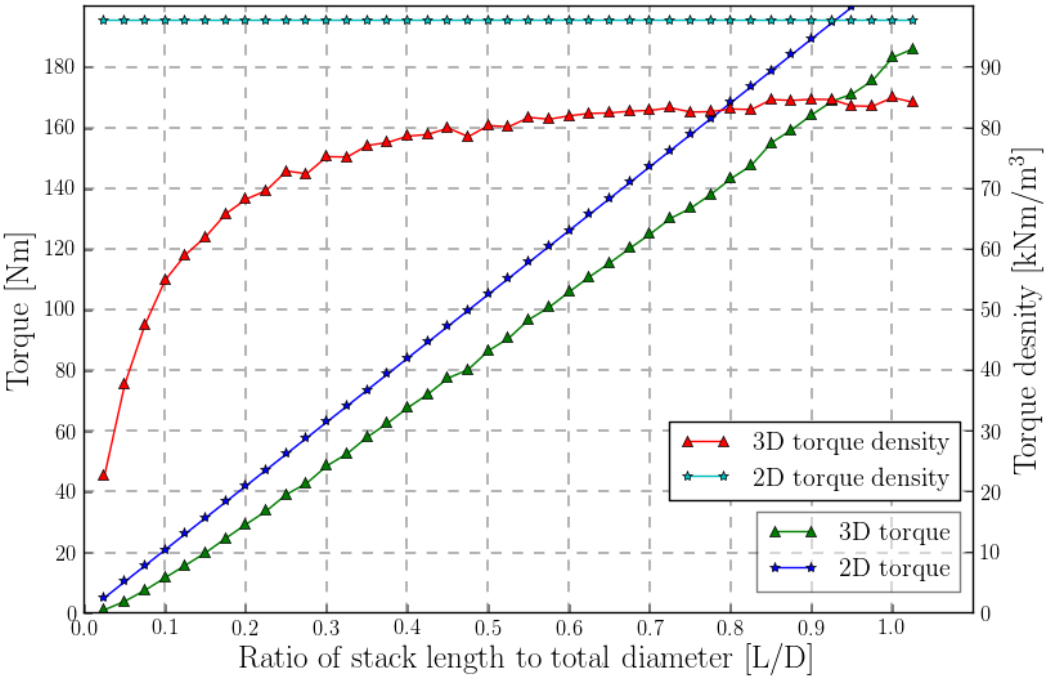

Figure 3.8: Torque density relationship to ratio of machine's stack length and total diameter.

The machine's total mass is one of the most important sales metrics to consider when the design is carried out. In most cases, it is not easy to predict the mass of the housing and support structure during the design or optimization stage. Therefore, only the masses of the electrically active components' are investigated in this chapter of the study. Moreover, the end-winding mass is automatically excluded although it forms part of the electrically active material, because the optimization was done based on 2D FEM. The relationship of the total active mass to permanent magnet mass is presented in Fig 3.9. This shows that a decrease in total mass results in using more PM material, while the opposite happens on the other design point. The PM material was paid special interest since it makes a significant contribution to the total cost of the machine, while the overall weight relates to the practical application of the machine. Thus, a trade off has to be reached between the two masses for an optimized design.

Tables 3.6 and 3.7 list the summarized results of the designed machine, which includes the losses, performance parameters and weights of different materials involved. The stator makes a major percentage contribution to the losses due to the copper losses, whereas the

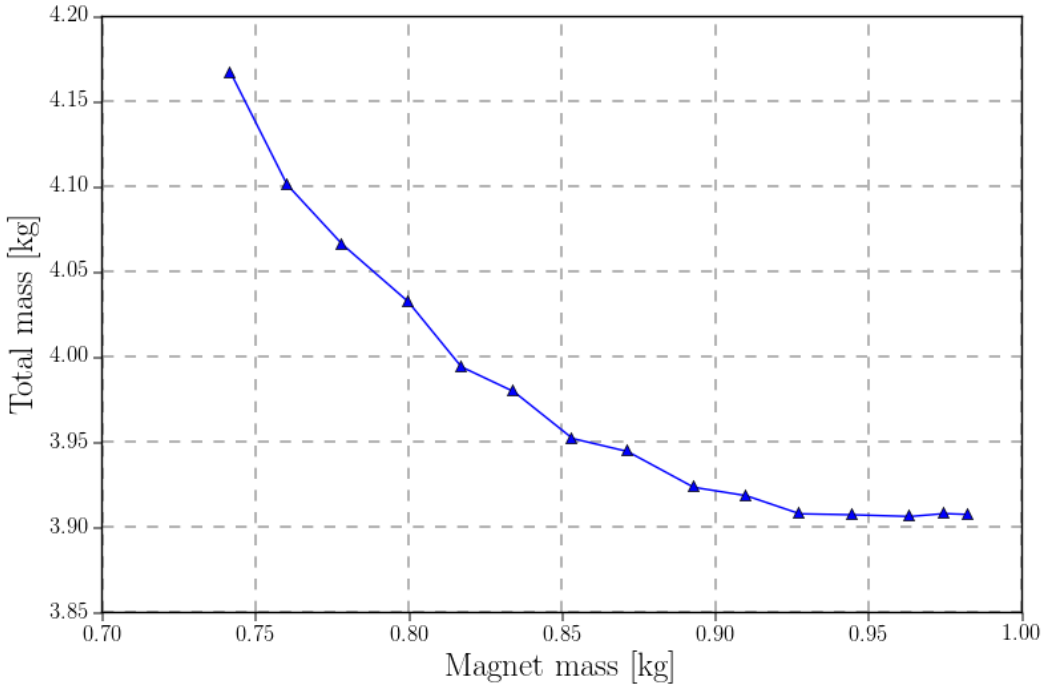

Figure 3.9: Total active masss versus permanent magnet mass.

frequency losses are insignificant because of low frequency. On the other hand, the cogging and ripple percentage torques are much larger on the inner rotor. This may have been expected since the cogging torque factor was also high, as there is lower number of pole-pairs on this rotor. Equally important, no other cogging torque minimization techniques were applied in this study as they constitute manufacturing problems and inaccuracies, except for adjusting the optimized PMs' pole-arc to the values with slightly less cogging torque. The torque density and torque per active mass are quite impressive, but it should be remembered that these might be overestimated since they are the 2D FE results and ignore housing volume and mass, hence they will be validated in the next chapter through 3D FE simulations and practical results.

Table 3.6: Loss composition in an outer stator MGPM machine.

Component	Copper loss [W]	Average Hysteresis loss [W]	Average Eddy current loss [W]	Total [W]	% Contribution
Inner rotor	0	0	10.35	10.35	13.71
Modulator	0	1.47	0.194	1.664	2.20
Fixed PMs	0	0	4.15	4.15	5.50
Stator	54.02	4.55	0.759	59.329	78.59
Total	54.02	6.02	15.453	75.493	–

Table 3.7: Performance results.

Component	Values
Maximum torque (gear), (Nm)	76
Average stator torque, (Nm)	7.33
Torque density, (Nm/m^3)	98.53
Torque per active mass, (Nm/kg)	19.03
Torque ripple (Inner rotor)	13.6%
Torque ripple (Modulator)	0.79%
Cogging torque (Inner rotor)	15.73%
Cogging torque (Modulator)	0.73%
Induced phase voltage (rms) (V)	137
Permanent magnet mass (M_{PM}), (kg)	0.834
Copper mass (M_{CU}), (kg)	0.951
Ferromagnetic material mass (M_{FE}), (kg)	2.209
Total mass (M_{Tot}), (kg)	3.994

3.3.4 Discussions

Air-gap magnetic flux density magnitude and harmonic content is a decisive parameter for torque transmission in an MGPM machine, as well as a determinant factor for its cogging torque and core loss characteristics. The magnetic flux density distributions under full- and no-load conditions of the machine are shown in Fig. 3.10, as obtained from the 2D FEA solution. It can be clearly seen that the majority of the flux lines couples the stator, modulator and rotor across the two air-gaps, which is a beneficial and required circumstance for torque production and gearing purposes. However, there are a few other flux lines that form return paths between two adjacent PMs and/or the modulator, not going through the second air-gap. These flux lines denotes the PM inter-leakage flux that negatively affects the machine's performance as it does not contribute to torque production and can induce additional core loss. Inter-leakage flux can occur directly between two PMs' edges or on a linked path from one PM to the modulator pole-piece, then back to an adjacent PM of opposite polarity, as indicated by "A" and "B" in both Figs. 3.10(a) and 3.10(b). Case "A" in Fig 3.10 relates more to the PMs' thicknesses. Besides, a too short gap length between consecutive PMs, which is the probable scenario when the number of PM pole-pairs is too high in a small circumference, results in increased leakage due to lower reluctance.

As shown in Fig 3.10, the MGPM machine consists of two layers of PMs. For those PMs exposed to opposite magnetic field, it is important to assess the risk of possible demagnetization. It was realized that during the optimization for maximum torque, the PMs on the stator tend to be thinner while the PMs on the rotor get thicker, which would increase the chances of demagnetization in the stator PMs when they face the rotor PMs of opposite polarity. This is the reason why a thickness ratio between the two PM layers is constrained in the design optimization. In addition, the PMs mounted on the stator

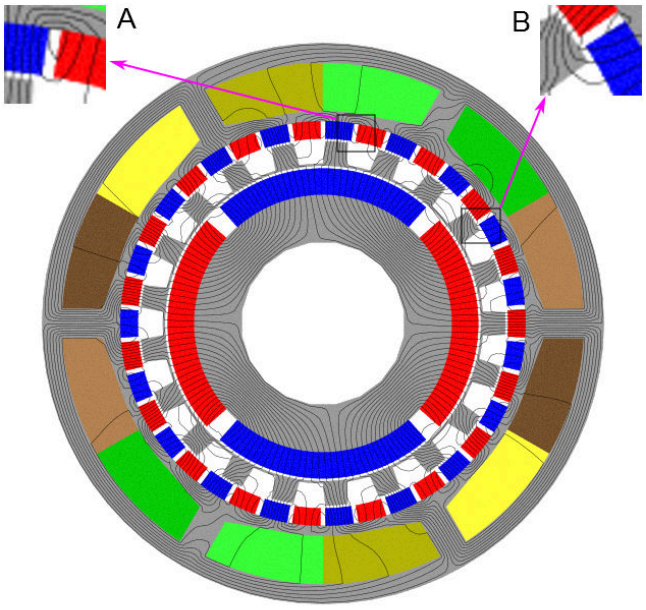

(a) No load

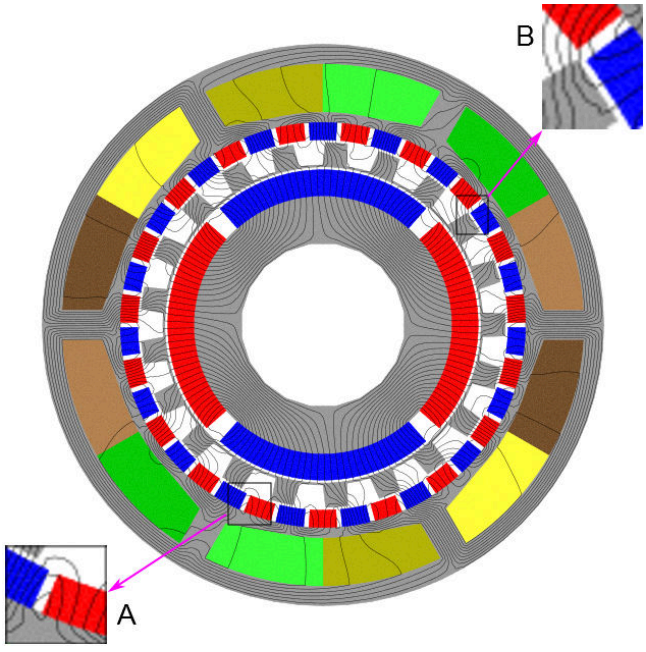

(b) Loaded

Figure 3.10: Magnetic flux distributions at full- and no-load conditions.

inner surface are also affected by both the armature reaction field and heating effects from the stator.

To assess the demagnetization effect as a consequence of these conditions, further analysis of the optimized MGPM machine within a range of temperatures at maximum current rating and load angle has been performed. The FE program (MagNet) used for this purpose indicates the degree of demagnetization in PM regions by two terms, i.e. *demagnetization proximity* and *prediction*. The demagnetization field proximity is calculated by

the following equation [77]:

$$\text{Demagnetization proximity} = B_{\text{demag}} - \mathbf{B} \times \frac{\mathbf{M}}{M} \tag{3.3.4}$$

where B_{demag} is the demagnetization thresh hold and $\mathbf{M}$ is magnetization vector. The demagnetization prediction is an indication of severity of demagnetization proximity on a scale of 0 to 1, corresponding to no risk and high risk of demagnetization, respectively.

For the analysis, the B_{demag} was set to 0.5 T since a PM is already on the verge of having totally reversed field if B can reach 0.0 T. This means that if the demagnetization proximity is above zero, the field of a PM (in its magnetization direction) has dropped below 0.5 T and the demagnetization prediction will also rise from zero to flag the risk of demagnetization, as illustrated in Fig. 3.11. In this figure, it can also be seen that the stator PMs are subjected to partial demagnetization beginning from the edges.

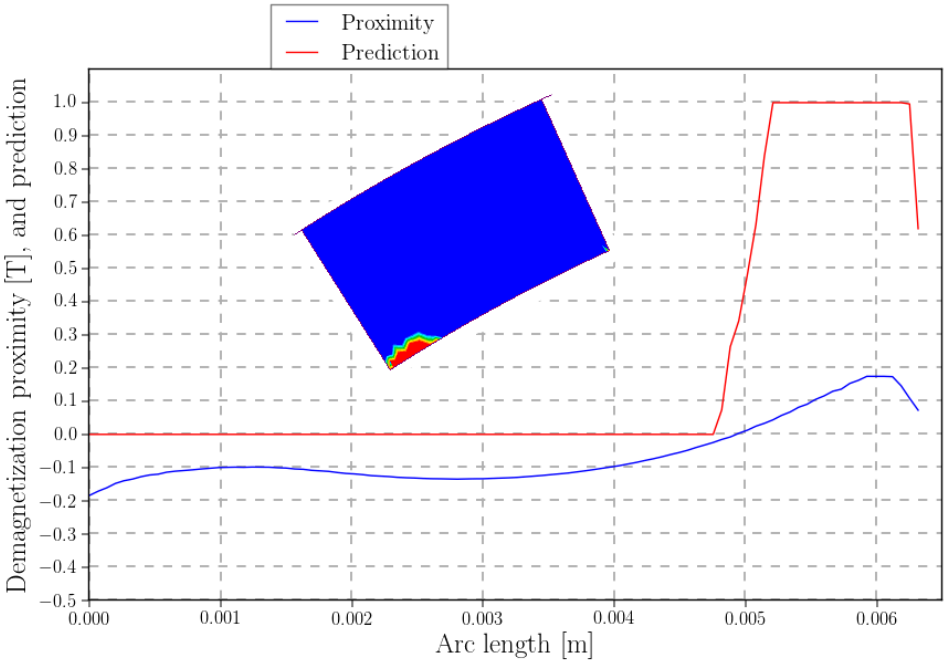

Figure 3.11: Demagnetization prediction on the surface of a stator PM, at 40°C.

Fig. 3.12 presents the plot of maximum and minimum proximity values on the surface of a single magnet, as a function of temperature. It can be read from this figure that the whole PM surface is exposing to demagnetized risk from the temperature of 60°C. Although this analysis is conducted for a single PM, all the PMs on the stator experience the same effect during operation. The relatively high demagnetization risk seems to be a major drawback of this outer-stator type MGPM machine. Since the design is based on N48H magnets, the operational temperature limit of the prototype machine has been set at 60°C.

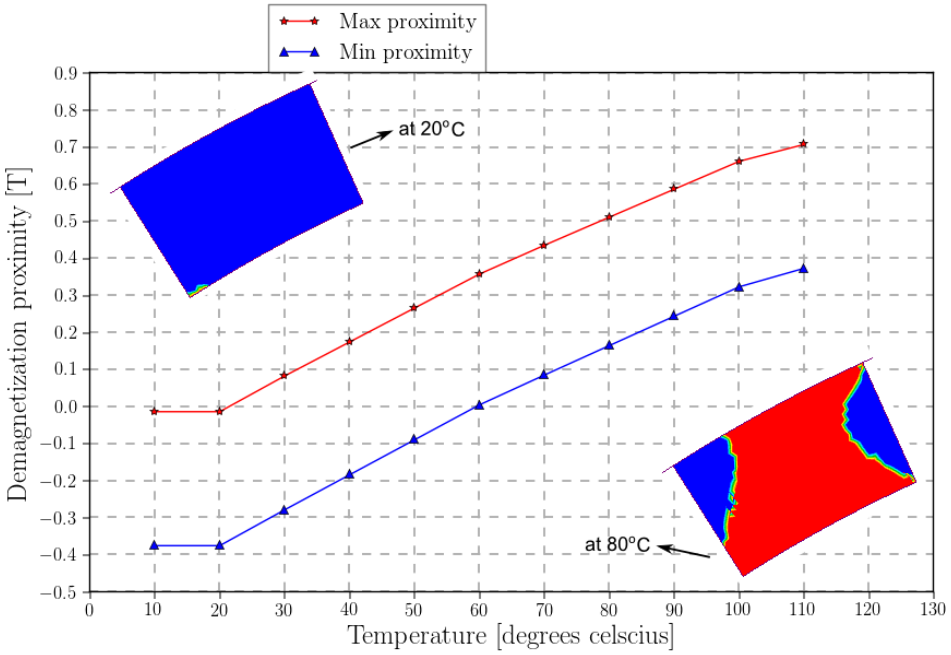

Figure 3.12: Demagnetization proximity as a function of temperature.

Chapter 4

Mechanical Design and Construction

It is important to note that during the machine optimization, the focus was mainly on the magnetically active components, excluding most of the support structure. This chapter explains how all of these units were integrated together to form a fully functional machine. The stator core and modulator pieces consist of an electrical steel laminations with a thickness of 0.5 mm, cut using the laser technology. The stator coils are hand wound with the aid of winding machine, and nomex paper was used to protect the copper coils against the sharp edges of stator core and to enhance the insulation between the two. The PMs are coated with a thin layer of black epoxy to protect them against corrosion.

4.1 Stator design

It has been mentioned in the previous design section that this project deals with the machine having slotted outer stator. Slotted stator is already at an advantage of better heat removal compared to the slot-less stator due to the large contact area, hence improved heat conduction between the stator core and the windings. Moreover, the outside stator has enhanced heat dissipation from the windings to the casing, then away to the surrounding environment, assuming the casing material is a good heat conductor. Because of the PMs that have to be stuck on the inner surface of the stator, as is the nature of this machine, the designer was confined to choose between the semi-closed and closed slots, while the open slots were not an option at all. These two possible slot options are shown in Fig. 4.1.

Semi-closed slots (Fig. 4.1a) have to be designed and constructed so that the opening between the teeth is enough for the coil wire to go through, while also providing more surface area for the PMs to rest on, so that they are not suspended on air. Having relatively thick teeth that can endure the strong magnetic forces to maintain uniform air-gap length as well as being PM flux return paths, means the coil space might be somewhat compromised for their thickness. In addition, inserting coil wires one-by-one

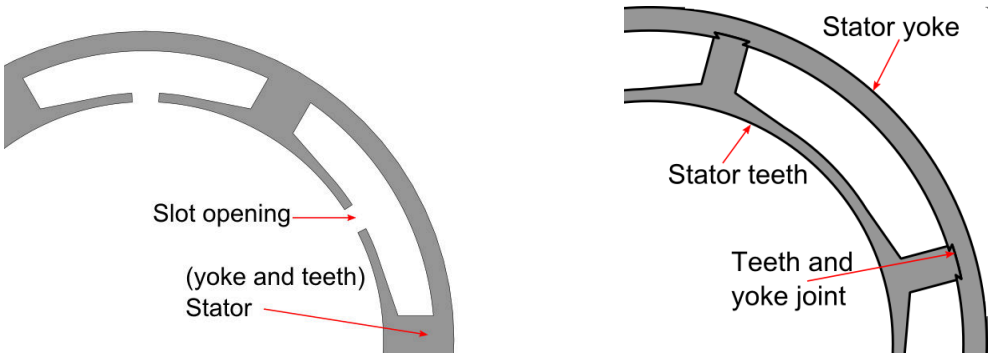

(a) Semi-closed slots (b) Closed slots

Figure 4.1: Stator slot design options.

through such a small opening may be quite an expensive process.

On the other hand, the closed slots stator has the teeth connected by the bridges on their inner radius. To enable the coil winding process, the teeth are fabricated as a separate component to the stator yoke and the two are joined together afterwards. One way to ensure secure joint without additional fixtures is to have teeth with dovetailed pins at the outside radius, and their corresponding grooves on the stator yoke, as illustrated in Fig. 4.1b. In this construction, the winding process might be easier and quicker than the previous design since the coils are wound from the wide open area between the teeth, or better than that, the preformed coils can be fitted onto the teeth from their outside radii. On the contrary, the tiny air-gaps between the teeth and stator at the joint area may be introduced due to manufacturing tolerances and imperfections. Consequently, additional reluctance is imposed on the flux path, which means a reduction in flux linkage and eventually reduced resultant electromotive force as well. This problem may be minimized by having a very tight fit joint, though assembly may also be challenging since both components are not solid but made of laminated material.

It was found that the optimized permanent magnet's pole-arc on the stator surface was very small that if the semi-closed stator had to be used, then some PMs will lay on the gap by a significant amount. For this prototype machine, it was decided to use the closed slots stator as shown in Fig. 4.2. The disadvantage of this design is that winding the coils is a tedious and complicated procedure, as one end of coil wire has to be "*pushed and pulled*" through the slots. This was possible to be done because the designed machine is small, handy and has few number of slots, but it is not a good practice for large machines or for commercial production.

Due to the difficulty in the winding process, a thick slot lining was applied. The achieved slot-filling factor of the prototype machine was only 0.359 which was less than the designed value (0.55). This would inevitably lead to a derated machine's output performance as

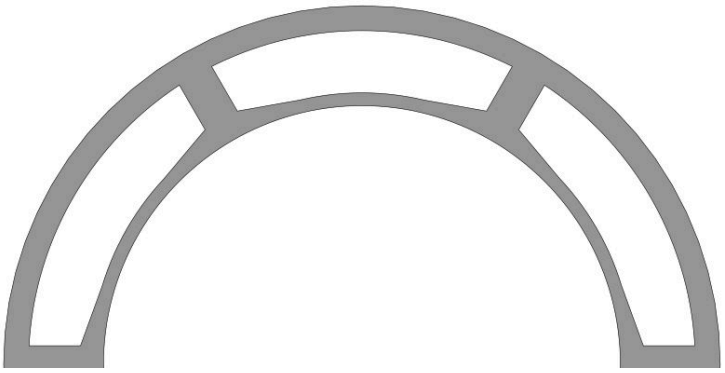

Figure 4.2: Closed-slots stator.

compared to the optimized results, especially in the voltage and electromagnetic torque.

4.2 Flux modulator

The flux modulating ring experiences the rotating fields with different harmonic magnitudes and frequencies. To minimize the frequency dependent iron losses in this component, it was made out of non-oriented silicon-steel laminations. Besides, the modulator is susceptible to strong magnetic forces resulting from both sets of PMs. Thus certain strategies had to be implemented to preserve its mechanical integrity even during overloaded conditions. Firstly, the fully assembled modulator is supported from both sides with the hubs to keep it concentric and perfectly aligned with the inner rotor axis while under the impact of continuously varying forces. The thin bridges connecting the modulator pole-pieces actually serves two major purposes, that is, they filter out some of unnecessary flux harmonics, thereby reducing torque ripples [52], while also holding the pole-pieces together at an equal angular distance from each other.

In order to keep the stack of laminations in intact shape, they are pressed by two end hubs and stainless-steel rods running in the slots of the laminations. It is important to note that even though these stainless steel rods are non-magnetic, they are good electrical conductors. Consequently, it is possible that a current can be induced in them under alternating magnetic flux conditions (similar to bar current in an induction rotor), especially if they are electrically connected on both sides. In other words, supporting the rods with electrical conductive material on both sides would turn the modulator into a squirrel cage rotor. Therefore, one supporting hub was made from a hard plastic material so that there is no current return path. To further strengthen the modulator, an epoxy resin was filled in the remaining air-spaces between the laminations and the rods. Figure 4.3 shows the model of the modulator with all supporting pieces in place. As depicted, the aluminum hub, laminations and rods are all united into one component by the epoxy resin.

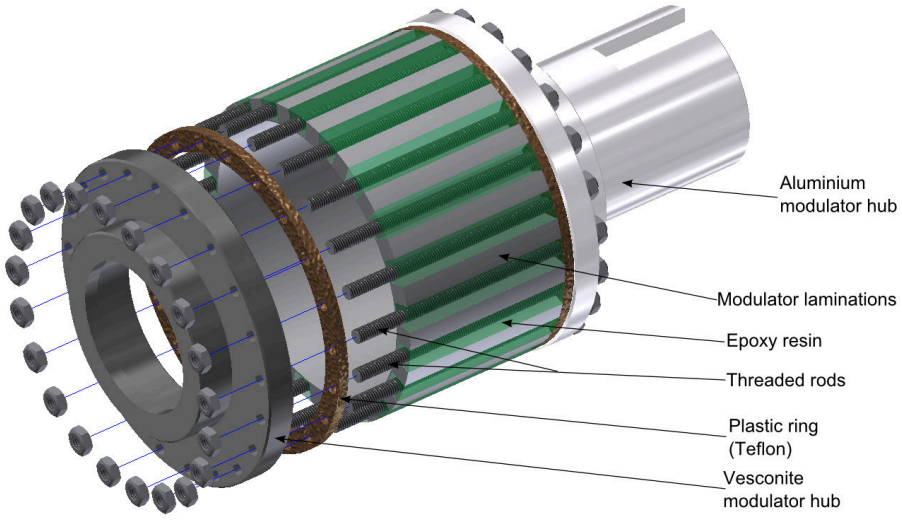

Figure 4.3: The modulator structure and its support components

The stack of modulator laminations and rods in preparation for moulding are shown in Fig. 4.4. An aluminum cylinder (mold) is fitted in the bore of the laminations to keep them concentrically aligned. The mold also has a key that slides through the laminations' key way to ensure that all the laminations' pole-pieces are perfectly aligned as well. Then the second modulator hub is put in, and tightly press fitted by the nuts to compress the laminations. A liquid epoxy is injected into the spaces between the modulator pole-pieces while a plastic is wrapped around it, and let for self hardening.

Due to a difficulty met in manufacturing thin bridges (0.5 mm) between the pole-pieces, the modulator was initially cut with thicker bridges at the production stage. Then it was machine down to size after the epoxy cures. The finished modulator is shown in Fig. 4.5.

4.3 Rotor design

It is assumed that the magnitude of the losses resulting from the time-varying flux density in the inner rotor yoke is acceptably low, thus this yoke is made up of mild steel to simplify manufacturing process. This allows the yoke and shaft to be configured as one solid component (Fig. 4.6). There are several ways applicable for mounting PMs on the yoke. These includes surface mounted, surface inserted and radially embedded (spoke type) techniques. In surface insert type, the PMs are embedded in shallow slots along the yoke circumference. Spoke type concept involves PMs radially embedded in the stator yoke, and this arrangement works by having the flux concentrated in the certain direction in the iron yokes between the PMs. Although they offer improved reliability of the rotor structure, both methods have a significant proportion of flux wasted through leakage into the iron core.

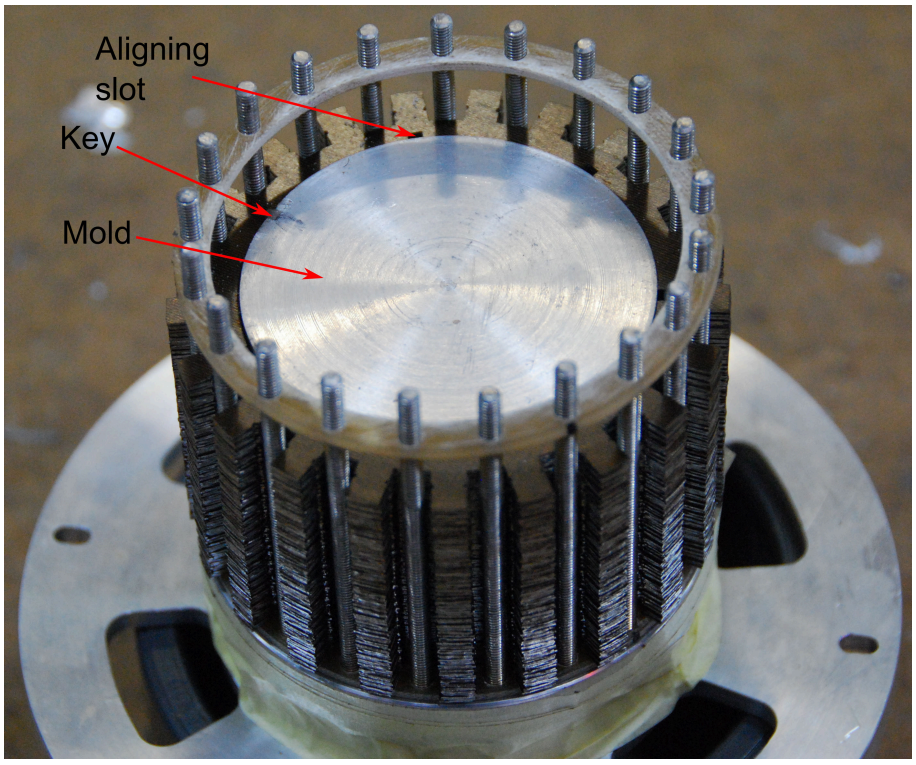

Figure 4.4: Preparation of the modulator laminations for moulding

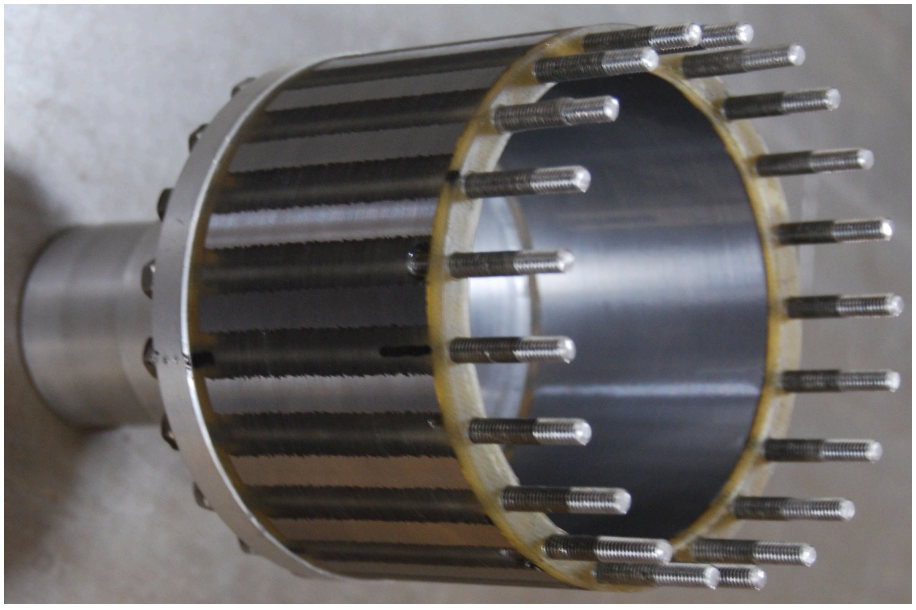

Figure 4.5: Final modulator structure.

In spite of the merits of the two methods discussed above, the preference was given to the surface mounted PMs due to several reasons. Surface mounted rotors are the easiest to construct, and best utilization of PM material is easily achieved in this method, hence high pull-out torque can be obtained. Furthermore, the low rated speed of the machine means reduced magnitudes of centrifugal forces and eddy current losses on the PMs. Neodymium iron boron ($Nd_2Fe_{14}B$) PMs with high thermal rating ($N48H$) are used as

the source of excitation, and they are glued on the rotor. Strips of non-magnetic material (Teflon) are inserted in the gaps between them, as illustrated in Fig. 4.6 to provide a support against tangential dragging force.

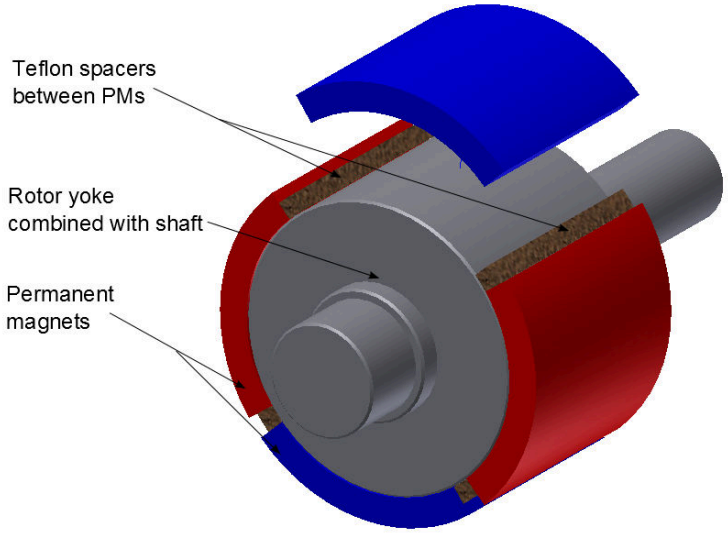

Figure 4.6: Inner rotor

These teflon strips are carefully cut to the precise angle desired according to the design, so that they aid to maintain uniform gaps during the mounting process, before the glue hardens. The completed rotor is shown in Fig. 4.7.

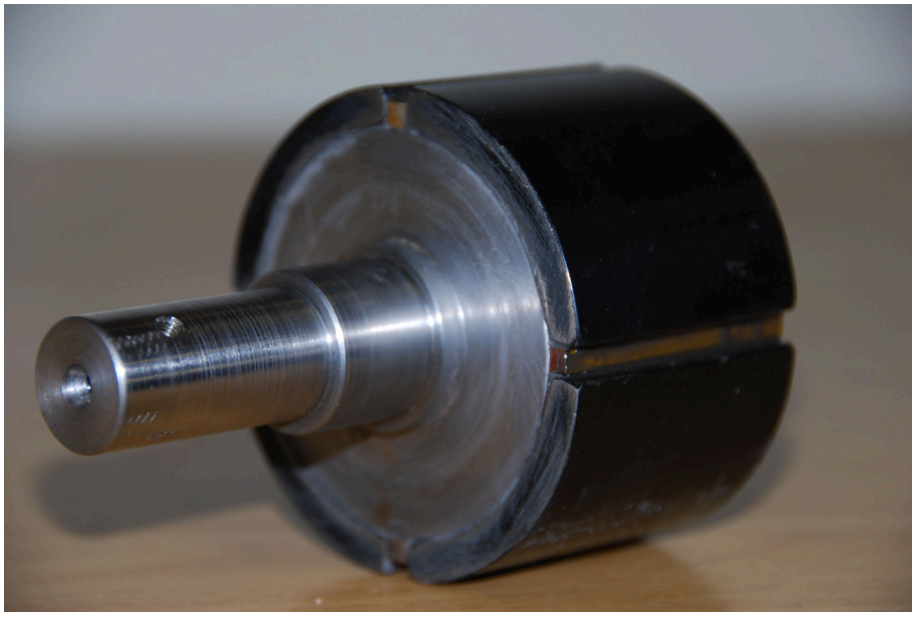

Figure 4.7: Completed inner rotor

4.4 Bearing selection

The rotational movement of the machine's components relative to each other is facilitated by the use of the bearings. Since the commercial bearings are available according to their own dimensional standards, careful selection was made to find those that can fit within the machine housing while also capable to handle the predicted loads. The space for the bearings was limited radially by the maximum allowable inside diameter of the supporting hubs for each component, and constrained axially by the fact that the machine was to be kept as compact as possible. With these considerations, single-row deep-groove ball bearings were found suitable for the current design. It would have been more beneficial if stainless steel bearings were used to reduce the effect of axial flux leakage, but because of their un-availability on the local suppliers, SKF bearings with normal magnetic materials were used. To compensate for this, teflon rings were placed between the support structure and the magnetically active components, such that a reasonable space is maintained to weaken the strength of leakage flux before it reach on them. Furthermore, sealed bearings were selected as they preserve their lubricants for longer time at the same time as rejecting contaminants from the outside surrounding.

To validate the ability of the selected bearings to support the components' loads at the rated speed, the equivalent bearings' loads, power loss and their life span were evaluated by implementing the formulae provided by SKF bearing manufacturers. The machine's components' masses and resultant forces which are to be supported by the bearings are obtained from MagNet 3D transient simulations. Then the equivalent dynamic bearing load is calculated from the following formula [80]:

$$Load_{bearing} = XF_r + YF_a \tag{4.4.1}$$

where F_r is actual radial bearing load, F_a is actual axial bearing load, X and Y are radial and axial load factors provided by the manufacturer.

From the 3D Magnet simulations and intuitive understanding of radial flux machines, the resultant axial force is insignificant, so only the radial forces are influential on the bearings loads. With the equivalent dynamic bearing load known, the frictional power loss is estimated from [81, 82]:

$$P_{bearing} = 1.05 \times 10^{-4} \times 0.5 \times \mu \times Load_{bearing} \times d \times n \tag{4.4.2}$$

where n is rotational speed in rpm, d is equal to bearing bore diameter in millimeters, μ is constant coefficient of friction for a specific bearing type, ($\mu = 0.0015$ for deep groove bearings).

The basic rating life of the ball bearing at 90% reliability is approximated by the following equation [83]:

$$L_{10h} = \frac{10^6}{60n} \times \left(\frac{C}{Load_{bearing}}\right)^3 \tag{4.4.3}$$

where C is basic dynamic load rating, also obtained from bearing manufacturer.

The main dimensions, rated speeds and loads of the used bearings are provided in the Table 4.1. In addition, their losses and expected life under normal working conditions and good lubrication are summarized in this table.

Table 4.1: Bearing parameters.

Parameters	6004-2RSH	(2x) 6005-2RSH	6009-2RS1
Bore diameter [mm]	20	25	45
Outer diameter [mm]	42	47	75
Axial length [mm]	12	12	16
Operating speed [rpm]	1575	1425	150
Equivalent dynamic load [kN]	995	1190	2210
Rated operating life [hours]	10582	11695	111111
Power loss [W]	2.468	3.339	1.174

4.5 Construction and assembly

The construction and assembly of the prototype machine was carried out in the university's machine's lab, while most of the components were produced from external company, with the manufacturing specifications provided by the designer. The stator housing and the two side end caps are made from aluminum for the two main reasons:

- Aluminum is lighter, so it doesn't add too much weight on the total machine mass.
- Since it is a good conductor of heat, it enables heat transfer from the stator core to the outside surrounding

Moreover, holes are excavated in the stator end caps without weakening their structure strength, to allow free aeration of air into the inner components, especially the coils and magnets for cooling purposes. The hollows are also advantageous in a sense that they reduce this component's mass by about 15% compared to the solid hub design, according to the mass properties extracted from Auto-Cad Inventor 2011.

In order to monitor the level of heat reaching to the PMs during the operation, the temperature sensor is embedded in the region between the coils and part of the stator holding the PMs (region A in Fig. 4.8).

While it may be argued that the temperature sensor will read an over estimated value of the heat on the PMs as it is also attached to the coils, the difference may be insignificant since there is thin iron material between the coils and PMs. It is predicted that more heat will be generated on the stator than on the inner rotor, for this reason, keeping the

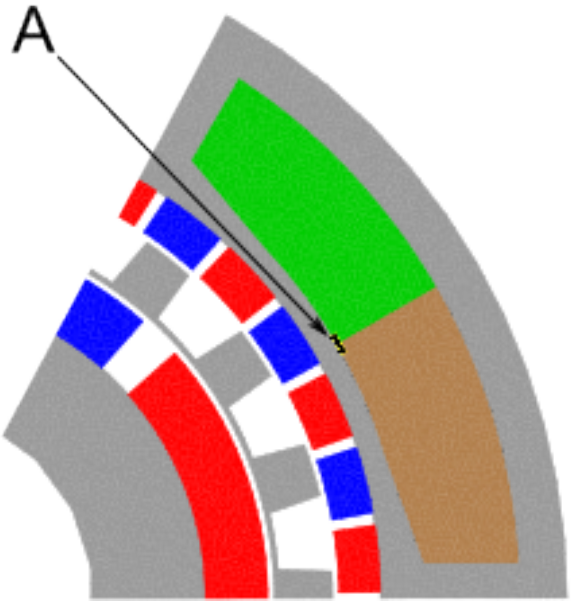

Figure 4.8: Location of temperature sensor on the stator

stator PMs under favorable temperatures also guarantees that the PMs on the rotor are well within their normal working conditions.

Figure 4.9 shows model of the stator core laminations fixed inside the housing, and compressed by the nut and rods combination to form one stack. The iron stacking factor achieved with this clamping method is 97%.

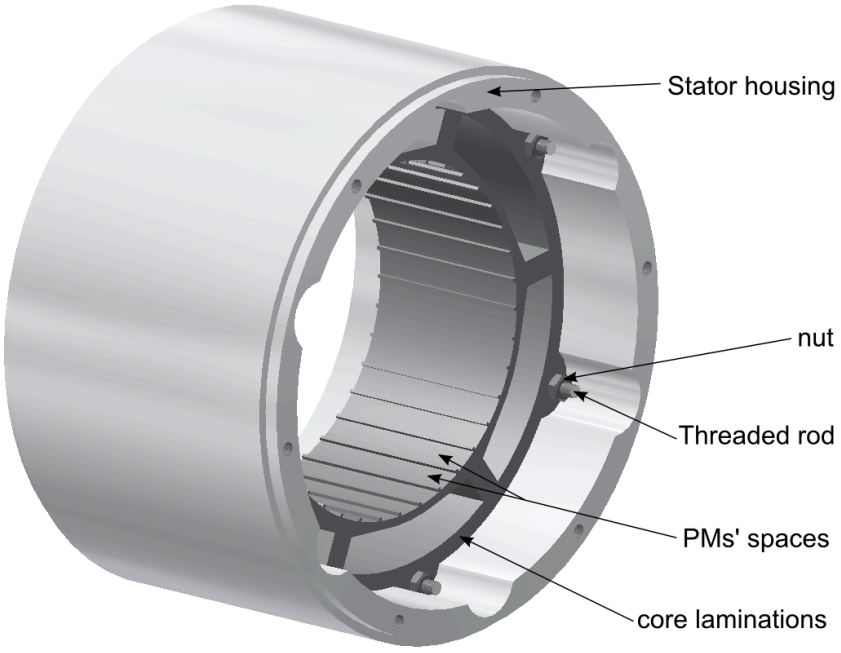

Figure 4.9: Stator core clamped by the rods inside the housing

The inner surface of the stator has tiny pieces sticking out in the region between the PMs' area. These protruding pieces helps to define uniformly distributed spaces for the

PMs along the circumference, and also provides an anchor for the PMs against the dragging force. To avoid any risk that the PMs would stand during the hand winding process, such as coat scratching or hitting onto other magnetic materials, the coils are first wound, then PMs glued afterwards. For the simplification of the winding process, each coil is independently wound, and subsequently connected in series with the respective coils to realize a required winding pattern. A *megohmmeter* test was used to ensure that the electrical insulation between the coils and the stator core is still maintained.

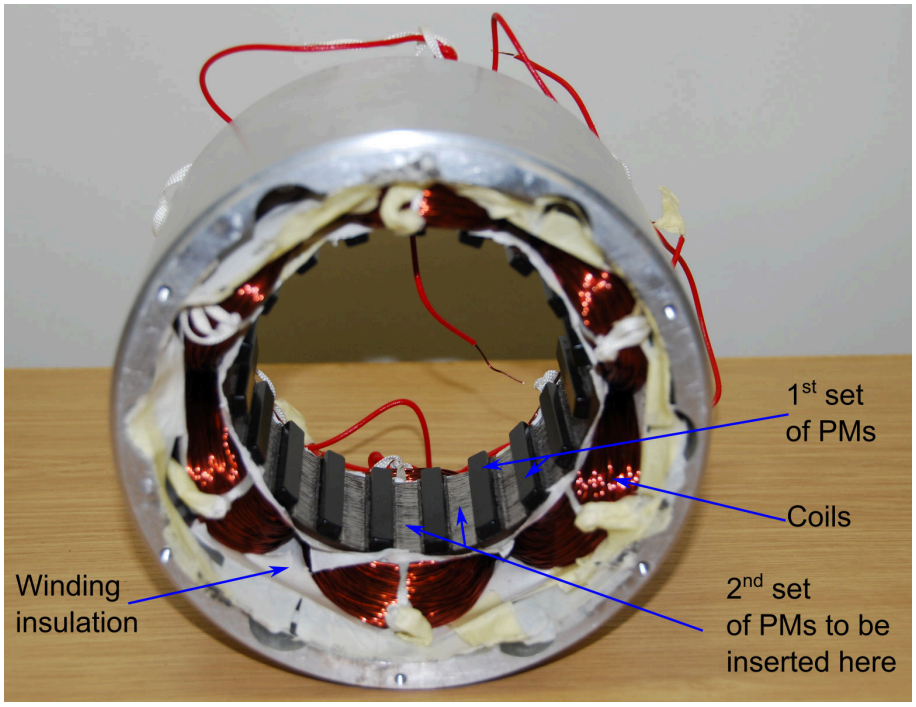

Figure 4.10: Placing the PMs on the stator bore

The stator assembly with first set of PMs glued on its bore surface, and with all PMs placed, is shown in Figs. 4.10 and 4.11. The longitudinal section of the complete machine is shown in Fig. 4.12. A photo of the assembled MGPM machine and its exploded view are given in Fig. 4.13. A summary of all the components' materials and properties used in this machine is presented in Table 4.2. Lastly, technical drawings with detailed dimensions and any other relevant information such as each components' materials are included in the Appendix A.

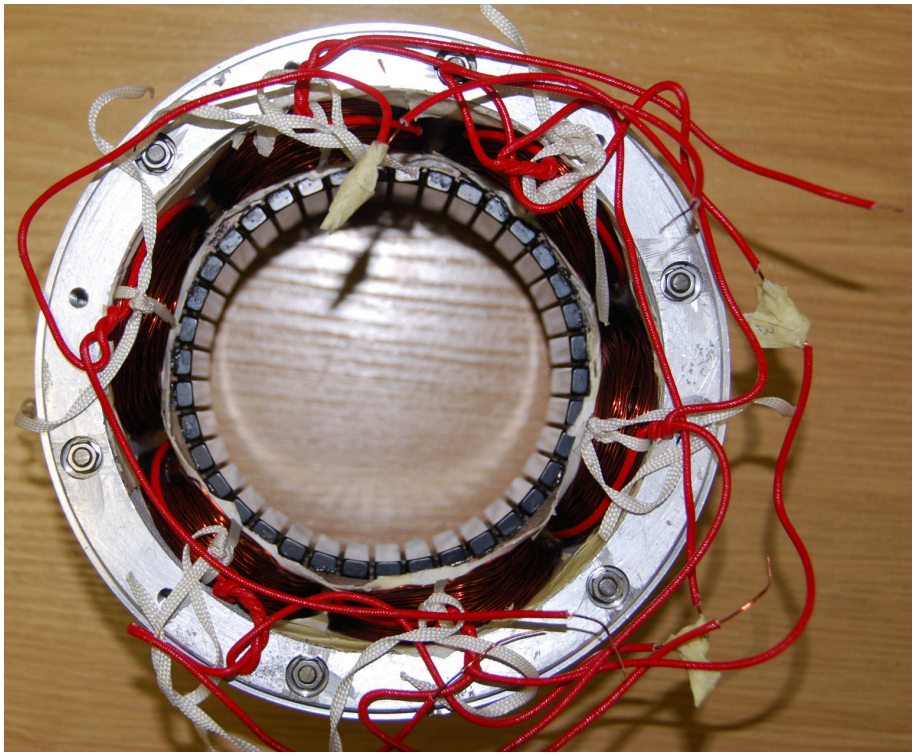

Figure 4.11: Complete stator

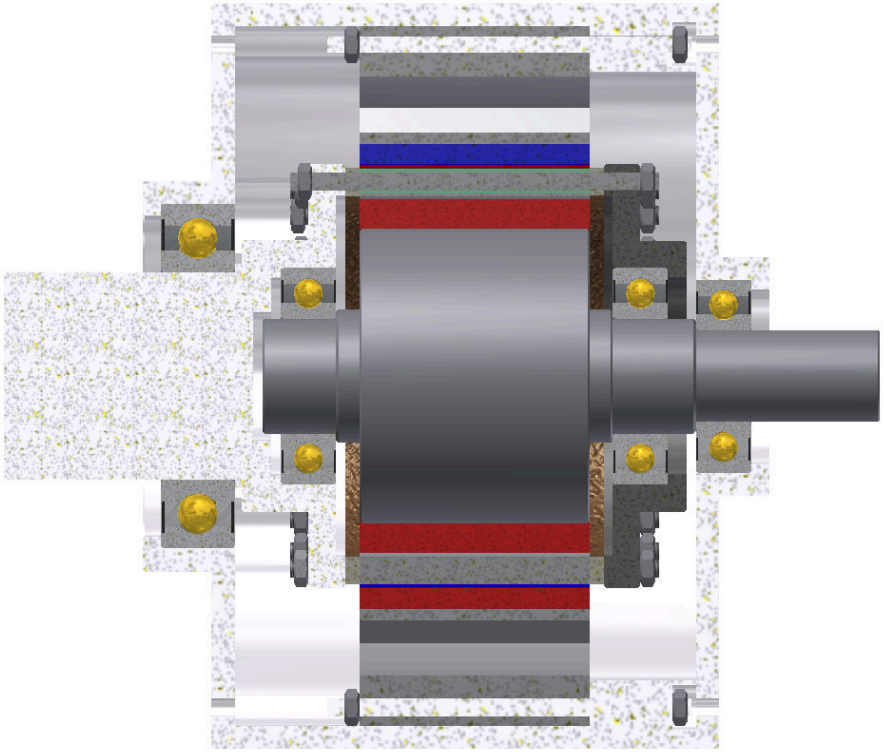

Figure 4.12: Full machine longitudinal section

Table 4.2: Component material and properties.

Component	Material	Properties
Stator core	$M400-50$	0.5 mm thickness, non-oriented silicon steel laminations
Stator housing	Aluminum 6082	Strong and high thermal conductivity
Stator hubs	Aluminum 6082	Strong and high thermal conductivity
Stator windings	Copper	Round wire, 0.65 mm diameter, high electrical conductivity
Winding insulation	Class F	Withstand high temperatures
Permanent magnets	$Nd_2Fe_{14}B$	High thermal rating, $B_r = 13.739\,\text{kGs}$, $(BH)_{max} = 46.263\,\text{MGO}$
Modulator laminations	$M400-50$	0.5 mm thickness, non-oriented silicon steel laminations
Modulator input hub	Aluminum 6082	Strong, high thermal conductivity
Modulator supporting hub	Vesconite	less thermal conductivity, non-magnetic, dimensional stability, light weight
Stator and modulator rods	Stainless-steel	Strong and very low magnetic conductance
Rotor yoke and shaft	Mild-steel	Strong
Modulator and rotor PMs spacers	Teflon	Strong and dimensional stability
Epoxy resin	Ampreg	Strong and self hardening (Good cure progression from ambient only cures)
Glue	Araldite-AV 138 and Hardener-HV 998	high shear strength, less thermal conductivity
Temperature sensor	Thermocouples	K type, large temperature range

Figure 4.13: The fully assembled MGPM machine and its exploded view

Chapter 5

Experimental Evaluation

The performance evaluation of the outer stator magnetically geared PM prototype machine based on its practical measurements is presented in this chapter. First there is a description of the test-bench employed to conduct all the experiments in the university's machines laboratory. Then the practical results from both the no-load and loaded test conditions are provided to compare with and validate the simulated results.

5.1 Test bench set-up

The set-up arrangement used for the prototype testing is made up of the following pieces of equipment:

- Delta AC servo motor
- Bonfiglioli LC series gear
- Flexible propshafts
- Torque sensor - Lorenz DR3000
- Three phase resistor bank
- Tektronix TDS 3014C phosphorous digital oscilloscope
- Voltage probes - Tektronix P5205 differential probe
- Current sensor - Tektronix TCP 202
- Agilent 34970A data logger, together with thermocouplers
- Computer, voltmeters, ammeters, three phase switch, connecting cables and three phase single coil transformer (variac)

The servo motor coupled with a gear and the prototype machine to be tested are connected by the prop-shafts via a torque sensor between them. The servo motor drives the machine at a required speed while the torque sensor measures the input speed, torque and mechanical power to the prototype. The output of the generator under the test is fed into a load resistor bank through a variac which is used to vary the output voltage and current seen by the load. Both the voltage probes and current sensors measure the continuous output voltage and current data, and logs them into the digital oscilloscope for waveform viewing and post testing analysis. During the operation, the machine's temperature is collected by the thermocouplers into an agilent data logger so that it can be easily monitored. The test-bench with the prototype machine mounted is shown in Fig. 5.1, and its schematic drawing depicted in Fig. 5.2.

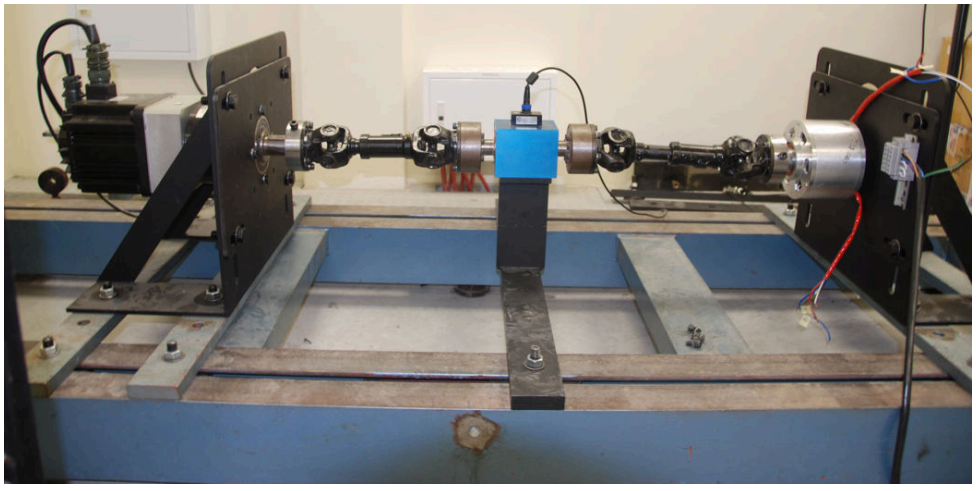

Figure 5.1: Test bench set up with prototype machine mounted.

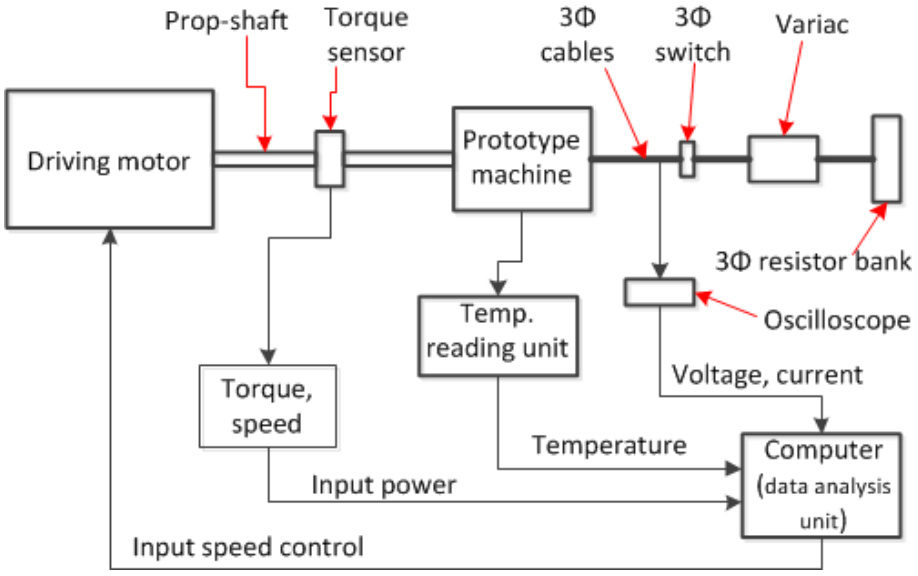

Figure 5.2: Schematic drawing of the complete test bench set up

5.2 DC phase resistance

In order to find a practical value of the stator resistance, and check whether the three coils are balanced, a simple circuit illustrated in Fig. 5.3 was constructed. By using this circuit, a number of mearsurements for the DC voltage over, and DC current through each of three stator coils was noted. Then the resistance was calculated from Ohm's law, which basically gives resistance as the ratio of voltage to current. Although the machine is meant for AC operation, DC circuit was employed for this purpose to avoid the inductance effect. It is known that resistance is temperature dependent, and a temperature coefficient of resistance was used in case it was necessary to calculate the resistance at any temperature of interest, but the presented measurements were recorded within a temperature range of 2 °C ($T = 25\,°\text{C}$ to $26\,°\text{C}$).

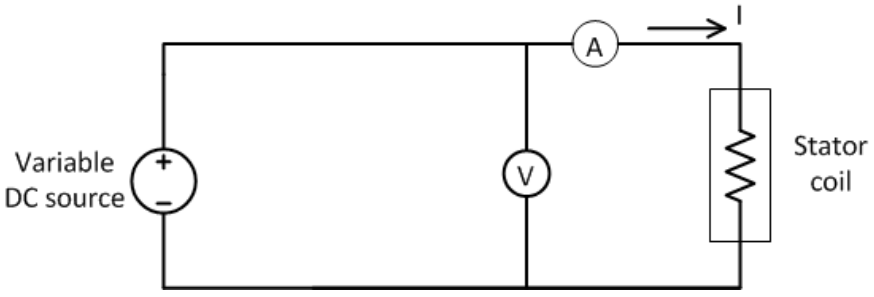

Figure 5.3: Measurement of stator coil DC resistance.

The measured voltage and current values and their corresponding resistance values are shown in Table 5.1. It can be seen that the average resistance of the three-phase coils is almost equal at an accuracy of one decimal point, with a slight difference, therefore it can be concluded that they are balanced with a stator resistance of $7.3\,\Omega$.

Table 5.1: Winding DC resistance data.

Coil 1			Coil 2			Coil 3		
I	V	$R = \frac{V}{I}$	I	V	$R = \frac{V}{I}$	I	V	$R = \frac{V}{I}$
0.51	3.70	7.25	0.50	3.70	7.40	0.50	3.70	7.4
1.00	7.30	7.30	1.00	7.30	7.30	1.00	7.20	7.20
1.50	10.90	7.27	1.50	10.90	7.27	1.50	10.9	7.27
2.00	14.70	7.35	2.00	14.60	7.30	2.00	14.80	7.4
2.50	18.50	7.4	2.50	18.50	7.40	2.50	19.00	7.60
Ave. R(Ω)		7.314			7.334			7.374

5.3 No load characteristics

The open circuit characteristics of the machine are experimentally determined by running the machine as a generator with no load connected at its output terminals. From this test, the back electromotive force (EMF) induced on the stator coils and no load losses which mostly include frictional and frequency dependent core loss, can be found. The three phase no load output voltage measurements obtained at a rated speed of 150 rpm is shown in Fig. 5.4. All three voltages are balanced, and placed 120° from each other. In addition, the voltage waveform shows a large magnitude of ripples which is thought to be a result of cogging torque between inner rotor PMs and stator teeth that tends to affect EMF harmonics as well. The maximum amplitude of these experimental voltage values

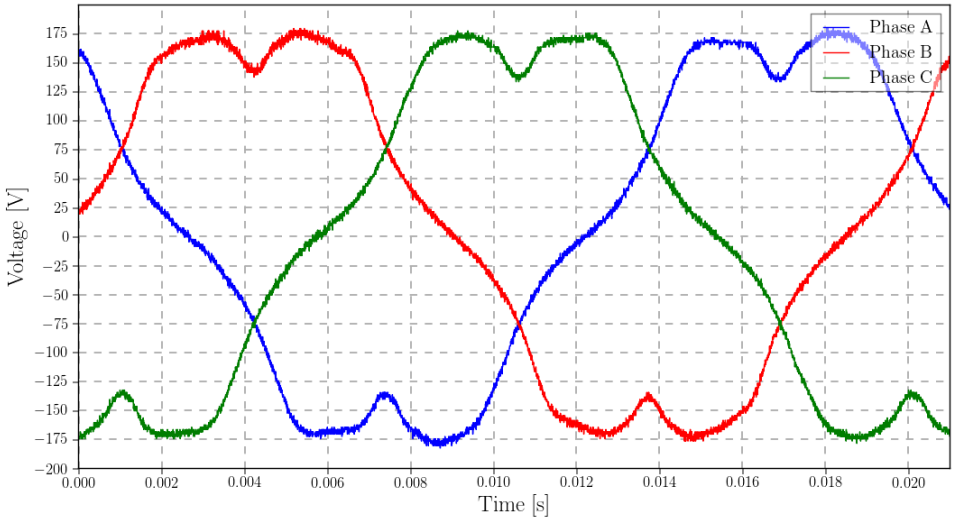

Figure 5.4: Open circuit voltage waveforms at 150 rpm.

are lower (by about 7%) than that of the 2D FE simulated transient results from MagNet. This percentage difference is still acceptable considering the fact that 2D FEM simulation ignore the leakage flux and some practical factors which may affect voltage production such as stator iron packing factor are not included. In addition, the FEM simulation assumes that the flux density is uniform across each and every coil turn, which may not be true. Apart from the discrepancies in induced voltage magnitudes, the measured waveforms closely resemble the simulated waveforms shown in Fig. 5.5.

Furthermore, the output electrical frequency computed as the inverse of total time for one complete waveform from Fig. 5.4, is obtained as 52.5 Hz. This is in good agreement with the theoretical calculations in section 3.1 which give the same frequency at an input speed of 150 rpm. Therefore, the speed gearing ratio of the machine can be validated by calculation of inner rotor's mechanical speed from voltage frequency, and then comparing

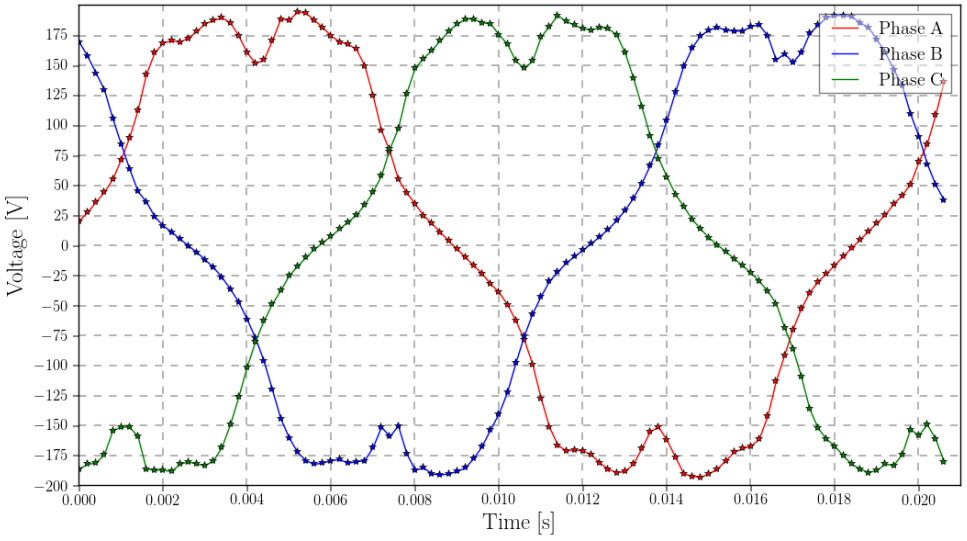

Figure 5.5: Open circuit voltage waveforms at 150 rpm from the 2D FE simulations.

its ratio to the speed on the input terminal(modulator) as follows:

$$n_h = \frac{60 \times f_{e\_out}}{p_h} = \frac{60 \times 52.5}{2} = 1575\text{rpm}$$

And the gear ratio

$$G_r = \frac{n_h}{n_l} = \frac{1575}{150} = 10.5$$

Again, this steady state speed ratio is similar to the designed value.

The no load back EMF measurements were also carried out at various speeds to indicate the relationship of machine's voltage induction to its speed. Figure 5.6 shows a graph of experimental and simulated back EMF rms values as a function of speed. As expected, the machine's voltage is linearly dependent on speed, and the simulated results are slightly higher than the practical due to the reasons already mentioned above.

The machine's no load power losses and their associated driving torque at the different rotational speeds were also investigated, and plotted in Fig. 5.7. These no-load power loss includes eddy current and hysteresis losses in both the ferromagnetic components and the PMs, and the mechanical losses such as bearing friction and rotor windage losses. It can be seen from the graphs on the figure that the total losses are alarmingly high compared to the combination of the analytically calculated bearing loss and simulated iron loss. It is understood that the discrepancy would still exist because the supporting structure were not included in the 2D FEM analysis, but that much difference was not expected. Since the non-magnetic supporting structural material (aluminum) was used to minimize the effect of frequency dependent loss resulting from the axial leakage flux density, it is suspected that frictional losses from the bearings have contributed to the total losses. The most likely reason for the unexpected high bearings' loss is that they are pre-loaded

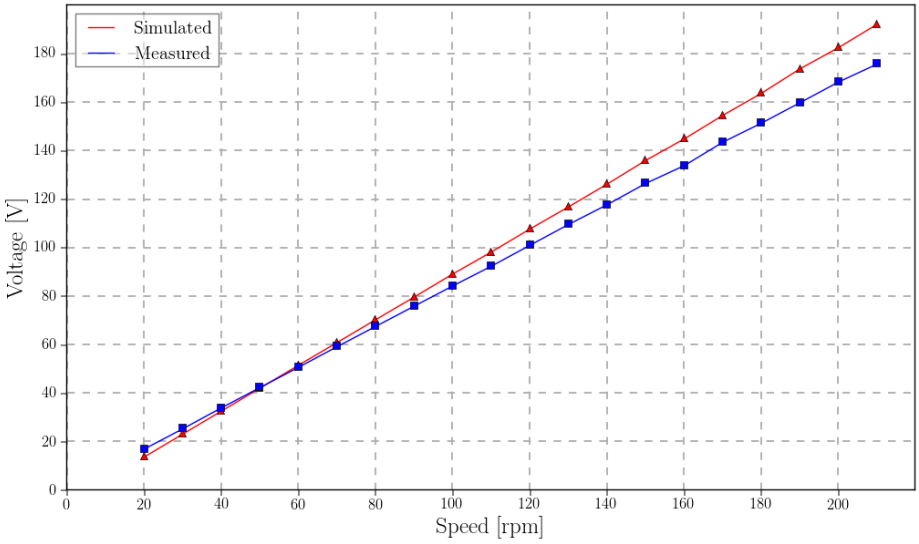

Figure 5.6: Phase rms voltage as function of speed.

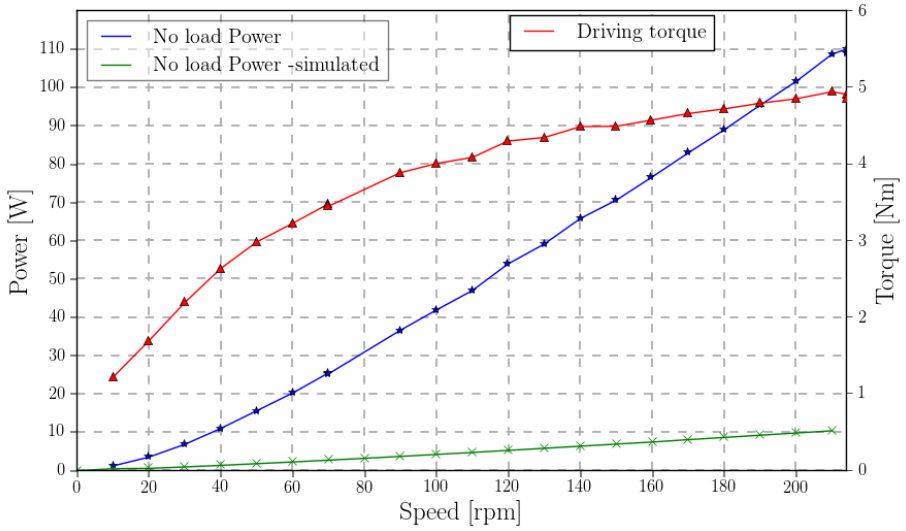

Figure 5.7: No-load power loss and driving torque.

in the axial direction. This was verified by slightly releasing the fastening nuts on the modulator and stator side hubs to give the bearings more axial space. The result was a reduced total loss of almost 40%, although this can't be seen as an absolute fix to the problem because the losses are still high and the machine cannot be expected to operate for a long time with the arbitrarily loosened components. Owing to this, the shaft will have to be redesigned to provide precise bearing space, so that the resultant losses can be minimized.

The maximum static pull-out torque of the magnetic gear part of the machine which basically represents the gear's torque capability, was measured through the set up shown in Fig. 5.8. The inner rotor is held at stand-still by clamping it, while the modulator input terminal is connected to the horizontal beam via the torque sensor. Then the

modulator is rotated step-by-step until the gear is overloaded and slips as it gets into the unstable torque region. For better understanding of how the set-up works, a simple

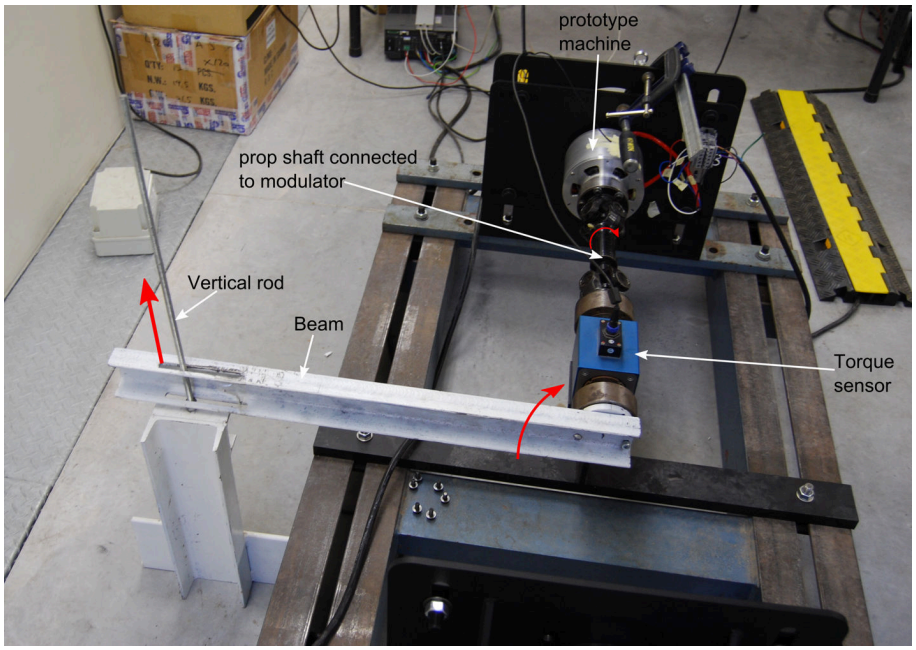

Figure 5.8: Locked rotor test set up.

schematic representation in Fig. 5.9 is included to help on the illustration, and further explanations can be found in [84]. Initially, the inner rotor and the modulator are adjusted to an angular position in which the torque between them is zero when the beam is in the horizontal position. By moving one end of the beam up the vertical threaded rod at almost uniform time steps, the gear is loaded since the modulator will be rotated at an angle relative to the locked inner rotor. As the beam is moved up, the torque is noted at each step and the tolerable maximum torque is reached when the rotated angle is 90 electrical degrees. The obtained experimental results are presented in Fig. 5.10a, while

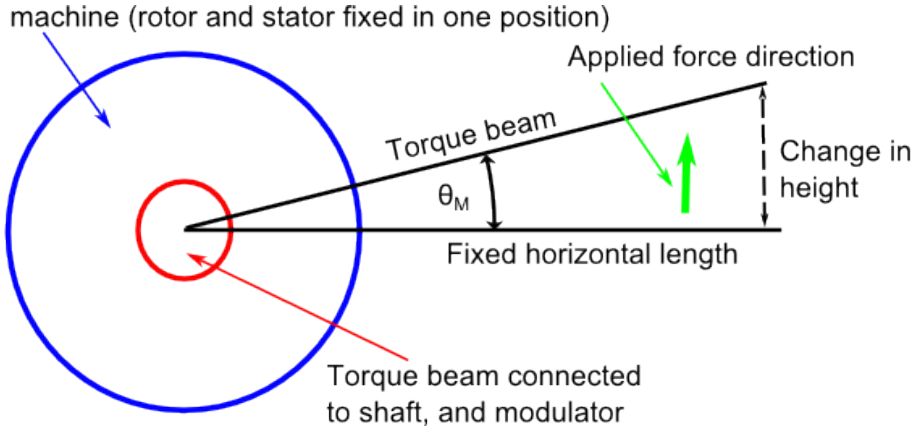

Figure 5.9: Illustration of locked rotor test set up [84].

the 3D FEM simulated torque angle curve is presented in Fig. 5.10b. To achieve the

simulated torque characteristics, a FEM model was repeatedly solved at small angle steps over one pole-pair, which is equivalent to 180 electrical degrees.

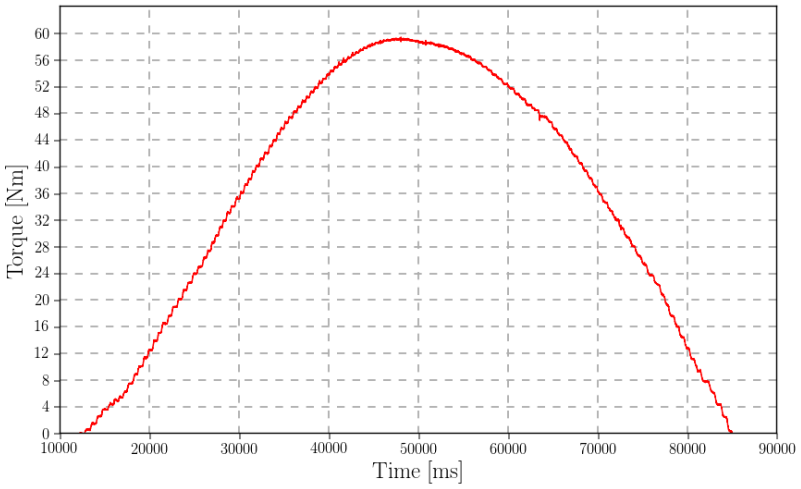

(a) Measured

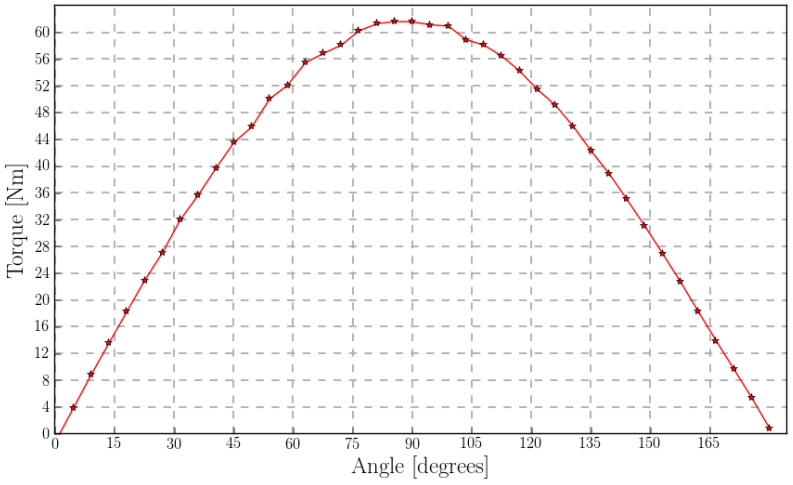

(b) Simulated

Figure 5.10: Static stall torque.

It can be deduced from both figures that the two curves compare favourably with the maximum simulated and experimental torques equal to 61 Nm and 59 Nm respectively, which comes to less than 4% difference in comparison.

5.4 Load tests

The loaded tests were performed to determine the output terminal voltage, torque and efficiency of the prototype machine at different operating speeds. The testing load used was a three-phase resistive load of 6 Ω, wye-connected like the stator windings. The measured three-phase currents' waveforms at a rated speed of 150 rpm are shown in Fig. 5.11.

In the same way as the generated voltage, the currents are also balanced, although they don't resemble a purely sinusoidal waveform as may be preferred. At a constant input

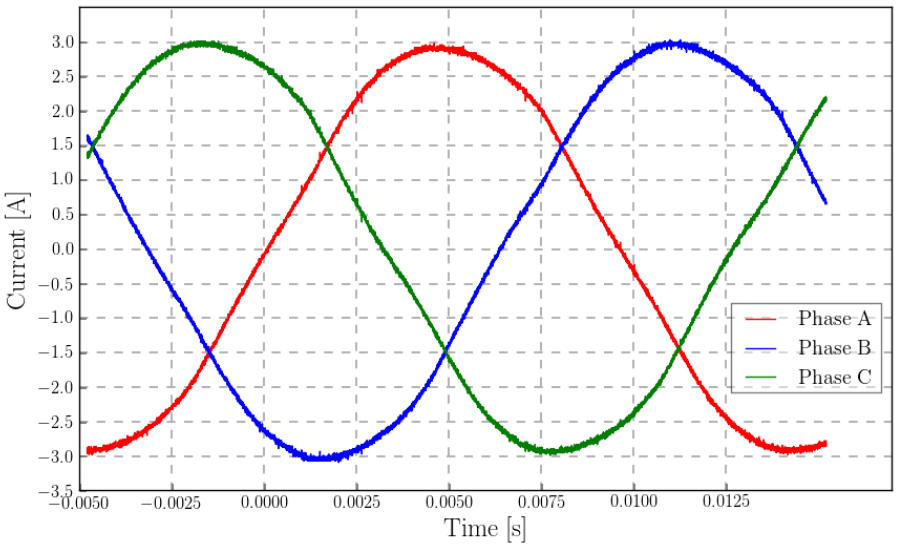

Figure 5.11: Measured three phase currents.

speed, the voltage drop across the stator winding resistance is proportional to the stator or load current increase, hence terminal voltage also decreases in accordance. The percentage difference between the induced input no load voltage and full load terminal voltage or terminal voltage at rated current, is conventionally termed voltage regulation. Percentage voltage regulation ($VR_{\%}$) is defined by eqn. 5.4.1 as follows:

$$VR_{\%} = \frac{V_{nl} - V_{fl}}{V_{fl}} \times 100\% \tag{5.4.1}$$

where V_{fl} and V_{nl} represents full-load and no-load terminal voltages respectively.

Figure 5.12 shows the terminal voltage variation as a function of stator/load currents at 50 rpm, 100 rpm, 150 rpm and 200 rpm. The poor voltage regulation in this machine is mainly due to the large impedance of the stator.

To determine the efficiency of the machine, the mechanical input and electrical output powers are measured at various operating speeds. The output apparent power is computed from measured output voltage and current, and the power factor is taken into account to separate reactive and real power. Both input and output powers at rated current are plotted in Fig. 5.13 as a function of speed. Also shown in the figure is the accompanying efficiency at rated current. Because the power graph is plotted at constant current (rated), the copper losses are also fixed, hence the efficiency has an increasing trend with increase in speed. The slope of an efficiency graph is initially steeper but flattens at higher speeds due to the overwhelming friction and core losses. Since the machine's operating efficiency varies with both the operating speeds and loads, it would be useful to show the efficiencies

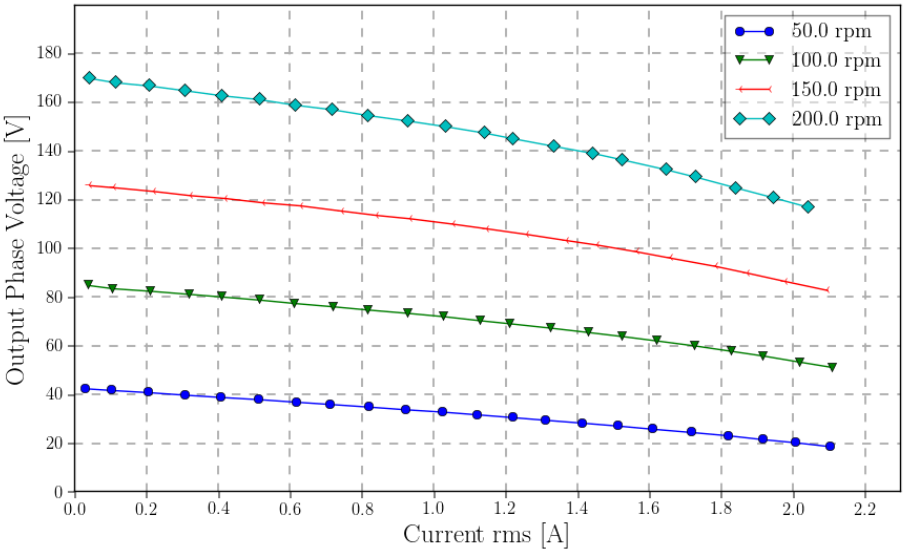

Figure 5.12: Voltage regulation at different speeds.

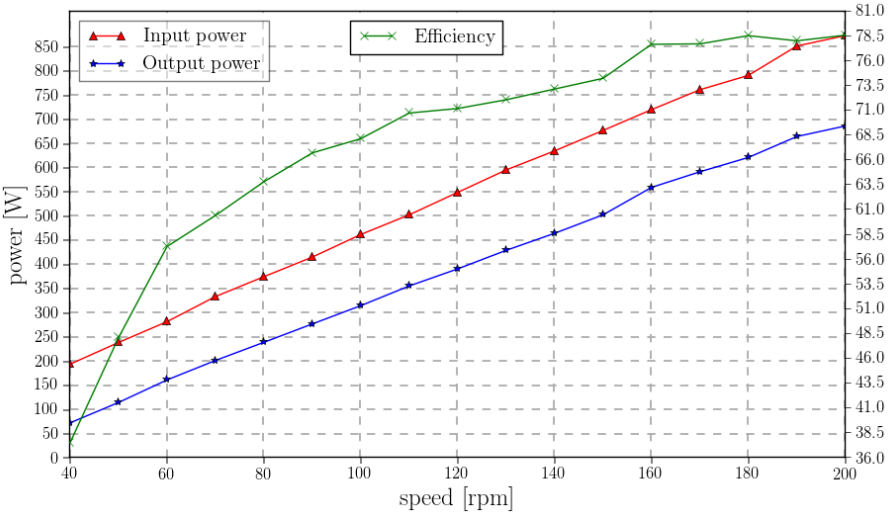

Figure 5.13: Input and output powers at rated current as function of speed.

under various operation conditions. Therefore, further measurements were carried out to construct an efficiency map for a better evaluation of the machine's performance. Fig. 5.14 is the measured efficiency map of the prototype machine. It can be observed that the efficiency increases at higher speeds. Looking from perspective of the load at fixed speed, the efficiency increases with load reaching a peak point after which further increase leads to a drop in efficiency. This may be attributed to the fact that at high loads, the stator and frequency losses increase significantly, and the resultant heat is generated which then reduces the flux density of the permanent magnets. It should also be noted that the peak efficiency is reached before the gear can slip, that is, by the time the gear is overloaded, the machine is already running at an un-preferred region of low efficiency.

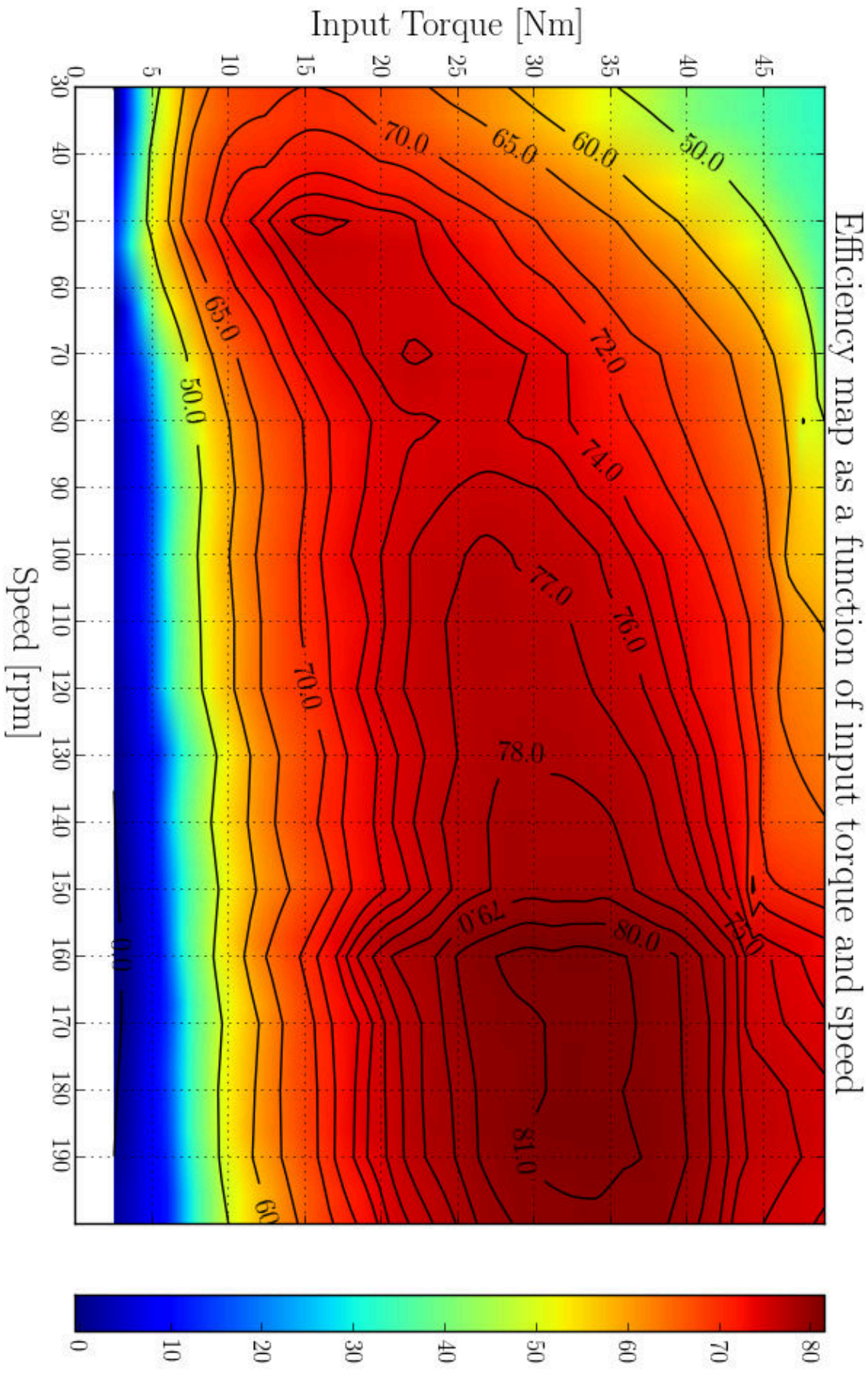

Figure 5.14: Efficiency map of input speed and torque.

Chapter 6

Conclusions and Recommendations

In this thesis the design optimization and performance evaluation of an outer-stator type magnetically geared permanent magnet machine for wind power applications is described. A prototype machine has been constructed according to the optimized design and experimentally evaluated. The fundamental theory of the magnetically geared PM machine and the design methodology have been addressed in previous chapters. The main conclusions and findings may be summarized as follows:

- The potential advantages of a magnetically geared PM machine for wind power applications include:
  - The over-load protection and contact-less power transmission characteristics of the MGPM machine may safeguard the wind generator against unpredicted wind loads, and reduce the maintenance requirements
  - The high torque density and relatively high single-stage gear ratio property of MGPM machines make them suitable for medium-speed wind power generation applications where the wind speeds are low and input torque is high.
- The outer-stator type magnetically geared PM (MGPM) machine has some attractive features such as a relatively simple mechanical layout (one air-gap less than that of an inner-stator type MGPM machine) and a very high torque density.
- Due to the fact that the MGPM machine incorporates both an MG and a PM machine in one volume, integrated mechanically and magnetically, the design approach of this machine is more complicated than that of conventional machines. An efficient FEM based design optimization procedure has been successfully implemented in the design of the MGPM machine.
- The optimized results prove that the torque capability of this machine is superior to that of many other machine types. The transient analysis of the optimized machine

(2D and 3D) shows low core losses, which implies that the machine can potentially achieve very high efficiency.

- The selection of suitable pole/slot combinations for both the stator and MG are important as the designs with poor torque quality and unbalanced magnetic pull have to be avoided. Considering the small size of the prototype machine, the practically available options are somewhat limited. However, for large machines, more design options are available.

- A prototype machine was fabricated during this project, which provides the designer with some practical experience in addition to the theoretical knowledge acquired throughout the study. It is quite challenging to practically realize some of the optimized machine parameters perfectly during construction, which requires slight adjustments that might alter the machine's performance. Hence both the mechanical design and electromagnetic design should be carried out in parallel.

- The measured torque performance compares favourably with the predicted ones, which shows that the design approach is accurate. However, the measured efficiency differs from the calculated results by a significant margin. This difference is mainly attributed to higher than expected no-load loss, which implies that mechanical design should be re-visited to reduce these unwanted losses.

6.1 Recommendations for future work

- Appropriate provision for mechanical losses should be made during the design phase for better prediction of efficiency, as these losses appear to be significant due to many rotating components or bearings being included in the machine, which lead to the machine's performance being overestimated. This also calls for careful shaft and bearing design to minimize the no-load losses, since it was found that the bearings on this prototype are axially pre-loaded, inducing additional losses.

- It is of great importance to perform the thermal analysis of this machine since the PMs on the stator surface are exposed to the high temperature effects from the stator coils. Cooling methods other than natural air may also be used to protect these PMs against demagnetization.

- Great care must be taken when designing the stator since this component accommodates both the PMs and coil windings. A poor design may complicate the winding process, making it more difficult to achieve a high slot filling-factor, which derates the machine's performance.

- Since the gradient based optimization algorithms were implemented in the current task, it is suggested that non-gradient based optimization algorithms be tried in future.

Appendices

Appendix A

Technical Drawings and Pictures Of Components

A.1 Dimensions

A.1.1 Permanent Magnets

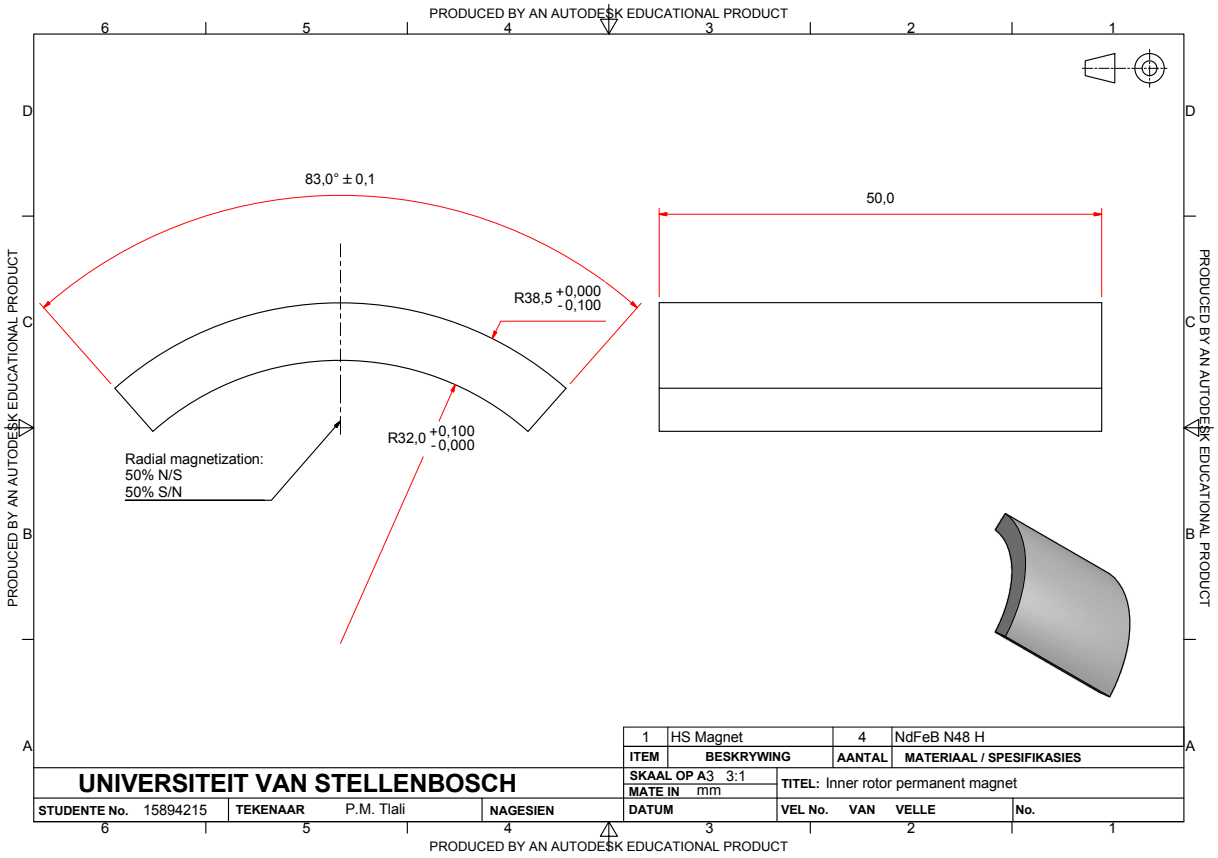

(a) Inner rotor permanent magnets

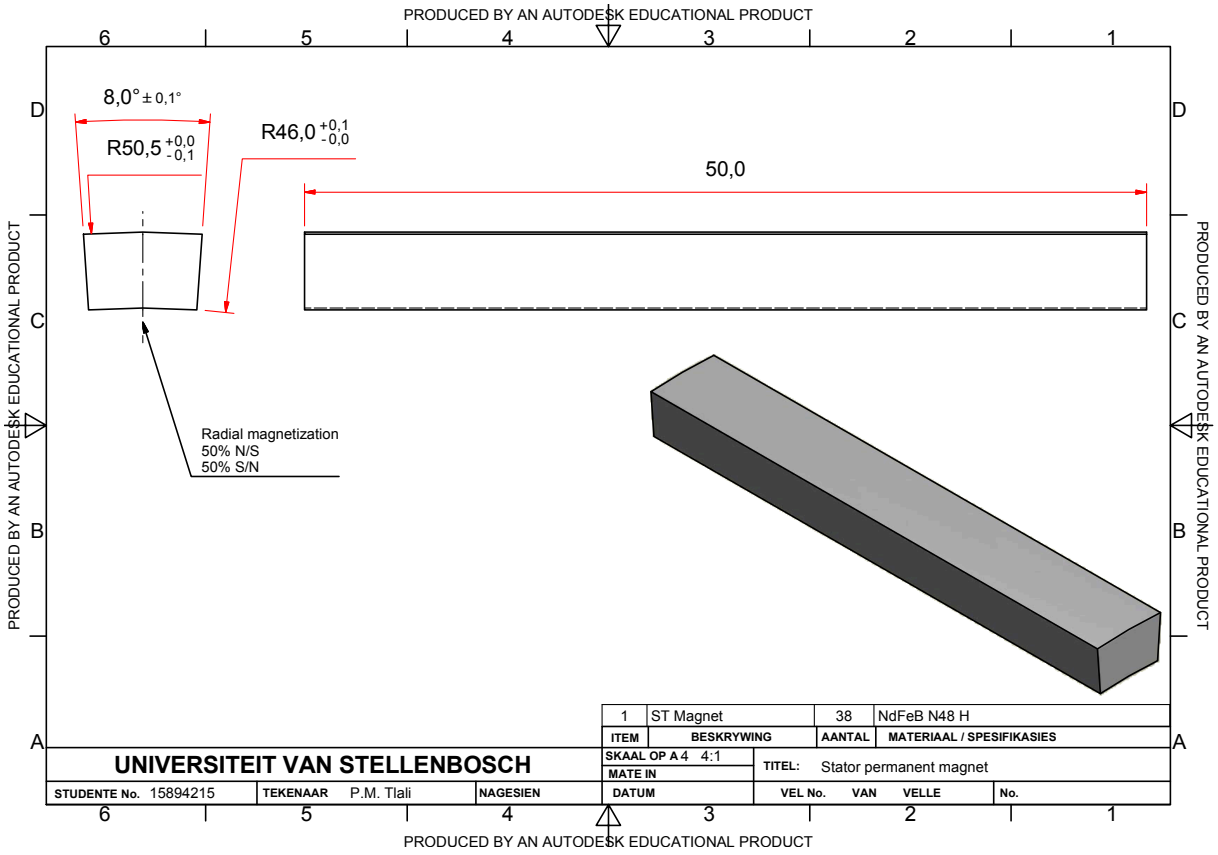

(b) Permanent magnets stuck on the stator

Figure A.1: Permanent magnets.

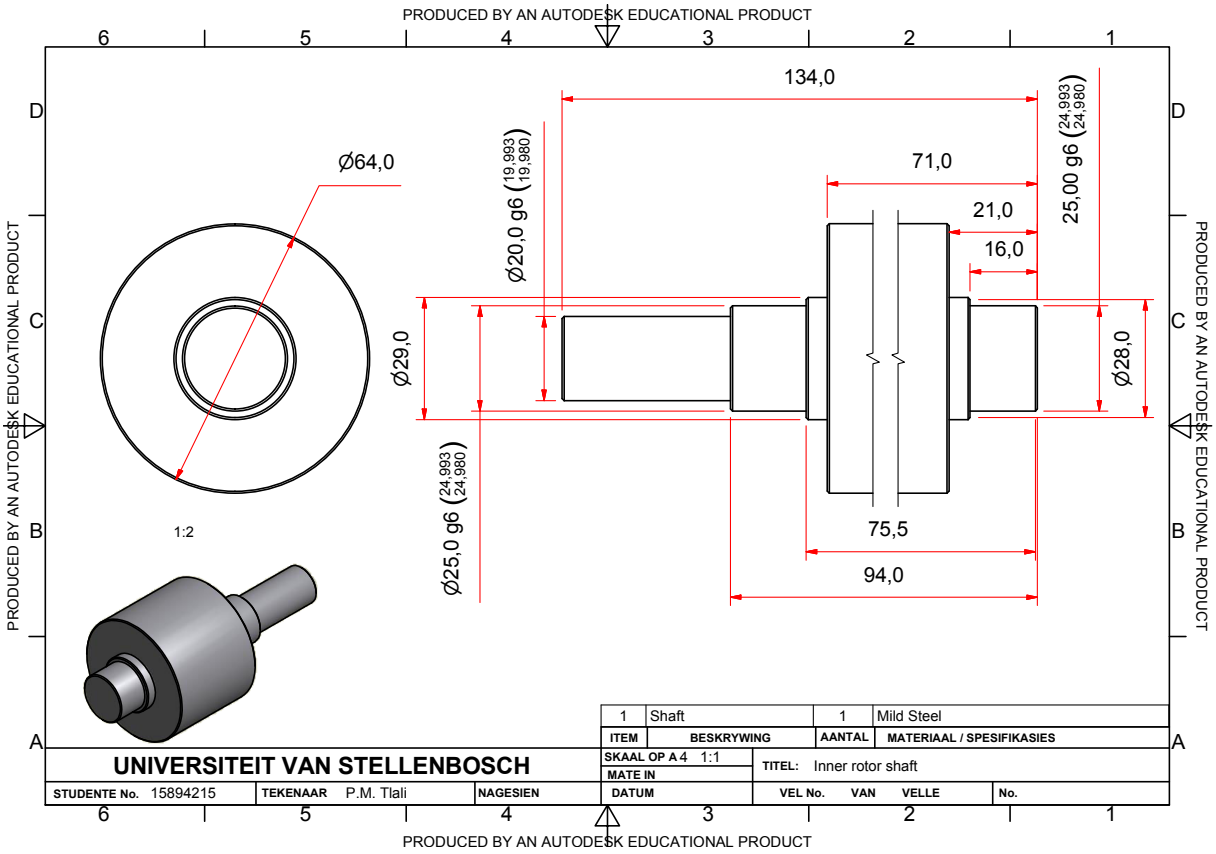

Figure A.2: Shaft.

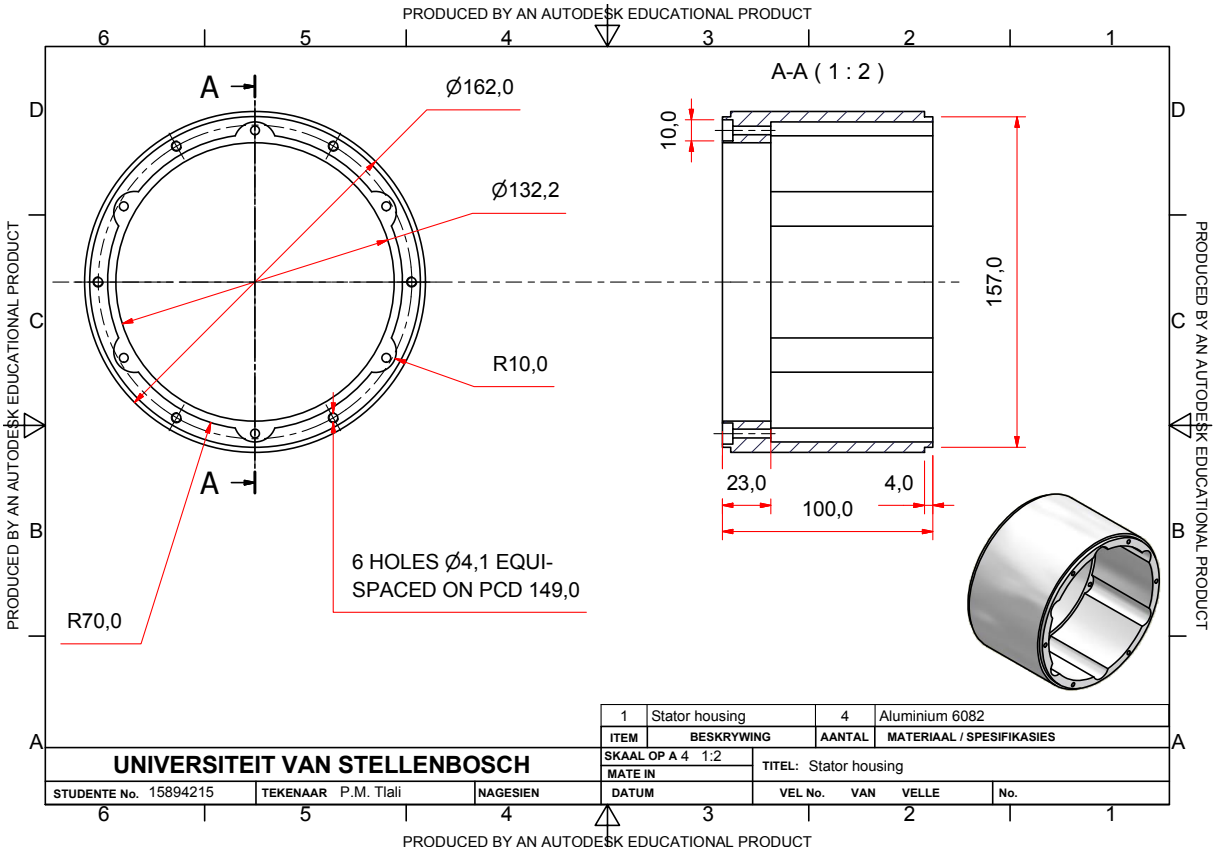

Figure A.3: Stator frame.

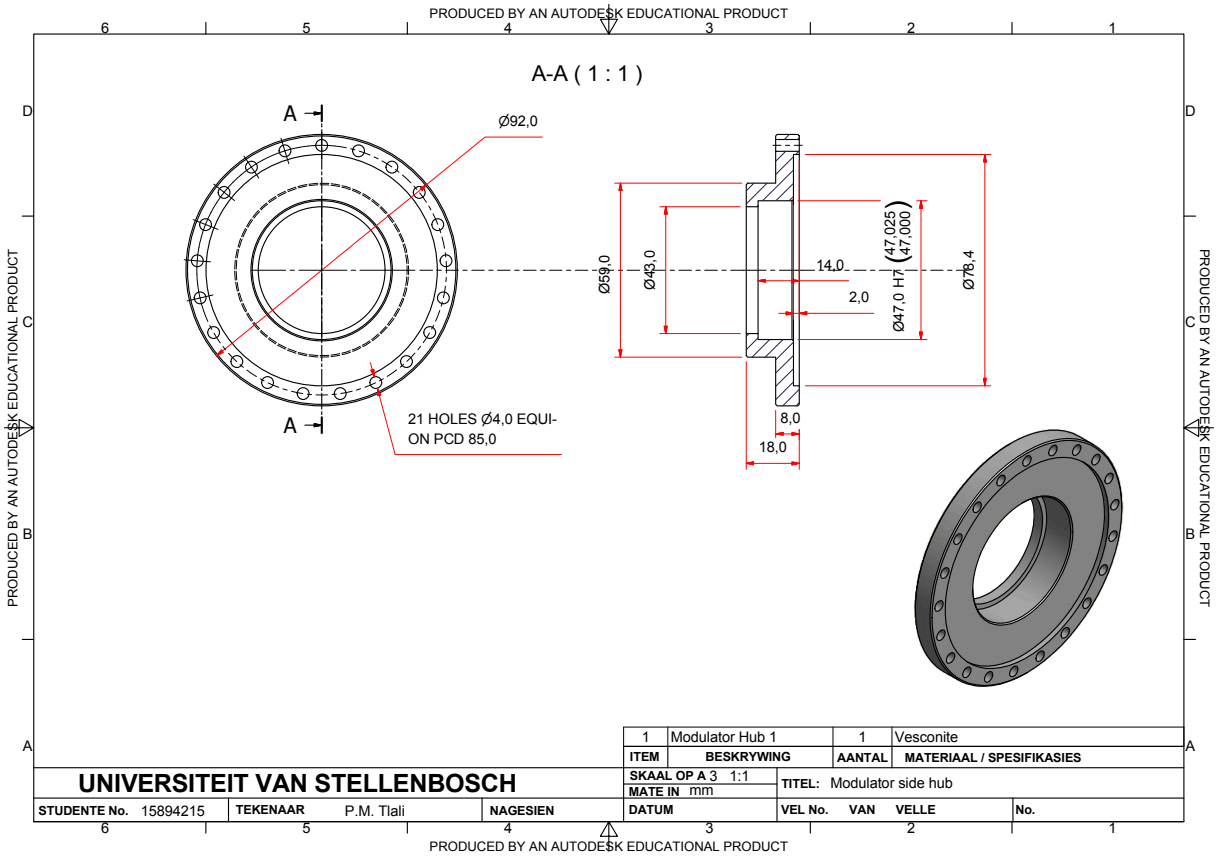

(a) Modulator hub 1

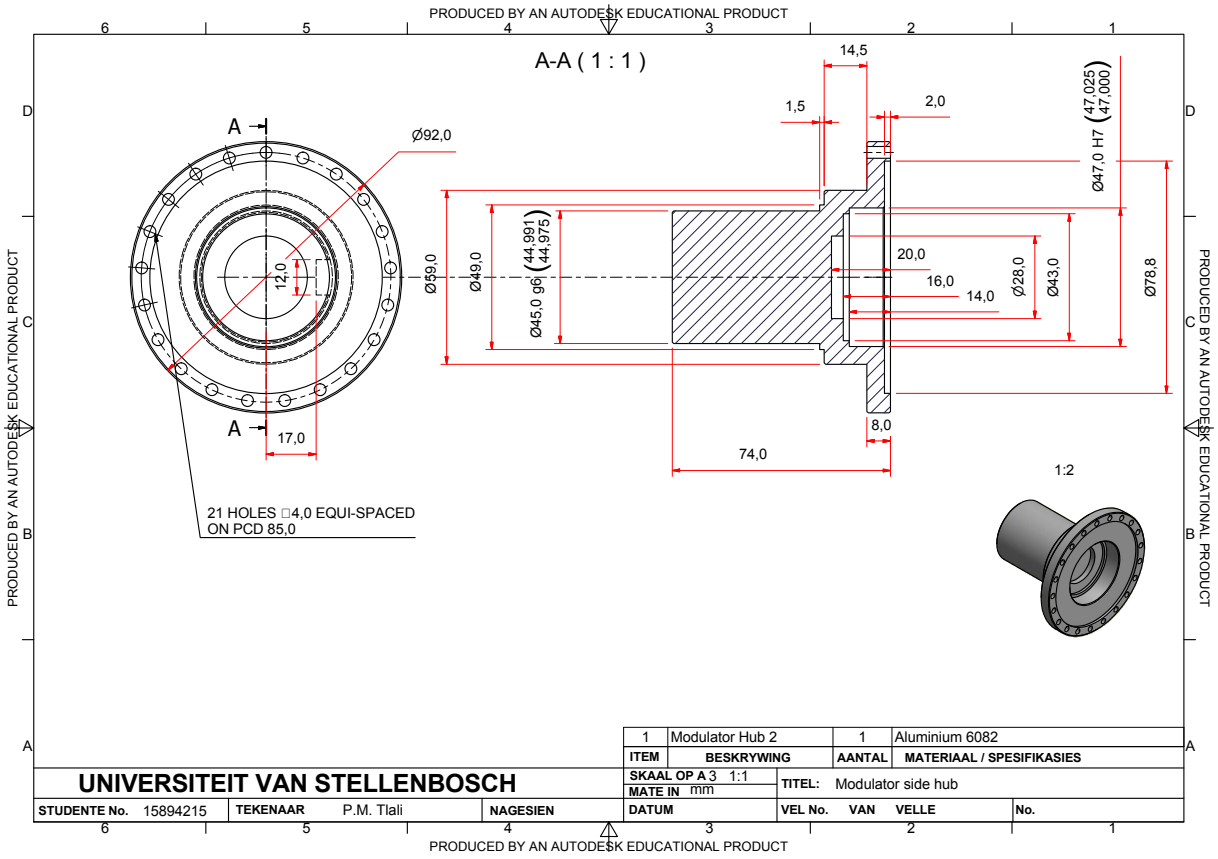

(b) Modulator hub 2

Figure A.4: Modulator side hubs.

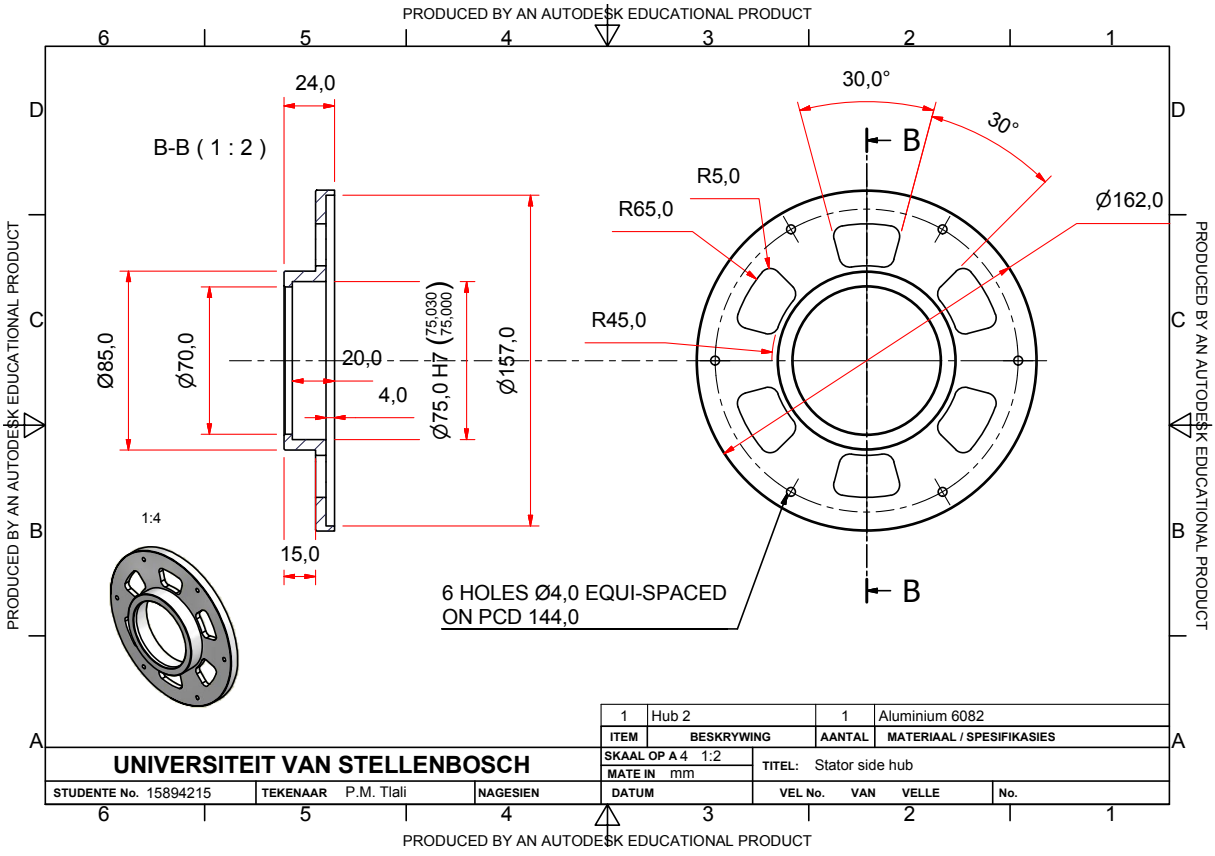

(a) Stator hub 1

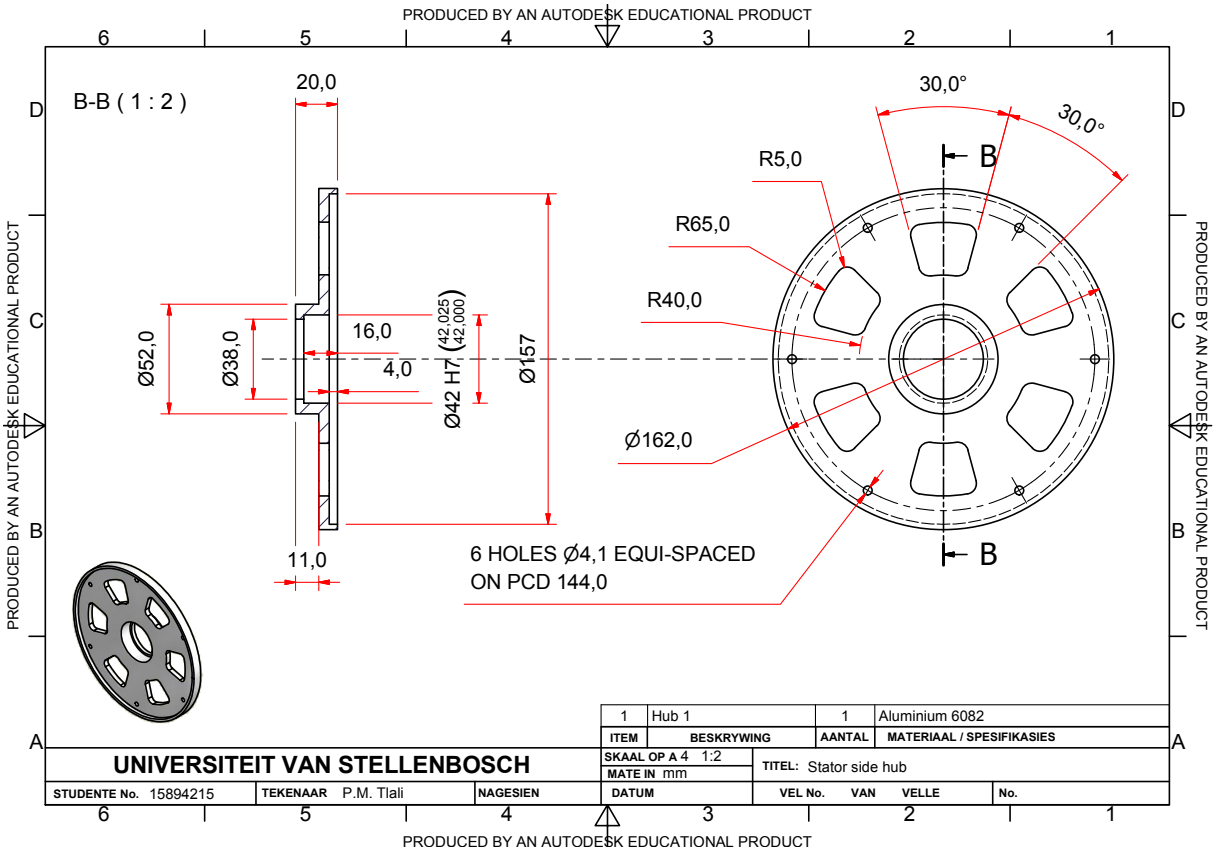

(b) Stator hub 2

Figure A.5: Stator side hubs.

List of References

[1] REN21, "Renewables global status report 2006 update," in *Renewable Energy Policy Network for the 21 century*, pp. 1–32, 2006.

[2] REN21, "Renewables global status report 2009 update," in *Renewable Energy Policy Network for the 21 century*, pp. 1–32, 2009.

[3] REN21, "Renewables 2012 global status report," in *Renewable Energy Policy Network for the 21 century*, pp. 1–172, 2012.

[4] RNS21, "Renewables 2014 global status report," in *Renewable Energy Policy Network for the 21 century*, pp. 1–215, 2014.

[5] "The gearbox problem," in *Northern Power Systems*, 2009.

[6] A. Ragheb and M. Ragheb, "Wind turbine gearbox technologies," in *Nuclear Renewable Energy Conference (INREC), 2010 1st International*, pp. 1–8, March 2010.

[7] H. Polinder, F. Van der Pijl, G.-J. de Vilder, and P. Tavner, "Comparison of direct-drive and geared generator concepts for wind turbines," in *Electric Machines and Drives, 2005 IEEE International Conference on*, pp. 543–550, 2005.

[8] M. Kimura, K. Ide, K. Nishihama, M. Futami, M. Ichinose, T. Fujigaki, M. Iizuka, K. Imaie, Y. Yagi, and J. Tamura, "A study of generator system selection for large wind turbine generator system," *Electrical Engineering in Japan*, vol. 161, no. 1, pp. 51–57, 2007.

[9] P. Tlali, R.-J. Wang, and S. Gerber, "Magnetic gear technologies: A review," in *Electrical Machines (ICEM), 2014 XXI International Conference on*, pp. 539–545, Sept 2014.

[10] C. G. Armstrong, "Power transmitting device," 11 1901.

[11] A. H. Neuland, "Apparatus for transmitting power," 2 1916.

[12] T. Von Zweigbergk, "Electric change-speed gearing for automobiles," 1 1919.

[13] H. T. Faus, "Magnet gearing," 5 1941.

[14] S. Rand, "Magnetic transmission system," 8 1970.

[15] M. Hetzel, "Low friction miniature gear drive for transmitting small forces, and method of making same," 2 1974.

[16] K. Ikuta, S. Makita, and S. Arimoto, "Non-contact magnetic gear for micro transmission mechanism," in *Micro Electro Mechanical Systems, 1991, MEMS '91, Proceedings. An Investigation of Micro Structures, Sensors, Actuators, Machines and Robots. IEEE*, pp. 125–130, Jan 1991.

[17] Y. Yao, D. Huang, C. Lee, S. Wang, D. Chiang, and T. Ying, "Magnetic coupling studies between radial magnetic gears," *Magnetics, IEEE Transactions on*, vol. 33, pp. 4236–4238, Sep 1997.

[18] Y. Yao, D. Huang, C. C. Hsieh, D. Chiang, and S. Wang, "Simulation study of the magnetic coupling between radial magnetic gears," *Magnetics, IEEE Transactions on*, vol. 33, pp. 2203–2206, Mar 1997.

[19] E. Furlani, "A two-dimensional analysis for the coupling of magnetic gears," *Magnetics, IEEE Transactions on*, vol. 33, pp. 2317–2321, May 1997.

[20] Y. Yao, D. Huang, C. C. Hsieh, D. Chiang, S. Wang, and T. Ying, "The radial magnetic coupling studies of perpendicular magnetic gears," *Magnetics, IEEE Transactions on*, vol. 32, pp. 5061–5063, Sep 1996.

[21] S. Kikuchi and K. Tsurumoto, "Design and characteristics of a new magnetic worm gear using permanent magnet," *Magnetics, IEEE Transactions on*, vol. 29, pp. 2923–2925, Nov 1993.

[22] S. Kikuchi and K. Tsurumoto, "Trial construction of a new magnetic skew gear using permanent magnet," *Magnetics, IEEE Transactions on*, vol. 30, pp. 4767–4769, Nov 1994.

[23] M. Baermann, "Permanent magnet device for generating electrical energy," 9 1966.

[24] X. Li, K. Chau, M. Cheng, and W. Hua, "Comparison of magnetic-geared permanent magnet machines," *Progress In Electromagnetics Research*, vol. 133, pp. 177–198, 2013.

[25] J. P. Yonnet, "A new type of permanent magnet coupling," *Magnetics, IEEE Transactions on*, vol. 17, pp. 2991–2993, Nov 1981.

[26] R. Hornreich and S. Shtrikman, "Optimal design of synchronous torque couplers," *Magnetics, IEEE Transactions on*, vol. 14, pp. 800–802, Sep 1978.

[27] T. B. Martin, "Magnetic transmission," 4 1968.

[28] G. A. Reese, "Magnetic gearing arrangement," 1 1967.

[29] N. Laing, "Magnetic transmission," 2 1972.

[30] N. Laing, "Centrifugal pump with magnetic drive," 10 1973.

[31] B. Ackermann and L. Honds, "Magnetic drive arrangement comprising a plurality of magnetically cooperating parts which are movable relative to one another," 5 1997.

[32] B. Ackermann, "Magnetic drive arrangement," 11 1999.

[33] K. Atallah and D. Howe, "A novel high-performance magnetic gear," *Magnetics, IEEE Transactions on*, vol. 37, pp. 2844–2846, Jul 2001.

[34] S. Mezani, K. Atallah, and D. Howe, "A high-performance axial-field magnetic gear," *Journal of Applied Physics*, vol. 99, pp. 08R303–08R303–3, Apr 2006.

[35] N. Niguchi, K. Hirata, M. Muramatsu, and Y. Hayakawa, "Dynamic analysis of axial-type magnetic gear employing 3-d fem," in *Electromagnetic Field Computation (CEFC), 2010 14th Biennial IEEE Conference on*, pp. 1–1, May 2010.

[36] K. Atallah, J. Wang, and D. Howe, "A high-performance linear magnetic gear," *Journal of Applied Physics*, vol. 97, pp. 10N516–10N516–3, May 2005.

[37] R. Holehouse, K. Atallah, and J. Wang, "Design and realization of a linear magnetic gear," *Magnetics, IEEE Transactions on*, vol. 47, pp. 4171–4174, Oct 2011.

[38] R. Holehouse, K. Atallah, and J. Wang, "A linear magnetic gear," in *Electrical Machines (ICEM), 2012 XXth International Conference on*, pp. 563–569, Sept 2012.

[39] J. Rens, K. Atallah, S. D. Calverley, and D. Howe, "A novel magnetic harmonic gear," in *Electric Machines Drives Conference, 2007. IEMDC '07. IEEE International*, vol. 1, pp. 698–703, May 2007.

[40] J. Rens, R. Clark, S. Calverley, K. Atallah, and D. Howe, "Design, analysis and realization of a novel magnetic harmonic gear," in *Electrical Machines, 2008. ICEM 2008. 18th International Conference on*, pp. 1–4, Sept 2008.

[41] J. Rens, K. Atallah, S. Calverley, and D. Howe, "A novel magnetic harmonic gear," *Industry Applications, IEEE Transactions on*, vol. 46, pp. 206–212, Jan 2010.

[42] F. Jorgensen, T. Andersen, and P. Rasmussen, "The cycloid permanent magnetic gear," *Industry Applications, IEEE Transactions on*, vol. 44, pp. 1659–1665, Nov 2008.

[43] A. Landry, "Magnetic transmission," 2 1975.

[44] N. Sakai, "Multiple magnet drive pump," 7 1989.

[45] W. J. Mabe, "Magnetic transmission," 5 1991.

[46] C. Huang, M. Tsai, and B. Lin, "Development of new magnetic planetary gears for transmission systems," in *Magnetics Conference, 2006. INTERMAG 2006. IEEE International*, pp. 225–225, May 2006.

[47] C.-C. Huang, M.-C. Tsai, D. Dorrell, and B.-J. Lin, "Development of a magnetic planetary gearbox," *IEEE Trans. Magn.*, vol. 44, pp. 403–412, March 2008.

[48] M.-C. Tsai and C.-C. Huang, "Development of a variable-inertia device with a magnetic planetary gearbox," *Mechatronics, IEEE/ASME Transactions on*, vol. 16, pp. 1120–1128, Dec 2011.

[49] F. Kong, Y. Ge, X. Zhu, L. Qiao, and L. Quan, "Optimizing design of magnetic planetary gearbox for reduction of cogging torque," in *IEEE Vehicle Power & Prop. Conf. (VPPC), pp.1-5*, 2013.

[50] N. Frank and H. Toliyat, "Analysis of the concentric planetary magnetic gear with strengthened stator and interior permanent magnet (ipm) inner rotor," in *Energy Conversion Congress and Exposition (ECCE), 2010 IEEE*, pp. 2977–2984, Sept 2010.

[51] L. Bronn, R.-J. Wang, and M. Kamper, "Development of a shutter type magnetic gear," Proceedings of the 19th Southern African Universities Power Engineering Conference (SAUPEC), Witwatersrand, Johannesburg, South Africa, 01 2010.

[52] S. Gerber and R.-J. Wang, "Evaluation of a prototype magnetic gear," in *Industrial Technology (ICIT), 2013 IEEE International Conference on*, pp. 319–324, Feb 2013.

[53] L. Jian, K. Chau, W. Li, and J. Li, "A novel coaxial magnetic gear using bulk hts for industrial applications," *Applied Superconductivity, IEEE Transactions on*, vol. 20, pp. 981–984, June 2010.

[54] M. Fukuoka, K. Nakamura, and O. Ichinokura, "Experimental tests of surface permanent magnet magnetic gear," in *Electrical Machines and Systems (ICEMS), 2012 15th International Conference on*, pp. 1–6, Oct 2012.

[55] P. Rasmussen, T. O. Andersen, F. T. Joergensen, and O. Nielsen, "Development of a high performance magnetic gear," in *Industry Applications Conference, 2003. 38th IAS Annual Meeting. Conference Record of the*, vol. 3, pp. 1696–1702 vol.3, Oct 2003.

[56] L. Jian and K. Chau, "A coaxial magnetic gear with halbach permanent-magnet arrays," *Energy Conversion, IEEE Transactions on*, vol. 25, pp. 319–328, June 2010.

[57] A. Razzell and J. Cullen, "Compact electrical machine," 2004.

[58] K. Chau, D. Zhang, J. Jiang, C. Liu, and Y. Zhang, "Design of a magnetic-geared outer-rotor permanent-magnet brushless motor for electric vehicles," *Magnetics, IEEE Transactions on*, vol. 43, pp. 2504–2506, June 2007.

[59] K. Atallah, S. Calverley, R. Clark, J. Rens, and D. Howe, "A new pm machine topology for low-speed, high-torque drives," in *Electrical Machines, 2008. ICEM 2008. 18th International Conference on*, pp. 1–4, Sept 2008.

[60] M. Venturini and F. Leonardi, "High torque, low speed joint actuator based on pm brushless motor and magnetic gearing," in *Industry Applications Society Annual Meeting, 1993., Conference Record of the 1993 IEEE*, pp. 37–42 vol.1, Oct 1993.

[61] L. W. Chubb, "Vernier motor," 1 1933.

[62] L. Jian, G. Xu, Y. Gong, J. Song, J. Liang, and M. Chang, "Electromagnetic design and analysis of a novel magnetic gear integrated wind power generator using time-stepping finite element method," *Progress In Electromagnetics Research*, vol. 113, pp. 351–367, 2011.

[63] P. Rasmussen, H. H. Mortensen, T. Matzen, T. Jahns, and H. Toliyat, "Motor integrated permanent magnet gear with a wide torque-speed range," in *Energy Conversion Congress and Exposition, 2009. ECCE 2009. IEEE*, pp. 1510–1518, Sept 2009.

[64] P. Rasmussen, T. V. Frandsen, K. K. Jensen, and K. Jessen, "Experimental evaluation of a motor integrated permanent magnet gear," in *Energy Conversion Congress and Exposition (ECCE), 2011 IEEE*, pp. 3982–3989, Sept 2011.

[65] S. Du, Y. Zhang, and J. Jiang, "Research on a novel combined permanent magnet electrical machine," in *Electrical Machines and Systems, 2008. ICEMS 2008. International Conference on*, pp. 3564–3567, Oct 2008.

[66] L. Jian, K. Chau, and J. Jiang, "An integrated magnetic-geared permanent-magnet in-wheel motor drive for electric vehicles," in *Vehicle Power and Propulsion Conference, 2008. VPPC '08. IEEE*, pp. 1–6, Sept 2008.

[67] K. Atallah, J. Rens, S. Mezani, and D. Howe, "A novel "pseudo" direct-drive brushless permanent magnet machine," *Magnetics, IEEE Transactions on*, vol. 44, pp. 4349–4352, Nov 2008.

[68] S. Gerber and R.-J. Wang, "Torque capability comparison of two magnetically geared pm machine topologies," in *Industrial Technology (ICIT), 2013 IEEE International Conference on*, pp. 1915–1920, Feb 2013.

[69] R.-J. Wang, L. Bronn, S. Gerber, and P. Tlali, "Design and evaluation of a disc-type magnetically geared pm wind generator," in *Power Engineering, Energy and Electrical Drives (POWERENG), 2013 Fourth International Conference on*, pp. 1259–1264, May 2013.

[70] Z. Zhu, D. Howe, E. Bolte, and B. Ackermann, "Instantaneous magnetic field distribution in brushless permanent magnet dc motors. i. open-circuit field," *Magnetics, IEEE Transactions on*, vol. 29, pp. 124–135, Jan 1993.

[71] J. Gieras and M. Wing, *Permanent Magnet Motor Technology: Design and Applications*. Marcel Dekker, New York, 2 ed., 2002.

[72] J. Potgieter and M. Kamper, "Evaluation of calculation methods and the effect of end-winding inductance on the performance of non overlap winding pm machines," in *Electrical Machines (ICEM), 2012 XXth International Conference on*, pp. 243–249, Sept 2012.

[73] S. E. Skaar, Ø. Krøvel, and R. Nilssen, "Distribution, coil-span and winding factors for PM machines with concentrated windings," in *Electrical Machines (ICEM), 2006 XVII International Conference on*, September 2006.

[74] Z. Zhu and D. Howe, "Influence of design parameters on cogging torque in permanent magnet machines," *Energy Conversion, IEEE Transactions on*, vol. 15, pp. 407–412, Dec 2000.

[75] N. Frank and H. Toliyat, "Gearing ratios of a magnetic gear for wind turbines," in *Electric Machines and Drives Conference, 2009. IEMDC '09. IEEE International*, pp. 1224–1230, May 2009.

[76] F. Libert and J. Soulard, "Investigation on Pole-Slot Combinations for Permanent-Magnet Machines with Concentrated Windings," in *Electrical Machines (ICEM), International Conference on*, p. 530, Sept 2004.

[77] Infolytica.

[78] G. Vanderplaats, *Multidiscipline design optimization*. Colorado Springs, 1 ed., 2007.

[79] Vanderplaats Resarch & Development, Inc, "Theory manual," 2013, June.

[80] SKF, "Equivalent dynamic bearing load," accessed on March 15, 2014.

[81] SKF, "Bearing frictional momemt estimation," accessed on March 15, 2014.

[82] SKF, "Bearing power loss," accessed on March 15, 2014.

[83] SKF, "Bearing basic rating life," accessed on March 15, 2014.

[84] J. Potgieter and M. Kamper, "Torque and voltage quality in design optimization of low-cost non-overlap single layer winding permanent magnet wind generator," *Industrial Electronics, IEEE Transactions on*, vol. 59, pp. 2147–2156, May 2012.